Department of Physics and Astronomy
University of Heidelberg

Bachelor Thesis in Physics
submitted by

Constantin Tormann

born in Lüneburg (Germany)

2018

Thermal Analysis of the Silicon Pixel Detector for the Mu3e Experiment

This Bachelor Thesis has been carried out by Constantin Tormann at the
Institute of Physics in Heidelberg
under the supervision of
Prof. Dr. André Schöning

Abstract

The Mu3e experiment will search for the charged lepton flavour violating decay $\mu^+ \rightarrow e^+e^-e^-$ with a target sensitivity of one in 10^{16} decays. To reach this sensitivity the Mu3e detector is based on a combination of a silicon pixel tracking system, a scintillating fibre detector and a scintillating tile detector. The pixel detector and the scintillating fibre detector are optimized and thinned in order to minimize the effects of multiple Coulomb scattering. Cooling the tracking detector with gaseous helium has been chosen as it offers a reasonable compromise between radiation length and cooling potential.

In the context of this thesis, the performance of the helium cooling system was studied using Computational Fluid Dynamics simulations. The analytical results indicate that an optimized design is capable of keeping the temperatures below $70\,°C$ for a given heat load of 250–$400\,mW/cm^2$. Furthermore, heatable modules for a thermal-mechanical mock-up of the detector were characterized. In combination with the simulations the results from the thermal-mechanical mock-up can be used to predict the deformation of the detector due to temperature changes and pressure gradients.

Zusammenfassung

Das Mu3e Experiment wird mit einer Sensitivität von einem in 10^{16} Zerfällen nach dem geladenen und nicht leptonzahlerhaltenden Zerfall $\mu^+ \rightarrow e^+e^-e^-$ suchen. Um diese Sensitivität zu erreichen, besteht der Mu3e Detektor aus einer Kombination aus einem Silizium-Pixel Detektor und Detektoren mit szintillierenden Fasern und Kacheln. Die Pixel und Faser Detektoren sind dahingehend optimiert Effekte durch Vielfachstreuung zu minimieren. Die Kühlung basiert auf gasförmigen Helium, welches einen guten Kompromiss zwischen Kühlpotential und Strahlungslänge bietet.

Für diese Arbeit wurde die Leistungsfähigkeit des Kühlsystems mit numerischen Fluidsimulationen untersucht. Die Ergebnisse zeigen, dass ein optimiertes System in der Lage sein wird, die Temperaturen unterhalb von $70\,°C$ zu halten, wenn die Wärmebelastung zwischen $250\,mW/cm^2$ und $400\,mW/cm^2$ beträgt. Zusätzlich wurden beheizbare Bauelemente für einen thermisch-mechanischen Teststand des Detektors charakterisiert. In Kombination mit den Simulationsergebnissen ist es möglich, erste Vorhersagen für die Deformation des Detektors zu machen. Diese entsteht aufgrund von Temperaturänderungen und Druckunterschieden im Experimentaufbau.

Contents

Chapter 1

Introduction

For more than two-thousand years humans have been trying to understand the atomic world. And since almost one hundred years we are reaching for the subatomic world. The body of acquired knowledge was finally combined in a theory that could describe the fundamental elements and their interactions. This theory is known as the Standard Model (SM) of particle physics. Since its introduction, it successfully explained a variety of experimental results and with the discovery of the Higgs boson in 2012, the last predicted particle was finally observed. But despite its great success, there are phenomena like the existence of dark matter or the nature of gravity, which are left unexplained by the SM.

Therefore, one of the main scientific goals is to find New Physics beyond the SM. This search can be done in different ways. One way is to produce new heavy particles by increasing the particle energies in collider experiments like the Large Hadron Collider (LHC) or the planned International Linear Collider (ILC). Another option is to work at high repetition rates trying to observe rare decays, which are forbidden or strongly suppressed in the SM. In order to prove a significant divergence from the SM the last method requires a high number of measured decays and a very good background suppression.

The Mu3e experiment will search for the charged lepton flavour violating (CLFV) decay $\mu^+ \rightarrow e^+e^-e^+$, which is strongly suppressed in the SM with $BR < 1 \cdot 10^{-54}$ and can only happen via higher order loop corrections with neutrino oscillation. The goal is to either detect this decay or to give an upper limit on the branching ratio in the order of 10^{-16}, four orders of magnitude below the current limit set by SINDRUM [1]. To achieve this goal in an appropriate time scale, an intense muon beam of $2 \cdot 10^9$ muons per second is needed. In the experimental concept these muons decay at rest and thus the three decay particles' energies have an upper limit of $53\,\text{MeV}$ each. In this energy regime, multiple Coulomb scattering in the detector material is the limiting factor of the momentum and vertex resolution. However, good momentum, vertex and time resolution are essential to suppress background and possibly detect this rare decay. This can only be achieved by using ultra thin detector components with higher values of radiation lengths. For this reason High Voltage Monolithic Active Pixel Sensors have been chosen to built a tracking detector consisting of four cylindrical layers. Their power consumption is expected to be approximately $250\,\text{mW/cm}^2$ and it is necessary to actively cool these components in order to prevent overheating. This

cooling system needs to fulfil the same requirement to keep effects of multiple Coulomb scattering as low as possible. It is planned to use gaseous helium, which offers a reasonable compromise between cooling potential and radiation length.

In the context of this thesis, the cooling concept for the Mu3e pixel detector has been studied using Computational Fluid Dynamics (CFD) simulations. Furthermore, preparations for a full scale thermal-mechanical mock-up of the Mu3e detector have been carried out, including the calibration of aluminium resistance thermometers and the investigation of thermal expansion of heatable silicon sensor mock-ups.

In the second chapter, a brief introduction to the SM and lepton flavour violation is given, in order to motivate the Mu3e experiment. In the third chapter, the experimental concept and the individual detector systems are explained. The fourth chapter introduces the theory of cooling with forced convection and presents the design of the cooling system. In the fifth chapter, the results of the CFD simulations are discussed and possible improvements to the design are motivated. The simulations include pure helium flow simulations in order to understand the flow distribution in the detector as well as thermal analysis of the heated detector. Chapter eight presents some preparations for the thermal-mechanical mock-up of the Mu3e detector, including the calibration of aluminium resistance thermometers, temperature distribution visualisation and silicon chip deformation studies. In the end, the thesis is summarized and an outlook is given.

Chapter 2

Theoretical Background

2.1 Standard Model of Particle Physics

The Standard Model (SM) of particle physics is a quantum field theory describing the fundamental constituents of matter (the elementary particles) and their interactions. It consists of twelve particles with spin 1/2 called fermions, their corresponding antiparticles and twelve gauge bosons with a spin of 1. The zero spin Higgs boson completes the SM. A schematic depiction of the particle content of the SM is presented in figure 2.1.
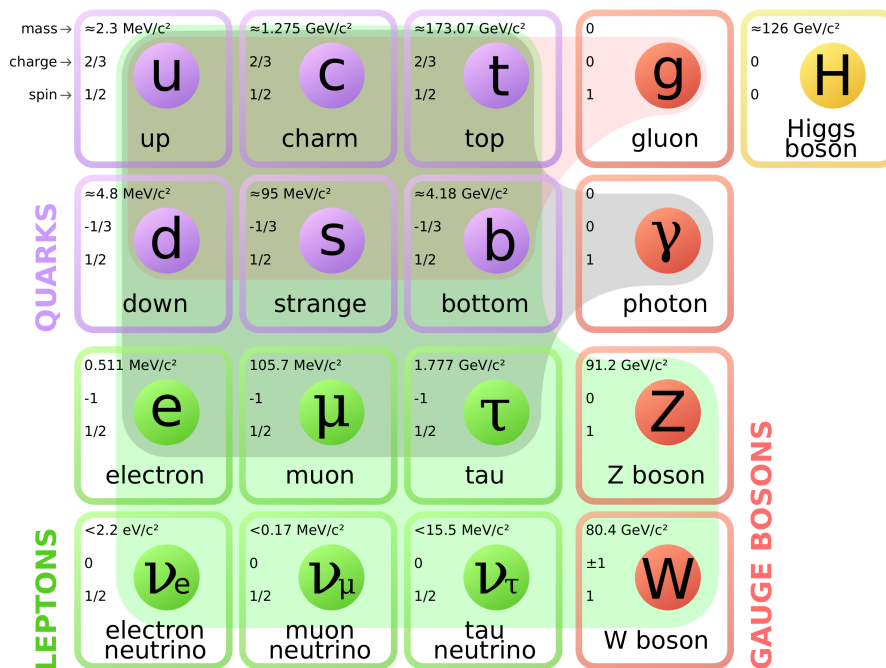

Figure 2.1: Standard Model of particle physics[2]

Gauge bosons are the mediators of the fundamental interactions: The electromagnetic in-

teraction, the weak interaction and the strong interaction.[1]

The mediator of the electromagnetic interaction is the massless photon, which couples to all particles carrying an electric charge. Due to the photon's properties this interaction has infinite range.

The electrically neutral Z boson and the two simply charged[2] $W^{\pm}$ bosons mediate the weak interaction. These bosons have fairly high masses causing a relative small interaction range. Quantum numbers characterizing each fermion can be converted when interacting with the charged W bosons. However, the different types of fermions, also referred to as flavours, can not arbitrarily change into any other flavour. Possible flavour changes and violations will be discussed in section 2.2 .

The gauge boson of the strong interaction is the eight massless gluons, which interact with any particle carrying colour charge. Despite many experimental attempts to detect freely propagating particles with non-zero colour charge, only combined, neutral states of the three different colours or colour-anticolour pairs could be observed directly. This phenomena is known as Colour Confinement. The fact that gluons carry a non-zero colour charge themselves, explains the very small range of the strong interaction and it allows the interaction with other gluons.

The sixth boson, the Higgs boson, was the last observed particle of the SM [3, 4]. In contrast to the other bosons it has zero spin and its existence proves the presence of the Higgs field. Particles acquire their masses through interactions with this field [5]. Even though the generation of particle masses can be explained, the question how masses interact with each other can not be answered by the SM. This is because the essential fourth fundamental interaction, gravity, is still missing in the SM. Luckily, the effects of gravity in the subatomic world are so weak as to be neglected.

Fermions have a spin of 1/2 and can be further classified by their masses and quantum numbers like their electric charges. There are two basic types called quarks and leptons, both consisting of six particles. Within their group, particles are related in pairs or so called generations. These generations are sorted with increasing mass, so that the lightest and most stable particle pair forms the first generation.

The defining property of quarks is their non-zero colour charge allowing them to interact strongly. They also carry an electric charge, so they can interact electromagnetically and weakly as well. Due to Colour Confinement they do not appear as free particles, but only as strongly bound states called hadrons. The first quark generation consists of the Up- and the Down-Quark.

The six leptons do not carry a colour charge, and thus do not interact strongly. Each generation is built up of one electrically charged particle and one electrically neutral neutrino. The charged particles; electron, muon and tau have sizeable mass, whereas their corresponding neutrinos are treated as massless in the SM. Experiments concerning neutrino oscillation, however, indicate non-zero masses for neutrinos. The importance of this discovery for the search of New Physics beyond the SM will be discussed in the following section 2.2 .

---

[1]Gravity is not part of the SM.
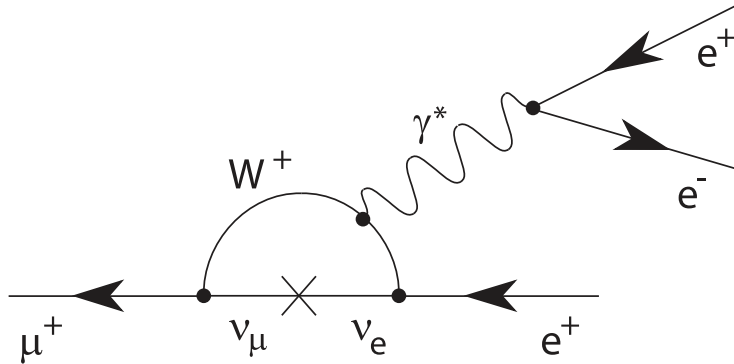[2]The charge is given in units of one electron charge.

Figure 2.2: Neutrino mixing loop diagram of the decay $\mu^+ \to e^+ e^- e^+$ [6]

2.2 Charged Lepton Flavour Violation

Each fermion flavour can be characterized by a set of flavour quantum numbers. There are six quark flavours (up, down, charm, strange, bottom, top) and three lepton flavour families (electron, muon, tau).

Quark flavour is not conserved for charged weak interactions; hence the quark flavour can change. This is possible due to the fact that the quantum states taking part in weak interaction do not match the mass eigenstates, but superpositions of the mass eigenstates. The relations are defined by the Cabibbo-Kobayashi-Maskawa (CKM) matrix [7].

Each of the three lepton generations can be assigned a lepton family number or lepton flavour. This is an additive quantum number with leptons having a value of $L_{\mathrm{i}} = 1$ and their corresponding antiparticles having a value of $L_{\bar{\mathrm{i}}} = -1$. At tree level the sums of the three different lepton flavours (denoted by the index i) are conserved.

The observation of neutrino oscillation, however, indicates that neutrinos do change their flavour (Super-Kamiokande [8], SNO [9], KamLAND [10] and others). This is referred to as lepton flavour violation (LFV).

In order to explain the flavour changes of neutral leptons it is possible to extend the SM by the introduction of the Pontecorvo-Maki-Nakagawa-Sakata (PMNS) matrix [11], the lepton equivalent to the CKM matrix. Similar to the explanation of quark flavour changes, the eigenbasis of the mass eigenstates and of the eigenstates of the weak interaction do no match. But each flavour eigenstate can be written as superposition of different mass eigenstates. This, however, requires distinguishable masses for the neutrinos, which stands in contrast to the zero mass assumption for neutrinos in the SM.

Even though this extended SM allows flavour changes of charged leptons, there is still no observation of charged Lepton Flavour Violation (cLFV). The non-observation is mainly caused by the GIM cancelation [12] which suppresses flavour changing neutral current (FCNC) decays to unobservable limits. As an example, figure 2.2 shows the Feynman diagram of the decay $\mu^+ \to e^+ e^- e^+$, which is forbidden at tree-level in the SM and can only happen via higher order loop corrections with neutrino oscillation. Its branching ratio is $BR(\mu^+ \to e^+ e^- e^+) = \mathcal{O}(10^{-54})$ [6].

(a) Penguin diagram with SUSY loop

(b) Tree diagram with new particles
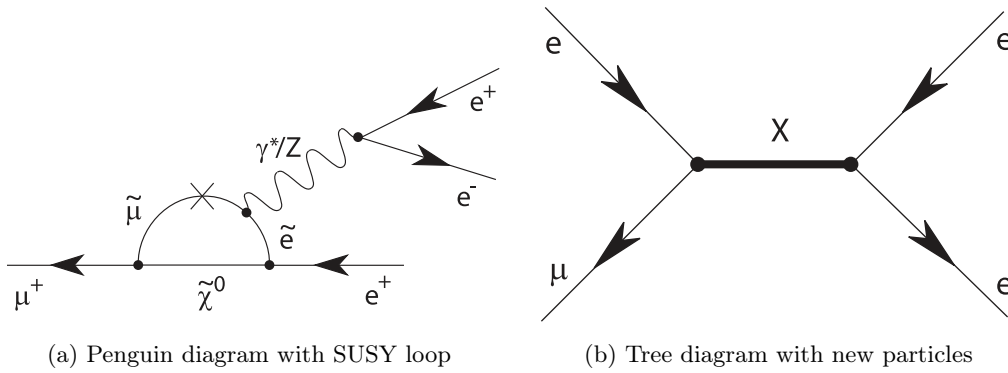
Figure 2.3: Feynman diagrams for $\mu^+ \to e^+e^-e^+$ assuming beyond SM physics [6]

Searching these rare decays offers a great opportunity to find signs of New Physics beyond the SM. Several alternative theories already predict increased branching ratios for decays like $\mu^+ \to e^+e^-e^+$ [13]. For example, super symmetric(SUSY) particles could run in γ/Z penguin diagrams as shown in fig 2.3a or there could be tree-level diagrams involving new particles like massive electrically neutral gauge bosons. The latter is shown in fig 2.3b, where X denotes the yet unknown particle.

Chapter 3

The Mu3e Experiment

The Mu3e experiment will search for the charged lepton flavour violating decay of one positive muon into two positrons and one electron. The goal is to either detect this decay or set a new branching ratio limit of 10^{-16} at 90% confidence level (CF), which is four orders of magnitude lower than the previously performed search by the SINDRUM experiment [1]. In order to reach this sensitivity, the experiment requires excellent timing, vertex and momentum resolution. Furthermore, measuring the necessary amount of decays in appropriate runtime can only be accomplished by working at a rate of $\geq 2 \cdot 10^9$ muons per second. Such a high number of decay particles can only be produced by the High Intensity Muon Beamline (HIMB), currently under study at the Paul Scherrer Institute (PSI) in Switzerland [6]. Until this beamlines becomes available it is possible to use the Compact Muon Beamline(CMB), which provides $1 \cdot 10^8$ muons per second. At this rate the Mu3e experiment can reach sensitivity of one in 10^{15} decays.

3.1 The Signal Decay $\mu^+ \rightarrow e^+ e^- e^+$

3.1.1 Kinematics

The identification of the decay $\mu^+ \rightarrow e^+ e^- e^+$ is based on momentum and energy conservation. Assuming the muons decay at rest, the energies of the decay particles add up to the muon mass of $105.659 \, \text{MeV}/c^2$ [14]. In addition, the decay particles originate simultaneously from a single vertex (decay point), leading to a vanishing total momentum

$$|\vec{p_{\text{tot}}}| = \left| \sum_{i=1}^{3} \vec{p_i} \right| = 0. \tag{3.1}$$

These terms combined restrict the decay particles' energies to a range of one electron mass and half a muon mass ($< 53 \, \text{MeV}/c^2$).

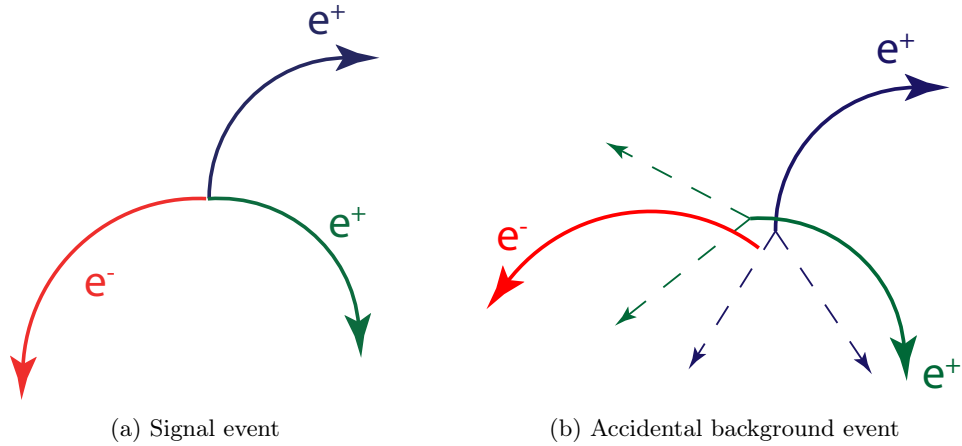(a) Signal event   (b) Accidental background event

Figure 3.1: Schematic comparison of (a) the Mu3e signal event and (b) an accidental background event of two Michel decays with an additional electron

3.1.2 Background

The final sensitivity of the Mu3e experiment strongly depends on the ability to distinguish between signal decay and background. Options to reject background are presented for the two main sources that need to be considered: accidental background and internal conversion.

Accidental Background

The majority of positive muons will decay into positrons via the dominant decay $\mu^+ \rightarrow e^+ \nu_e \bar{\nu}_\mu$, also known as Michel decay. Since the characteristic electron of the target decay is missing, combinations of three Michel decays can only be misinterpreted as $\mu^+ \rightarrow e^+ e^- e^+$, if tracks are wrongly reconstructed.

Unfortunately, there are further processes like Bhabha scattering (decay positrons scattering off electrons in the detector material) and photon conversion which can create $e^+ e^-$ pairs originating from a common vertex. The converting photons can arise from radiative muon decays or bremsstrahlung.

The risk of accidentally interpreting a combination of these processes as $\mu^+ \rightarrow e^+ e^- e^+$ increases for the high rates used in the experiment. Since the particles originate from different processes, they do not share a common vertex and are not coincident in time. Furthermore, the momentum and energy constraints are most likely violated. This type of background can be suppressed by excellent time, momentum and vertex resolution. A sketch of the signal decay and an accidental background event can be seen in figure 3.1 .

Internal Conversion

The radiative muon decay with internal conversion $\mu^+ \rightarrow e^+ e^- e^+ \nu_e \bar{\nu}_\mu$ has a branching fraction of $3.4 \cdot 10^{-5}$ [14] and shows almost identical characteristics to the decay $\mu^+ \rightarrow e^+ e^- e^+$. A virtual photon of the radiative decay promptly converts into an $e^+ e^-$ pair, leading to a common vertex and time of origin for the decay particles. It is possible to distinguish between both decays, by determining the missing energy carried away by the undetected neutrinos.
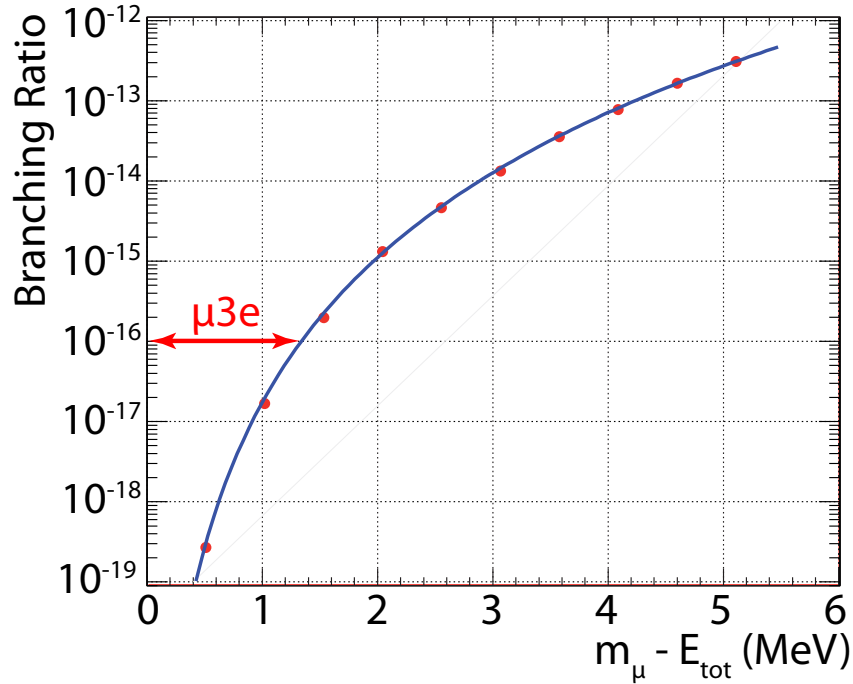
Figure 3.2: Branching ratio of the internal conversion decay $\mu^+ \to e^+e^-e^+\nu_e\bar{\nu}_\mu$ as a function of the energy cut [15]

Figure 3.2 shows the branching fraction as a function of the subtraction of the muon mass and the visible energy of the $\mu^+ \to e^+e^-e^+\nu_e\bar{\nu}_\mu$ decay. To reach a final sensitivity of 10^{-16} at 90 % CF, an energy resolution better than 1 MeV is required.

3.2   Experimental Concept

Muons enter the detector through a beampipe and are stopped on a large surface, which allows to distinguish between different vertices. A hollow double cone target made of Mylar was chosen for this purpose.

The muons' decay particles then follow helical tracks in a homogeneous magnetic field of 1 T. Their path through four layers of pixel detectors allows to precisely determine the momentum and vertex of these particles. These layers are arranged in two double layers, building up a cylindrical detector station. In between the outer and the inner double layer, a scintillating fibre detector is used for precise timing. Two additional detector stations are added on each end, upstream and downstream, of the central detector station. These stations consist of the outer pixel double layer and a scintillating tile detector underneath. Due to the magnetic field the electrically charged decay particles perform curls and pass through the tracking detector at these additional *recurl* stations. The scintillating tile detector is designed to stop the particles and give the most precise timing information below 100 ps. The complete detector with five stations is about 2 m long and placed in a solenoidal magnet with an inner diameter of 1 m. A schematic view of three stations is shown in figure 3.3. Due to the
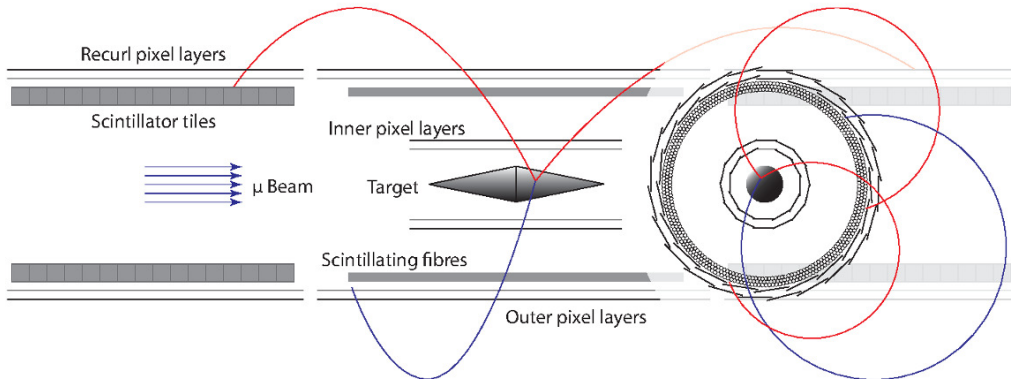
Figure 3.3: Schematic side-view and front-view of the central and two recurl stations of the Mu3e detector. The blue and the two red lines indicate the particle tracks of a signal decay [6]

low energies of the decay particles ($<53\,\text{MeV}$), the dominating factor limiting momentum and vertex resolution is multiple Coulomb scattering in the detector material. Therefore, only thin components, ideally with high radiation length, are chosen for the detector. The thickness of the silicon pixel trackers can be significantly reduced due to the High Voltage Monolithic Active Pixel Sensor (HV-MAPS) technology. For the same reason, the cooling system of the pixel detector uses a constant flow of gaseous helium, which offers a reasonable compromise between radiation length and cooling potential.

Multiple Coulomb Scattering

When charged particles traverse through matter, they are deflected on their path due to scattering at nuclei. This effect is known as multiple Coulomb scattering and results in a displacement y and a deflection angle Θ_{MS} with respect to the undisturbed beam (see figure 3.4). As this affects the track reconstruction of the decay particles, it is important to understand this process. For small deflection angles, one can use the Highland parametrization [16] to define Θ_{MS} as

$$\Theta_{\text{MS}} = \frac{13.6\ \text{MeV}}{\beta c p} z \sqrt{\frac{x}{X_0}} \left(1 + 0.038 \log \frac{x}{X_0} \right), \tag{3.2}$$

with the RMS of the central $98\,\%$ of the planar scattering angle distribution Θ_{MS}, the particles velocity in units of the speed of light β, the material's radiation length X_0, the material's charge number z and the particle's momentum p. To decrease the effects of multiple Coulomb scattering, one can either use higher particle momenta or thin materials with high radiation length. For very thin detectors, the displacement y is negligibly small and only the deflection angle has to be taken into account.
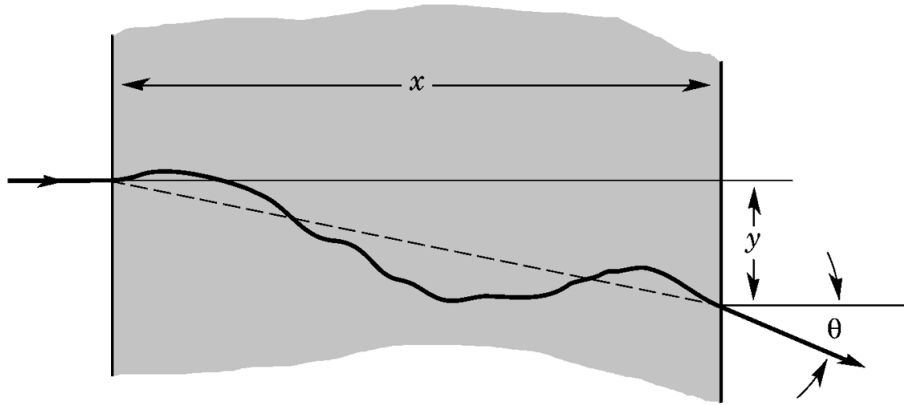
Figure 3.4: Illustration of multiple Coulomb scattering, modified from [14]

3.3 Sub Systems of the Mu3e Detector

3.3.1 Pixel Detector

Precise measurements of the particle trajectories are essential to determine the momenta and the vertex of the decay. Therefore, the tracking detector for the Mu3e experiment needs to match the following requirements. First, the detector needs to consist of ultra thin materials in order to reduce effects of multiple Coulomb scattering. Second, the dead-time of the detector needs to be small enough to process the high particle rates in the experiment. High Voltage Monolithic Active Pixel Sensor (HV-MAPS) can be thinned down to $50\,\mu m$ while providing and excellent timing resolution of below $20\,ns$. These chips are glued on flex-prints consisting of polyimide foil and aluminium traces used as power and signal lines. It is possible to create a self supporting mechanical structure by using only $25\,\mu m$ thick polyimide foil. The four barrel shaped layers with pixel sensors are numbered radially outwards and the outer two layers are about three times longer than the inner two. A more detailed description of this support structure will be presented in chapter 4, since the mechanical design and the cooling system are linked.

One pixel sensor is planned to be approximately $23 \times 19.8\,mm^2$ with a $0.5\,mm$ wide inactive region, which can be compensated by an overlap to the adjacent sensor (indicated in figure 3.3).

All together, each assembled layer will have a thickness of about $150\,\mu m$, corresponding to $\approx 0.1\,\%$ of a radiation length.

High Voltage Monolithic Active Pixel Sensor

Monolithic Active Pixel Sensors (MAPS) have a thin active volume and the electronics can be implemented directly on top of the silicon semiconductor. Hence, this technology enables to built pixel sensors with high fill factor. But the main disadvantage is the collection of charge via diffusion, which results in a time resolution in the order of several hundred nanoseconds. The HV-MAPS technology, however, collects charge via drift using a high bias exceeding $50\,V$. This method can improve the time resolution below $10\,ns$. Furthermore,
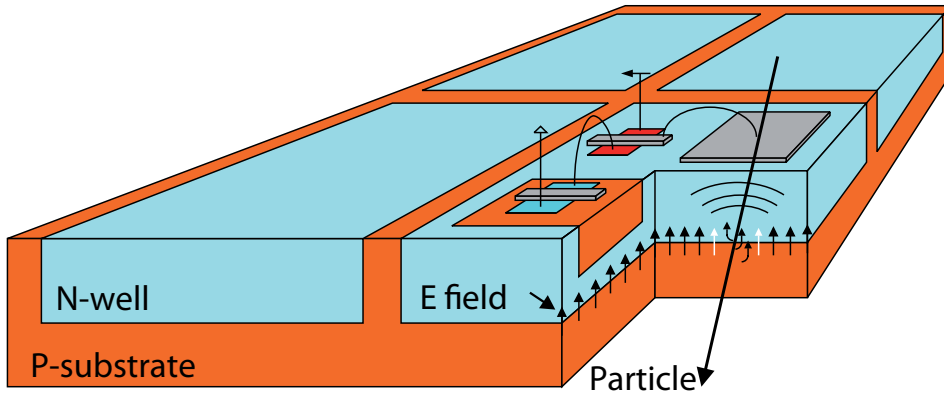
11

Figure 3.5: Schematic of a MAPS design showing four pixels [17]

the depletion zone is only about $9\,\mu m$ thick making it possible to thin the sensor down to $50\,\mu m$. A schematic of a 2×2 matrix of the HV-MAPS is visualized in figure 3.5 . The pixel sensor specifically designed for the Mu3e experiment is called MuPix and has an expected power consumption of 250–$400\,mW/cm^2$.

3.3.2 Timing Detectors

An additional time of flight system is integrated in order to measure the three coincidental electrons with excellent time resolution. As priorly explained this is necessary to suppress accidental background (see 3.1.2).

Fibre Detector

The scintillating fibre detector consists of three layers of about $300\,mm$ long scintillating fibres with $250\,\mu m$ diameter [18]. Arrays of silicon photomultiplier (SiPM) at both ends of the central station will detect the emitted photons in the fibres. These devices can be operated in magnetic fields and have high counting rates, enabling a time resolution below $500\,ps$. As the fibre detector is located in the central station at a radius of $60\,mm$ from the target center, the material and thickness needs to be a compromise between time resolution and reduction of multiple Coulomb scattering. In total, three layers with scintillating fibres correspond to $0.3\,\%$ of a radiation length.

Scintillating Tile Detector

The scintillating tile detector consists of $6.5 \times 6.5 \times 5\,mm$ sized scintillating tiles [19] and is located underneath the pixel layer in the four recurl stations. Since there is no interest in the particles after passing through the tiles, they can be stopped in the material. This enables a time resolution below $100\,ps$ at a high efficiency of nearly $100\,\%$. The readout is performed by SiPM underneath each tile.
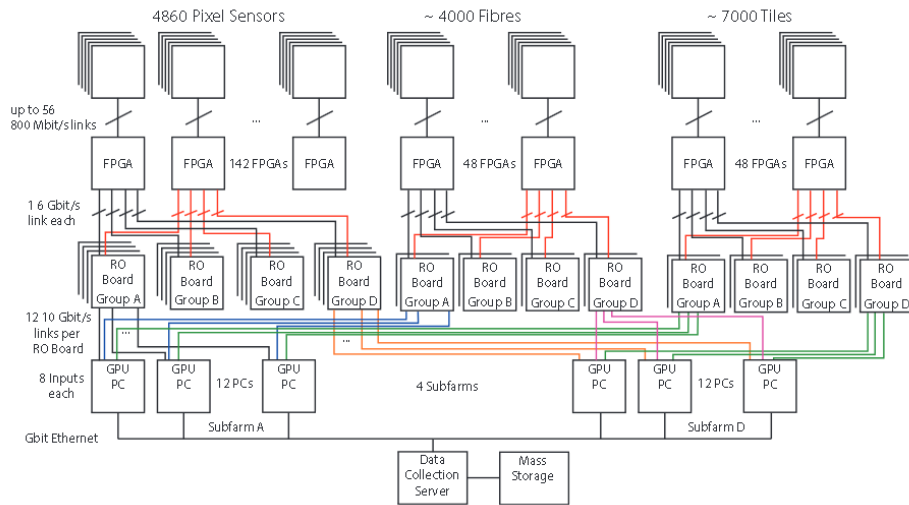
Figure 3.6: Schematic of the Mu3e DAQ: Hit informations are sent via 108 links, with 800 MBit/s each, is buffered in 238 FPGAs and sent to the readout boards. From those boards, the data is send to the GPU farm and the tracks are reconstructed. Selected events are stored.

3.3.3   Read-out System

The Mu3e data acquisition (DAQ) system consists of three layers; the front-end FPGA(field-programmable gate arrays), switching boards and the filter farm. Figure 3.6 shows the readout scheme for the experiment. Apart from the FPGAs the components for the readout system are placed outside of the magnet. Hit informations are continuously send to the FPGAs (no hardware trigger) at a rate of 1 Tbit/s. The information is passed via optical links to the PCs of the filter farm where the events are reconstructed online. Selected events are sent to a single collection server at a rate of 50 MB/s and are written to a mass storage system.

Chapter 4

The Cooling System

Overheating is a potential threat to any electronic system, included the Mu3e detector. Pixel trackers, SiPMs and FPGAs need to be actively cooled in order to maintain temperatures within their operating ranges. Studies for the pixel tracker using different MuPix prototypes found a maximum working temperature of $70\,°C$ [20]. Further experiments with the MuPix 6 and the MuPix 7 measured power consumptions per surface area of $250–400\,mW/cm^2$ [21, 22]. The anticipated goal is to have a final power consumption per area of about $250\,mW/cm^2$. Consequently, the total heat load of the central station's pixel tracker is about $1160\,W$. This comprises of $1040\,W$ for the outer pixel double layer and about $120\,W$ for the inner double layer.[1]

Keeping the temperature in a reasonable range is only one challenge for the cooling system. Another challenge is to keep the material budget as low as possible. Gaseous helium is chosen as coolant for the pixel detector, because it offers a good compromise between cooling potential and radiation length, i.e. a layer of helium with a thickness of $1\,m$ equals approximately $0.019\,\%$ of the radiation length X_0. In contrast, the same layer of nitrogen has $\frac{x}{X_0} \approx 0.3\,\%$ and each pixel tracker layer has already $\frac{x}{X_0} \approx 0.1\,\%$. The good cooling capability of Helium compared to other gases can be explained by its thermophysical properties (see section 4.1). The gas enters the detector with a temperature of slightly above $0\,°C$ in order to prevent icing of condensed humidity, which could still exist in the helium atmosphere.

In the past, a comparable cooling system was successfully used to cool the Silicon Vertex Tracker of the STAR experiment [23]. They applied a constant air flow with $23\,°C$ to remove about $180\,W$.

For completeness, it should be mentioned that the SiPMs and FPGAs use a different cooling system based on water, which is not discussed in the context of this thesis.

This chapter will give a short introduction into the theory of forced convection followed by a presentation of the mechanical structure and the cooling concept of the experiment. The chapter ends with a short discussion about the different flow types in the detector.

---

[1]Assuming $P/A = 250\,mW/cm^2$ and chip dimensions of $23 \times 19.8\,mm^2$
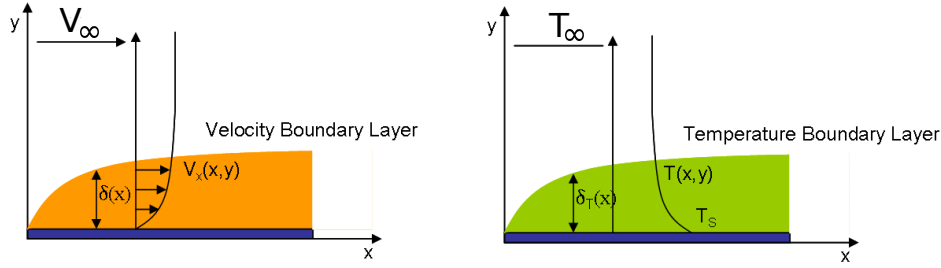
Figure 4.1: Schematic of velocity and temperature boundary layer, modified [26]

4.1 Convective Heat Transfer

The fundamental principle of cooling a heated surface with a fluid (gas or liquid) flow, is known as convection. The energy transfer comprises of two mechanisms, random molecular motion (diffusion) and macroscopic (bulk) motion (advection). The latter form of energy transfer can be described by fluid mechanics.

Additionally to convection, heat dissipation via thermal radiation occurs for all matter with a temperature greater than absolute zero. For analysis of modules with a power consumption of $100\,\mathrm{mW/cm^2}$ [24] radiative cooling could be neglected, but for increased heat loads this needs to be verified again. However, this thesis focusses on convective heat transfer and radiative cooling is mostly neglected. The main reason for this simplification is that convection affects the temperature distribution more and thus the helium cooling system needs to be optimized first. In regard to the performed simulation this decision lowers the necessary time for analysis.

Convection can occur naturally, if the flow is induced by buoyancy forces, which are due to density differences caused by temperature variations in the fluid. However, an active cooling system as the proposed one, uses external sources like pumps or fans to create the fluid flow. In this case we speak of forced convection.

The concept of boundary layers is central to understand forced convection processes. As a consequence of the fluid-surface interaction a region of varying velocities forms, ranging from zero at the surface to a finite velocity v_∞ associated with the fluid flow. This region is referred to as velocity boundary layer. Its thickness δ is typically defined as the distance from the surface where $v(\delta) = 0.99 \cdot v_\infty$ [25].

Analogously, a difference between the surface temperature T_s and outer the fluid temperature T_∞ results in a region of varying temperatures, called the temperature boundary layer. Its thickness δ_Th is defined as the distance from the surface where $T_\mathrm{s} - T(\delta_\mathrm{Th}) = 0.99(T_\mathrm{s} - T_\infty)$ [25]. In general $\delta \neq \delta_\mathrm{Th}$ applies.

For every problem involving fluid dynamics it is important to distinguish between laminar and turbulent flow, because depending on the flow type, the boundary layers and the cooling capability can differ. A laminar flow is highly ordered and one can identify uninterrupted streamlines along which particles move. In contrast, a turbulent flow is irregular and characterized by chaotic changes in pressure and velocity. A transition from laminar to turbulent flow occurs, when small perturbations in the flow can not be damped away by viscous forces.

The dimensionless Reynold number Re represents the ratio of inertia to viscous forces and, therefore, it can be used as an indicator for the flow type. It is defined as

$$Re = \frac{vL}{\nu}, \tag{4.1}$$

with the mean flow velocity v, the characteristic length L and the kinematic viscosity ν. The critical Reynolds number Re_c, i.e. the value of the Reynolds number where the transition from laminar to turbulent flow can occur, highly depends on surface shape and roughness. For the flow over a flat surface, L denotes the distance from the leading edge and Re_c is known to vary from approximately 10^5 to $3 \cdot 10^6$ [25].

In the following paragraph, an equation for the temperature distribution on a flat, heated surface cooled by forced convection is presented, considering two-dimensional, incompressible and laminar flow. A more detailed calculation can be found in [24].

Laminar Fluid Flow over a Flat Surface with Constant Heat Flux

Physical problems including fluid dynamics, require solving the Navier-Stokes equations to determine the velocity field. For incompressible flow ($\nabla \vec{v}=0$), these equations can be written in the following form

$$\rho \left(\frac{\partial \vec{v}}{\partial t} + (\vec{v} \cdot \nabla)\vec{v} \right) = -\nabla p + \mu \Delta \vec{v} + \vec{f}, \tag{4.2}$$

where ρ is the fluid density, p is the pressure, μ is the dynamic viscosity and $\vec{f}$ is the body force density. These equations can be simplified for the two-dimensional problem under consideration:

$$v_x \frac{\partial v_x}{\partial x} + v_y \frac{\partial v_x}{\partial y} = \nu \frac{\partial^2 v_x}{\partial y^2}, \tag{4.3}$$

with the kinematic viscosity ν. The velocity boundary conditions are

$$v_x(y = 0) = v_y(y = 0) = 0 \tag{4.4}$$

$$v_x(y = \infty) = v_\infty \tag{4.5}$$

Equation 4.3 needs to be solved numerically to obtain the velocity profile, which is indicated in figure 4.1 .

Then, the temperature profile can be derived by using the energy equation for a constant pressure flow field:

$$\rho c_p \left(\frac{\partial T}{\partial t} + \vec{v} \cdot \nabla T \right) = k \Delta T + \frac{d\rho_q}{dt}, \tag{4.6}$$

where c_p is the specific heat capacity at constant pressure, k is the thermal conductivity and ρ_q is the heat density. Assuming a steady state ($\frac{\partial T}{\partial t} = 0$) and no additional heat sources than the surface, the equations yields

$$v_x \frac{\partial T}{\partial x} + v_y \frac{\partial T}{\partial y} = \alpha \frac{\partial^2 T}{\partial y^2}, \tag{4.7}$$
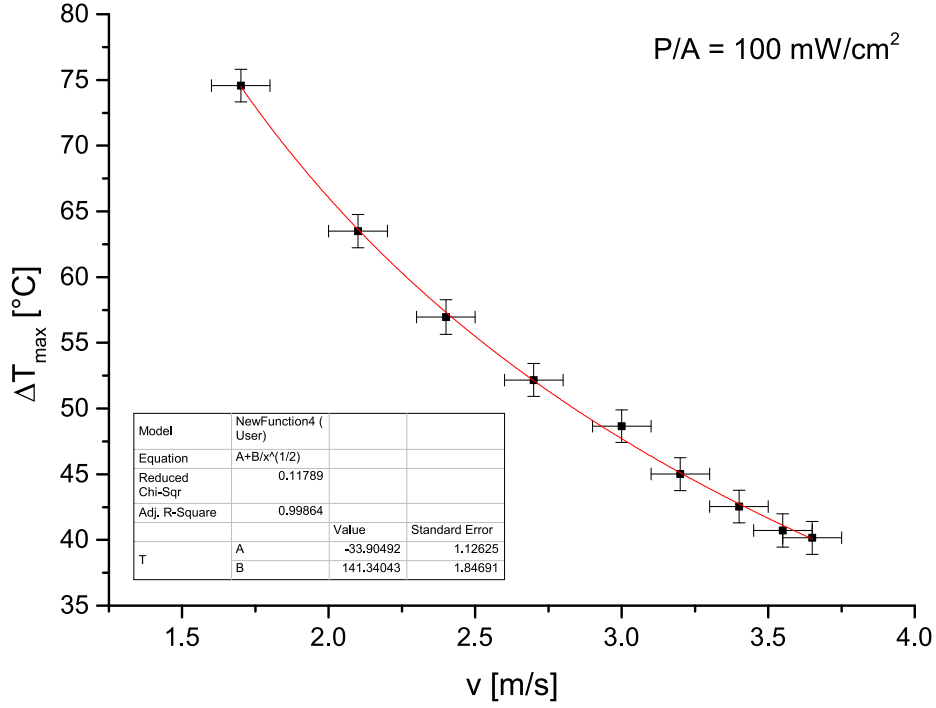
16

Figure 4.2: $\Delta T_{\mathrm{max}} = T_{\mathrm{max}} - T_{\mathrm{coolant}}$ as function of the air flow velocity at $P/A = 100 \, \mathrm{mW/cm^2}$. The air entered the system at room temperature. [29]

where $\alpha = \frac{k}{\rho c_p}$ is the thermal diffusion coefficient. An approximation of the solution for equation 4.7 assuming constant heat flux $q = -k \frac{\partial T}{\partial y}|_{y=0}$ and a laminar flow is given by

$$Nu_x = 0.453 \cdot Re_x^{1/2} Pr^{1/3} \quad Pr \geq 0.6, \tag{4.8}$$

with the dimensionless Nusselt nummber $Nu_x = \frac{hx}{k}$ [25]. This number gives the ratio of heat transfer to conductive heat transfer. The convective heat transfer coefficient is defined by $h = \frac{q}{\Delta T}$, with $\Delta T = T_s - T_\infty$. $Pr = \frac{\nu}{\alpha}$ is the dimensionless Prandtl number, which for helium is 0.664 [27]. Inserting the definitions Nu_x and Re_x into equation 4.8 yields

$$\Delta T(x)_{\mathrm{lam}} = \frac{q}{0.453 \cdot k \cdot Pr^{1/3}} \sqrt{\frac{\nu x}{v_\infty}} \tag{4.9}$$

for the temperature profile on the heated surface. A surface of finite length L, reaches the maximum temperature

$$\Delta T_{\mathrm{max,lam}} = \frac{q}{0.453 \cdot k \cdot Pr^{1/3}} \sqrt{\frac{\nu L}{v_\infty}}. \tag{4.10}$$

It is now possible to explain why the cooling capability of helium is expected to be higher than the one of air ($\frac{k_{\mathrm{he}}}{k_{\mathrm{air}}} \approx 6$).

Previous experimental studies could verify the relation $\Delta T_{max} \propto \frac{1}{\sqrt{v_\infty}}$ for a heated cylinder barrel cooled with a laminar flow on the inside and the outside [28, 29]. One result of these measurements is shown in figure 4.2. The heated prototype was cooled with air at room temperature.

Figure 4.3: Prototype of inner detector half without silicon sensors

4.2 Mechanical Design

The Mu3e experiment requires a mechanical design with a firm structure while using the ultra thin materials, to decrease effects of multiple Coulomb scattering. For the same reason, all electronic wires and coolant supplies need to be guided through inactive volumes of the detector. Furthermore, the detector should be segmented to enable easy maintenance and assembly of the detector.

In the following, the detector structure will be build up piecewise starting from the center going to larger radii. The functionality of each detector part was already explained in section 3.3 and will not be explained again, except it is relevant to the cooling system. In order to simplify descriptions regarding the pixel tracker, we define the term segment as: sandwich of a 19 mm wide flexprints constisting of 25 µm thick polyimide film and aluminium foil plus HV-MAPS glued and bonded on top. The segments' lengths and the amount of sensors can vary for the different layer of the tracking detector. Since the HV-MAPS width will be larger than 19 mm, there will be an overlap to the adjacent segment.

The core structure of the detector are two aluminium beampipes with 66 mm diameter, placed on a common axis with enough space in between both ends to fit the stopping target and the surrounding inner tracking detector. Only one of these beampipes is used to supply

18

Figure 4.4: Prototype of Layer 3 module with $50\,\mu m$ thick glass plates to simulate the flexibility of silicon. The shown, outdated prototype has only one V-fold.

a positive muon beam while the other one can be used to exchange the stopping target. In the end, each detector component will be attached to the beampipes.

The inner two pixel layer consist of eight and ten segments with $12\,cm$ active length[2], which are arranged as prism sides with regular polygons as bases. Both ends of the segments are glued to polyetherimide (PEI) endrings, which are split in half for easier assembly and possible maintenance. A prototype of an inner detector half can be seen in figure 4.3. Studies with prototypes using $50\,\mu m$ glass plates as silicon substitute, showed that this system is already self supporting and does not require additional strengthening. Since the entire detector is flooded with gaseous helium, the inner double layer separates three helium volumes; inside Layer 1, between Layer 1 and Layer 2 as well outside layer 2. As the circumscribed circle diameter of Layer 2 is about $68\,mm$, which is slightly larger than the beampipes diameter, cooling with forced convection will be challenging for the inner detector. Both layers are screwed to a mounting system, which includes an inlet system for the helium flow in between the layers, and is then attached to the beampipe.

Figure 4.5b shows the planned design for power lines and helium supply as well as for the read out cables. These parts need to fit into very limited space between the beampipe and the tile detector. For this reason a complex tubing system for the helium supply has been designed using irregular polygon shapes. It is possible to build these structures with carbon fibre materials. A detailed description of the helium circuits, is given in the next section.

The next detector part going further outwards is the timing system. Particularly important for the cooling system is the scintillating fibre detector, because it divides the helium volume between the outer and inner double pixel layer into two separated ones. In regards to the cooling system, this most likely means having individual cooling circuits for the two separated areas.

---

[2]Length covered with MuPix sensors

The third pixel layer consists of 24 segments with an active length of 340 mm and the fourth pixel layer consists of 28 segments with an active length of 360 mm. In order to simplify the assembly and maintenance of these layers four segments are combined to one module (see figure 4.4). It has proven useful to increase the stability of these outer modules by adding two triangular shaped prisms made of 25 μm thick polyimide foil underneath each segment. In regard to the cooling system, this creates the possibility to add further helium flows within these so called V-folds. Each module is completed by gluing the segments to PEI endpieces, which have an integrated helium distribution system for the V-folds. This system will be discussed in detail in section 5.1.

The outer double layer and the scintillating detectors are mounted to an endring, which is finally attached to the beampipe. Feed throughs for helium and electronics are integrated into this ring as well.

The rest of the volume ending with the inner wall of solenoidal magnet is free space only filled with helium.

4.3 The Cooling Concept

The latest design of the cooling system is the result of solving spatial limitations due to the mechanical design and the experiences gained by previous studies with pixel layer prototypes. Some decisions motivated by the latter will be discussed in the paragraph below.

Previous Studies for the Cooling System

First attempts to cool parts of the detector were performed by one single flow through the detector. Experiments and simulations provided consistent and positive results that it would be possible to cool the system via forced convection [24, 28, 29]. They also proved helium to be a superior coolant compared to air. One example of these results can be seen in figure 4.2, showing that the presented theory of convective cooling is accurate.

Furthermore, the performed simulations highlighted areas of low velocities which were not supplied with a reasonable gas flow [30]. Cooling might still be sufficient, but increasing the flow through these regions could be an improvement. This affects the inner double layer in general, because the beampipe hinders the gas flow, and the gap between the outer double layer. One possible adjustment was tested in a previous thesis [30] and could improve the temperature distribution. The next step was to add a flow in the V-folds, which were already used as mechanical strenghtening [6]. This lowered the temperatures of the module prototypes even further [29]. The decision to add a second V-fold underneath each segment was motivated by simulations testing different V-fold types [30].

Besides, improving the cooling system it was investigated whether the cooling system influences the functionality of the pixel detector. In particular, flow induced vibrations due to the flow in the V-folds were studied and the results showed unproblematic vibrational amplitudes as long as the helium velocity stayed below 30 m/s. For a constant flow of 20 m/s the average amplitudes were below 2 μm [31, 32]. The influences of a global flow over the detector are not tested yet.

4.3.1 Helium Flow Circuits

The description of the flow circuits focuses on the central detector station. Though in regard to the cooling system the recurl stations of the detector are just simpler versions of the central one, since there is no inner pixel layer which requires cooling. Tubing and distributing the helium is designed similar; hence it is possible to draw some conclusions for the entire detector. Nevertheless, testing all stations in a row will be a step in the future.

The cooling system contains six different flow channels. A schematic of the flow concept is presented in 4.5a and a view along the beampipe showing the tubing design is shown in figure 4.5 . The tubing as seen in figure 4.5b is symmetric coming from up or downstream. The volume outside Layer 4 ending with the magnets inner walls is referred to as the global volume. It is planned to have a helium flow in this region, but due to the large volume it is considered to create this flow in a surface close region only.

Coming from downstream helium flows through the green coloured tubes (see figure 4.5b) into the gap between Layer 3 and Layer 4. This type of flow is referred to as gapflow. After passing through the station, the helium is blown radially outwards into the global volume and eventually pumped out of the magnet volume and through a heat exchanger, which is connected to a cooling unit. This unit lowers the helium temperature back down to 0 °C, before it is reused to cool the detector.

The same tubes coming from the opposite direction are used to supply the gap between Layer 3 and the scintillating fibre detector. After passing through the station the gas is blown radially outwards into the global area as well. Two things should be noted. First, there is no official design for the inlet or the outlet to this volume. Neither are the exact dimensions of the scintillating fibre detector. However, since design options are limited due to the lack of space, the future design will only vary in some details from the used one in this thesis. Second, the opposite flow direction compared to the gapflow between Layer 3 and Layer 4 is chosen for spatial reasons rather than for physical ones.

The cooling system is completed by flows from downstream to upstream through the V-folds of Layer 3 (red) and Layer 4 (yellow) as well as through the gap between Layer 1 and Layer 2 (grey). These circuits are closed, meaning helium is not exhausted into the global volume but flows through the corresponding tubes on the opposite site of the detector to the cooling units. In principle, it would be possible to change the flow directions for these circuits, but the inlet and outlet have slightly different designs, and thus changing the direction might change the flow distribution.

The current design does not include helium flows for the area within Layer 1 or for the gap between Layer 2 and the scintillating fibre detector. For this reason the flow direction through the gap between Layer 1 and Layer 2 can be chosen in any direction, since it does not affect other flows in the active region.

4.3.2 Helium Flow through Non Circular Tubes

The presented cooling system does not involve one single regular tube with circular cross section. Apart from the difficulties of manufacturing these polygonal tubes, it is an involved problem to determine the type of flow through them. At least to a first approximation the
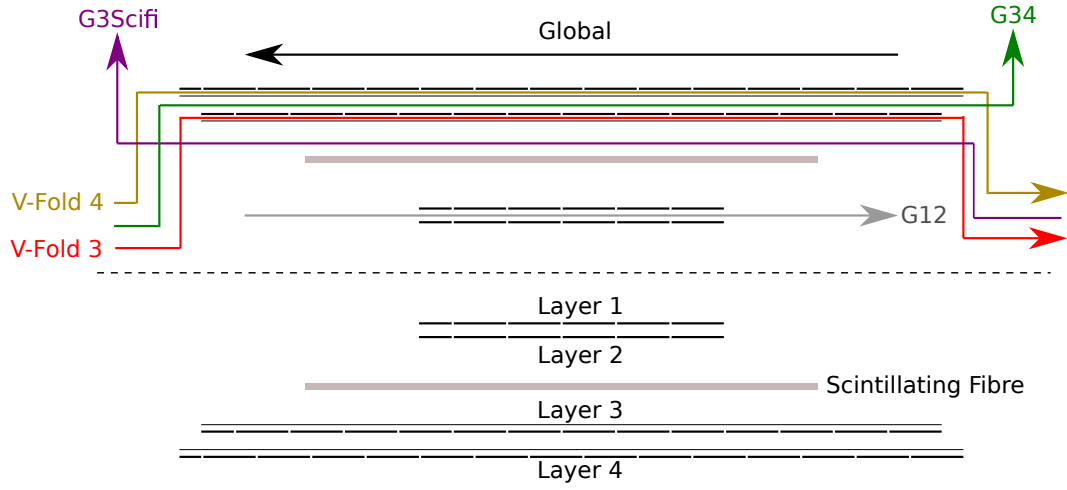
(a) Flow directions through the central station
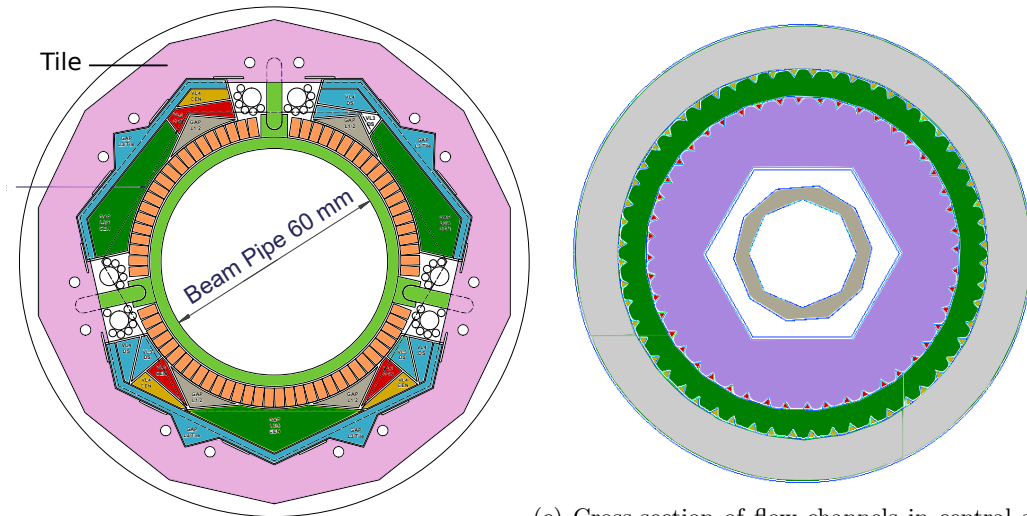
(b) Tubing and wiring

(c) Cross-section of flow channels in central station

Figure 4.5: Schematic of the flow directions and flow channels for the central station. Description of the flows by colour: green = Gapflow between Layer 3 and Layer 4, grey = Gapglow between Layer 1 and Layer 2, dark purple = Gapflow through Layer 3 and scintillating fibre, yellow = Flow through Layer 4 V-folds, red = flow through Layer 3 V-folds, black/grey = global flow. In (b) blue indicates further tubes used to supply the recurl stations, light green indicates the beam pipe and light purple the scintillating tile detector. The scales of (b) and (c) do not match.

Flow channel	He flow speed m/s	Cross-section cm²	Volumetric Flow 10^{-3} m³/s	Reynolds number
Gap L1/L2	10	12	12	<1200
Gap SciFi/L3	5	105	53	<2700
V-folds L3	20	$0.7 \times 24 \times 2$	20	400
Gap L3/L4	10	60	60	<2000
V-folds L3	20	$0.7 \times 28 \times 2$	23	400
Total		238	168	

Table 4.1: Characteristics of the different flow channels

results of circular tubes can be applied to noncircular tubes by using the hydraulic diameter

$$D_h = \frac{4A_c}{P},$$ (4.11)

where A_c is the cross-section area of the tube and P is the so called wetted perimeter [25]. The wetted perimeter is defined as the sum of the lengths of each surface in contact with the fluid. Since the tubes will be fully filled with helium this equals the circumference of the cross-section. Using this quantity as the characteristic length in equation 4.1, it is possible to calculate the Reynolds number. For equilateral triangles (V-folds) it is $D_h = \frac{a}{\sqrt{3}}$, where a denotes the length of one triangle side. For the other flow channels it is possible to use the hydraulic diameter of an annulus, which gives an upper limit for the polygonal shapes. It is defined as $D_h = D_{\text{outer}} - D_{\text{inner}}$, with D being the diameters of the inscribed circles of the polygon cross-sections. A summary of the different flow velocities and approximate Reynolds numbers is given in table 4.1. The necessary values for these calculations are $\nu = 1.23 \cdot 10^{-4}$ m²/s (helium at 300 K [27]), $a = 4$ mm, polygon side length of layer module $p \approx 19$ mm and the diameter the scintillating tile detector $D_{\text{scifi}} = 80$ mm [3].

The critical Reynolds number for a flow through a circular tube is $Re_c \geq 2300$ [25]. So in case of the V-folds and the gap flow inside the inner detector it is reasonable to assume laminar flow. For the gap flow through the outer detector the decision is a bit more complicated. Neglecting the V-folds leads the given upper limit approximation in table 4.1, which means the flow could be in a critical regime where any perturbation can cause a transition from laminar to turbulent flow. Using the exact calculation for the hydrostatic diameter, including the larger wetter perimeter due to the V-folds, however, leads to Reynolds numbers of about 1000, indicating laminar flow. The question is whether one can trust the hydrodynamic diameter, which is an approximation, for this complicated geometry. Furthermore, the critical Reynolds number could be lower due to the sharp edges of the V-folds.

These considerations are, however, only valid for the flow in the station and not for the distribution system. The distribution systems into the detector volumes are not optimized with smoothed edges and will definitely create turbulences.

Another important dimensionless number is the Mach number M, which indicates if a flow can be assumed as incompressible. It is defined as

$$M = \frac{v}{a},$$ (4.12)

---

[3]This value is only valid for the design used in this thesis

23

where a is the speed of sound [25]. For helium under standard conditions this value is about $1000\,\mathrm{m/s}$ [33]. For each flow in the detector the Mach number is below 0.3, which is the commonly used upper limit for incompressible flow [25]. Therefore, it is reasonable to assume incompressible flow inside the detector.

Chapter 5

Computational Fluid Dynamic Simulations

The theoretical treatment of problems like the helium flow through the Mu3e detector or the heat transfer by forced convection is very complex because it requires solving the three-dimensional continuity equation, Navier-Stokes equation and energy equation. The fact that the cooled detector ideally reaches a thermodynamic equilibrium and, hence, the solutions are time independent, does not simplify the problem much.

One practical way to still make theoretical predictions is to use Computational Fluid Dynamics (CFD). The software chosen for this task is Autodesk CFD® [34], which is available in a free version for students. The Autodesk CFD®software uses the Finite Element Method (FEM), which is a numerical technique to find approximate solutions to boundary value problems for partial differential equations.

FEM subdivides a complex problem into a finite number of simpler, individual sub problems, that are called finite elements. Each element is defined by a number of points called nodes, which are also the contact points to adjacent elements. The overall pattern of elements is referred to as mesh, which is an approximate equivalent to the real structure. The behaviour of each element in the simulation is described by a submatrix and to obtain results for the overall problem the software needs to solve the combined matrix of all submatrices. Superfluous details should be excluded, so that the analysis is not unnecessarily complicated. The solutions of the simulations are just approximations of the real problem, but it is possible to improve the results by increasing the amount of elements representing the structure.

In principle, the described method is capable of predicting both laminar and turbulent flows, but in the Autodesk CFD®software it is necessary to choose one type for the simulation. As discussed in the previous chapter the fluid flows through the active detector region are laminar, but the flow through the inlet system will create turbulences. Therefore, most simulations are performed for a turbulent and incompressible fluid flow. However, it is tested whether the differences of laminar simulations and turbulent simulations can be neglected for the problem under consideration.

The methodical sequence for setting up and running a simulation in Autodesk CFD®will

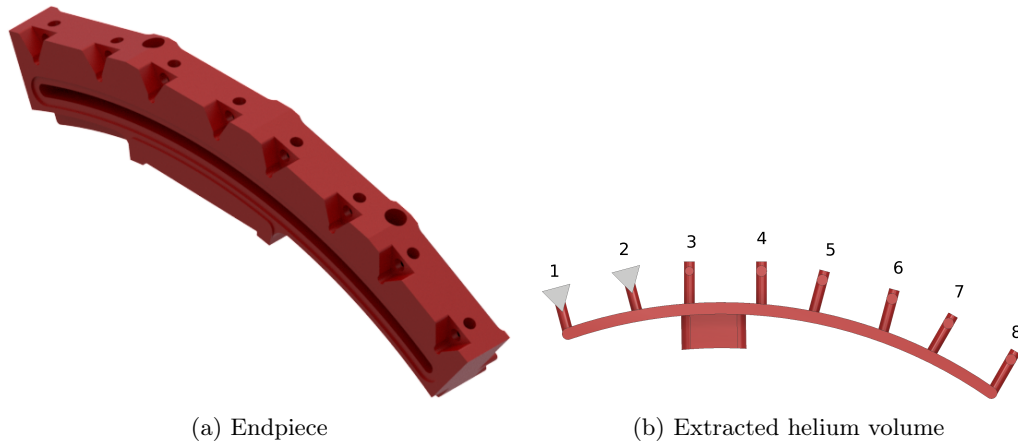(a) Endpiece   (b) Extracted helium volume

Figure 5.1: CAD model of (a) Layer 3 endpiece without simplifications and (b) the extracted helium volume inside the endpiece with two indicated V-folds

be presented below for the local helium flow through the V-folds.

5.1 Helium Flow Simulations

In order to understand the results, i. e. the temperature profile, of the simulations performed with convective heat transport, it is important to study how the helium flows through the detector. Once the flow distribution is known, it might be possible to improve the system. This section focusses on the local helium flow through the V-folds of Layer 3 and Layer 4 and the gap flows inside the double layers. The flow through the gap between Layer 3 and the SciFi will not be discussed in the context of this thesis, since the design for the inlet and the outlet is only preliminary. As soon as the dimensions and inlet systems for this flow channel are specified, the effects on the presented results need to be investigated.

5.1.1 Local Helium Flow

The distributor for the local flow through the V-folds is integrated into the PEI endpieces of the modules (see figure 5.1). Helium enters the endpiece through a large inlet on the bottom side and flows into a banana shaped volume. It should be noted that the inlet is not placed in the middle, but about 15° to the side. This is a necessary step to create more space for the readout connections. Consequently, one can presume higher velocities in the V-folds close to this inlet. From the banana shaped region helium flows through eight equally sized channels into the V-folds.

The first step towards the simulation is to create a Computer Aided Design (CAD) of the structure, which is then imported in the CFD software. The model of the local flow simulation represents the extracted helium volume of 340 mm long triangular V-folds with endpieces on both ends. Neglecting the surrounding material reduces the run time and by default the Autodesk CFD®software interprets the surfaces of this model as boundary walls. The next step is to specify the materials of each part, which in this case is simply Helium. Afterwards, the boundary conditions like the inlet velocity or initial temperature of the gas
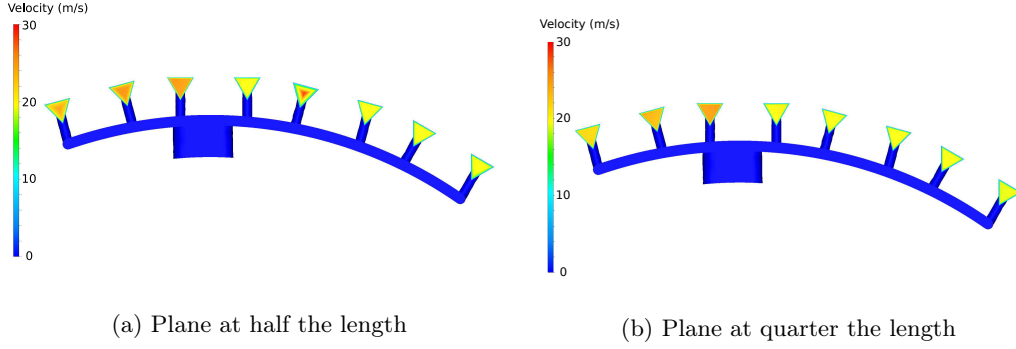
(a) Plane at half the length

(b) Plane at quarter the length

Figure 5.2: Cross-section of the simulated helium flow at half and quarter of a module's length. The average helium velocity through the V-folds is $20\,\mathrm{m/s}$.

need to be defined. The planned velocity for the gas flow through the V-folds is $20\,\mathrm{m/s}$ and the inlet velocity can be easily calculated using the conservation of volumetric flow:

$$A_{\mathrm{in}}v_{\mathrm{in}} = A_{\mathrm{out}}v_{\mathrm{out}} = 8 \cdot A_{\mathrm{fold}}v_{\mathrm{fold}}, \qquad (5.1)$$

with A being the cross-section of the inlet. The necessary outlet on the opposite end of the module is defined by setting zero overpressure.

The mesh for the simulation can be created automatically by the software or manually by the user. Additionally, the Autodesk CFD®software offers a technique called Mesh Adaptation , which progressively improves the mesh definition based on previous simulations. By default, this is performed three times, but it is possible to change the number of cycles. An ideal result is mesh independent, meaning small changes to the mesh do not change the results significantly. Since the same problem is simulated multiple times with refined meshes, this technique requires more time than one simple run. As an example, the time for the currently discussed design differs from about three minutes to more than one hour when performing three adaptation runs. The question whether it is necessary to spent additional resources for this technique will be discussed in the following paragraph.

Mesh Adaptation Mode

Working with mesh adaptation can increase the run time significantly. Simply comparing the same set-put simulated with and without mesh adaptation shows whether it is reasonable. This test is performed for Layer 3, but the results are equivalent for both outer layers. Figure 5.2a shows the plane with the velocities at half of the module's length and Figure 5.3 shows the plotted velocity distributions for the two different methods on this plane.

There is one significant difference between both simulations; the velocity in the fourth V-fold from the right is significantly lower for the simple run. Not running the simulation with mesh adaptation could therefore lead to wrong assumptions. In regard to design changes this is problematic. This example proves that it is reasonable to use mesh adaptation for set-ups comparable to this one. More complex structures with significantly higher elements number will not be performed with this technique, since the run time would exceed any practical limit. However, experiences with the simulations show that complex structures
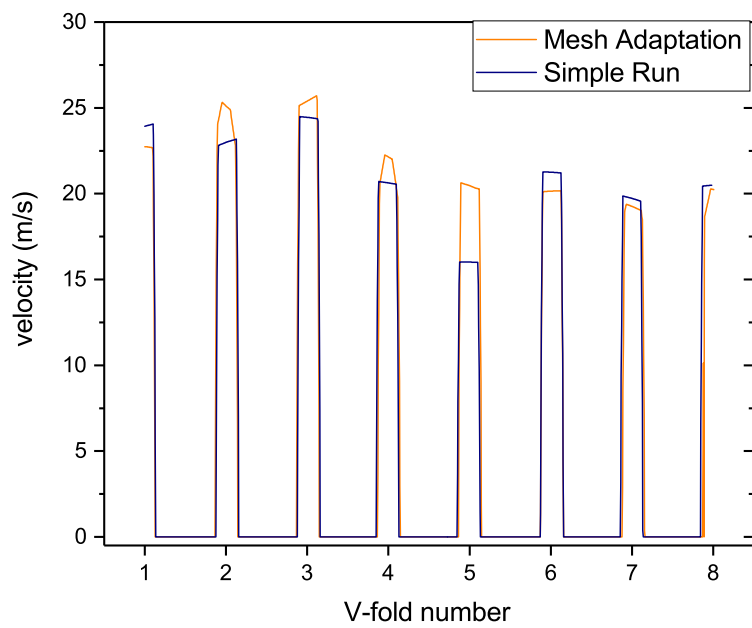
Figure 5.3: Velocities for simulated helium flow through a Layer 3 module with and without mesh adaptation at half the length of the module. The expected flow velocity is $20\,\mathrm{m/s}$. The horizontal scale represents a length scale in millimetres, but for easier identification of the individual V-folds, the labelling is replaced with numbers. Compare to figure 5.1b .

have finer automatic meshes, which reduces the necessity for mesh adaptation.

Even though mesh adaptation is a great tool, using this technique does not guarantee realistic results. This can be seen in figure 5.3. At half the length of the V-folds, the velocity profile in V-fold number 4 is star shaped. In contrast, none of the other channels shows a similar profile and at quarter of the length this feature disappears. This is problematic because the mean velocities at these two lengths vary by up to 0.5 m/s, which is unexpected for a non compressible flow. Unfortunately, the Autodesk CFD®software can not determine the mean velocity through a volume, which would average over these variances, but only for planes. Since artefacts like this randomly appear at different lengths and for turbulent and laminar simulation modes respectively, this will be taken into account as an error for the mean velocities in the simulation.

Laminar Flow

As mentioned before the simulations are performed for a turbulent model, even though the flow through the V-folds is laminar. Another comparison will show that the velocities in turbulent flow and laminar flow only differ on a negligibly scale. The velocity profiles for both flow types at half the module's length are shown in figure 5.4. Furthermore, the mean velocities are calculated and added to the plot. The error of about 0.5 m/s is motivated by the varying mean velocities as discussed above.

One can see that the mean velocities are similar and only the flow pattern varies, which is likely caused by the different models used to calculate the boundary layer. As an example, the flow profile in circular tubes is parabolic for laminar flows and almost flat for turbulent flow. Since the mean velocities are similar it seems reasonable to keep working with turbulent simulations to test the optimized endpiece.

Improvements to the Flow Distribution

Until now the velocities through the V-folds varied by almost 5 m/s and as expected the flow through the folds closest to the inlet is higher. Since applying changes to one part of the distributor affects the entire flow pattern, improving the system is mostly based on trial and error. The direct approach is to limit the flow through the V-folds with higher velocity in order to increase the flow through the others. This can be done by using smaller drill holes for the outlets into the V-folds like presented in figure 5.5. Options for the diameters are limited to 0.1 mm steps due to commercial availability of these drill sizes. The goal is to only have maximal variations of 10 %, equalling 2 m/s. The results of the most promising change are presented in figure 5.6. For the optimized design the highest velocity differences are about 10 %. The improvement will also be verified with activated heat transfer in section 5.2.1.

Other possible changes like widening the outlet into the V-fold or narrowing the banana shaped region can not compete with the presented design, because they are either difficult to manufacture, involve several changes or did not improve the flow pattern significantly.
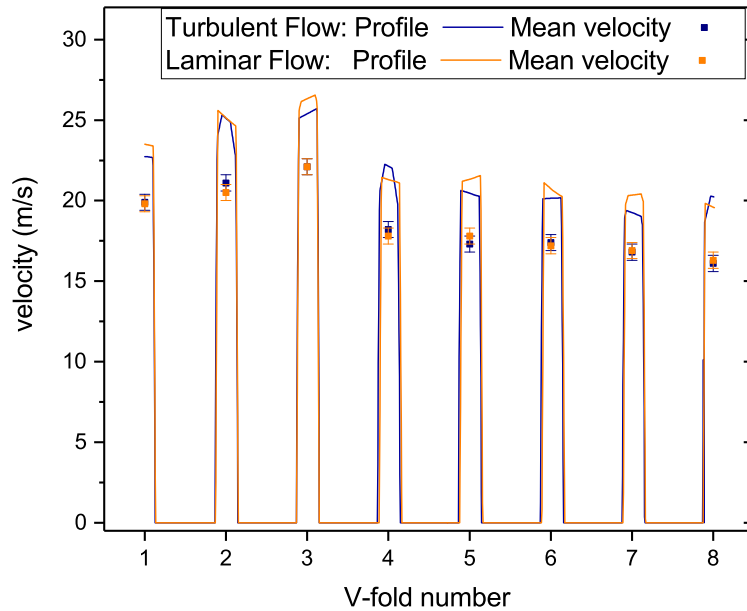
Figure 5.4: Simulated helium flow through a Layer 3 module for laminar and turbulent flow. The expected flow velocity is 20 m/s. The horizontal scale represents a length scale in millimetres, but for easier identification of the individual V-folds, the labelling is replaced with numbers. The plot shows the velocity profile and the average velocities.
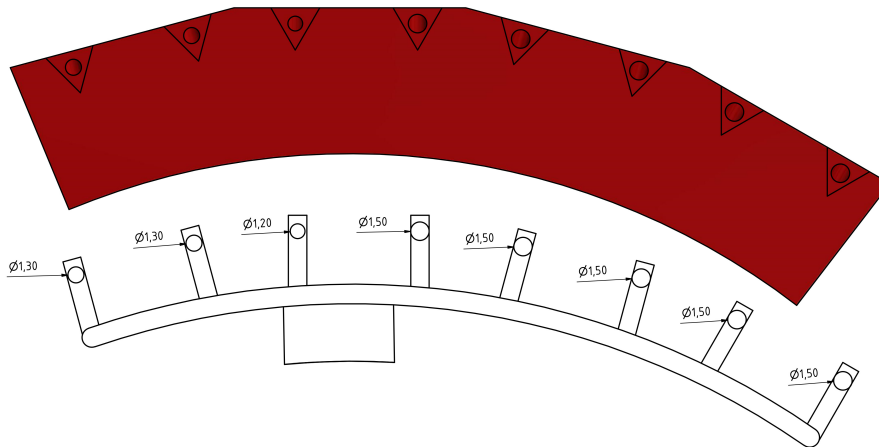

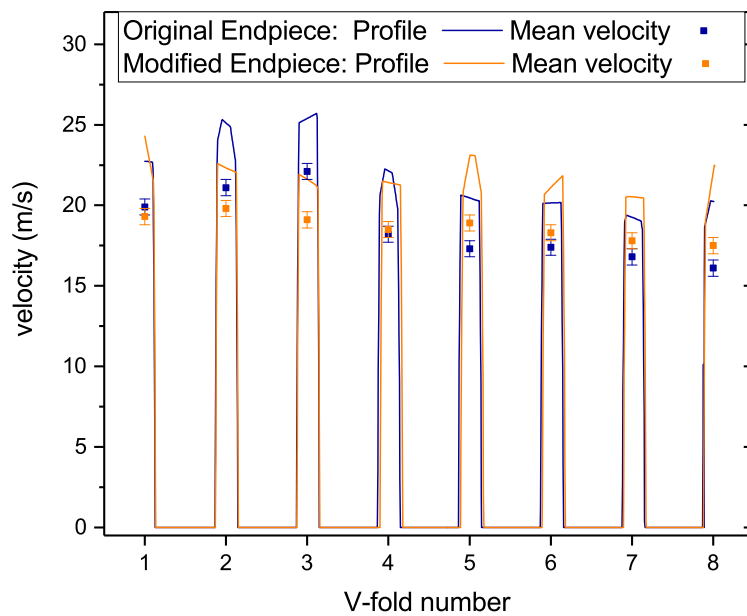Figure 5.5: Technical sketch of the optimized endpiece. The original design used eight drill holes with 1.5 mm diameter.

Figure 5.6: Simulated helium flow through a Layer 3 module for regular and optimized endpieces. The expected flow velocity is 20 m/s. The horizontal scale represents a length scale in millimetres, but for easier identification of the individual V-folds, the labelling is replaced with numbers. The plot shows the velocity profile and the average velocities.
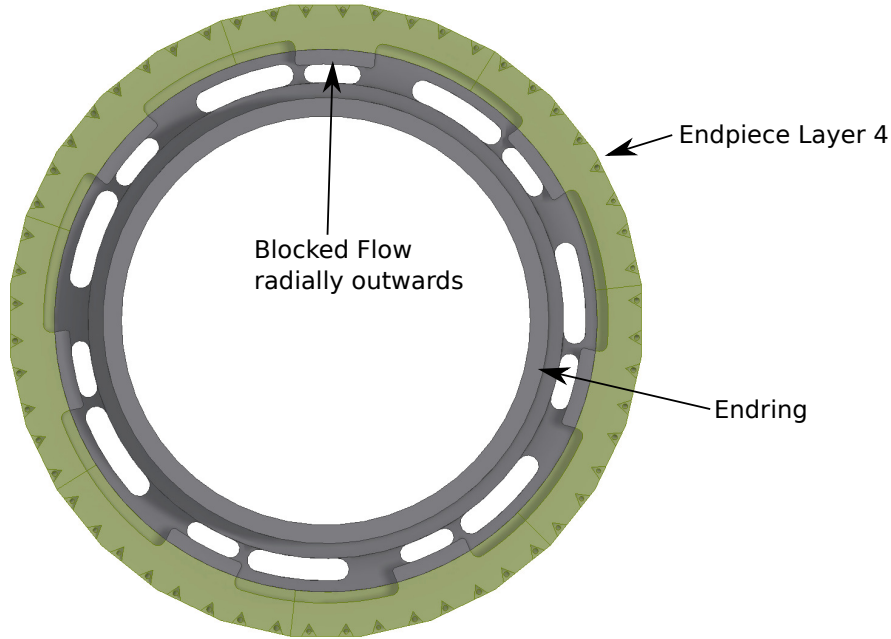
Figure 5.7: Endring with integrated helium feed through and Layer 4 endpieces. Indicated is one of the seven obstacles hindering the flow radially outwards into the gap region.

5.1.2 Gapflow through the Outer Double Layer

An additional helium flow through the gap between Layer 3 and Layer 4 was first introduced in the master thesis of Yanwing [30]. The initial design used small holes, drilled into the module endpieces, to supply a helium flow to this gap. The main disadvantage was the high inlet velocity necessary to create a sufficient gas flow, i.e. a flow of $4\,\mathrm{m/s}$ in the gap required an inlet velocity of $200\,\mathrm{m/s}$. Instead of further increasing the inlet velocities, the new design uses larger inlets (compare eq. 5.1, conservation of volumetric flow), which are now integrated into the endring (see figure 5.7).

How the helium streams into the gap is best explained with the help of visualisation, since there are a few obstacles affecting the flow.

The two outer layers have a difference in active length of $20\,\mathrm{mm}$, so their endpieces are shifted by one centimetre on each end of the layer (see figure 5.8). This provides enough space for helium to flow past the endpieces into the gap area. It should be noted, that due to the electronic wiring of Layer 4 there are seven regions where the helium flow is deflected by the Layer 4 endpieces (visible in figures 5.7 and 5.8). A similar problem occurs on the other side of the endring, where helium needs to flow around the tubes providing coolant to the V-folds of Layer 4 (visible in figure 5.9).

The extracted helium volume of the entire gap flow is presented in figure 5.9, including the exhaust which blows the helium radially outwards into the global volume.

The parameters for this simulation are:

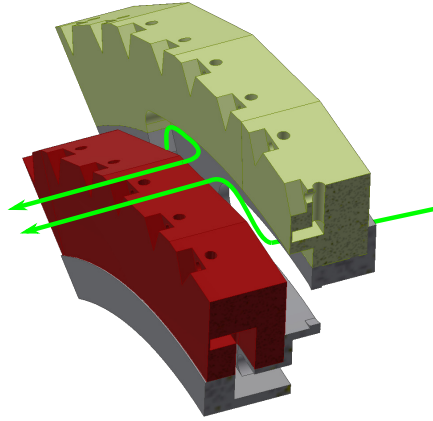- average velocity in gap region $v = 10\,\mathrm{m/s}$

Figure 5.8: Flow through the endring into the gap between Layer 3 and Layer 4. Indicated is the undisturbed flow and the flow which is deflected by the recess needed for the Layer 4 read out.
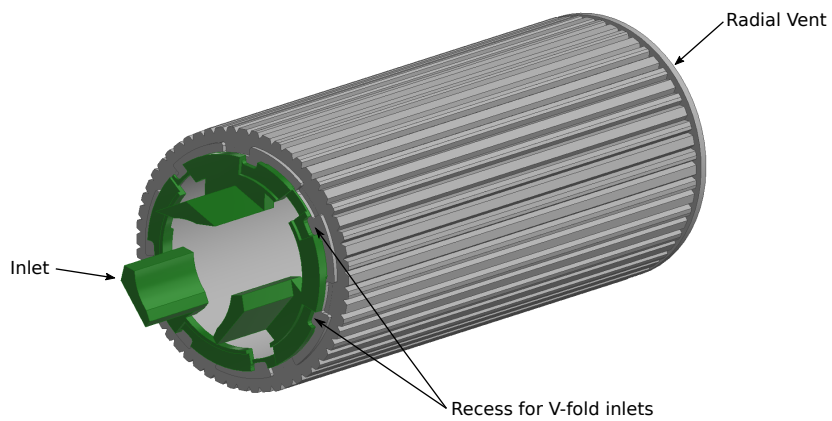

Figure 5.9: Extracted helium volume of the gapflow through the outer double layer including the inlet and outlet system. Indicated is the recess, which is needed to create space for the helium supply of the Layer 4 V-folds.
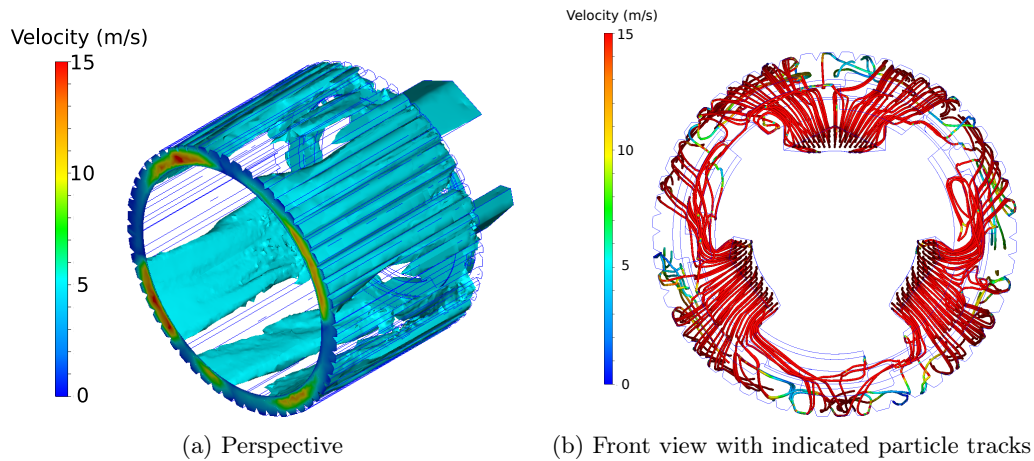
| (a) Perspective | (b) Front view with indicated particle tracks |

Figure 5.10: Visualisation of the low velocity regions in the gap flow through the outer double layer. The average velocity in the gap is 10 m/s. In (a), everything coloured in light blue has a velocity higher than 5 m/s and blank spaces have velocities below this value. In (b), the *particles* flow around the four low velocity regions

- zero overpressure for radial exhaust

- Mesh adaptation disabled

The simulation shows that the velocities in the gap region are unevenly distributed ranging from almost zero to above 15 m/s. In order to visualize regions of low velocity, the gas volume with velocities above 5 m/s is coloured in light blue (see figure 5.10). This reveals four main regions of low velocity on the inlet side, which are almost 90° apart from each other. Since variations in the flow distribution will also affect the temperatures in the detector, it is important to understand their origin. The Autodesk CFD®software is capable of indicating fluid particle tracks and vectorial flow directions. An exemplary use of particle tracks is shown in figure 5.10b. It is shown how the fast helium *particles* coloured in red flow around the four low velocity regions. With this technique it is possible to find the inlet system for the Layer 4 V-folds being the cause of these low velocity regions. Like an obstacle in a fast river, these features create regions of low velocities and eddies directly behind. There is one explanation why there are four and not seven low velocity regions. In three cases two helium flows from different directions merge directly behind the obstacle, and therefore the velocity does not drop as strong.

Any changes to the inlet system most likely involve changes to the entire detector mechanics and cooling design. Therefore, it is tested first, how significant these low velocity regions are for the temperature profile.

5.1.3 Gapflow through the Inner Double Layer

The helium flow through the gap between the two inner layers is currently the only planned active cooling of the inner detector, which is mainly due to the lack of space for additional ducts. In contrast to the gapflow through the outer double layer, helium leaves the inner detector via tubes on the opposite side. Also in contrast to other flows, there are four instead
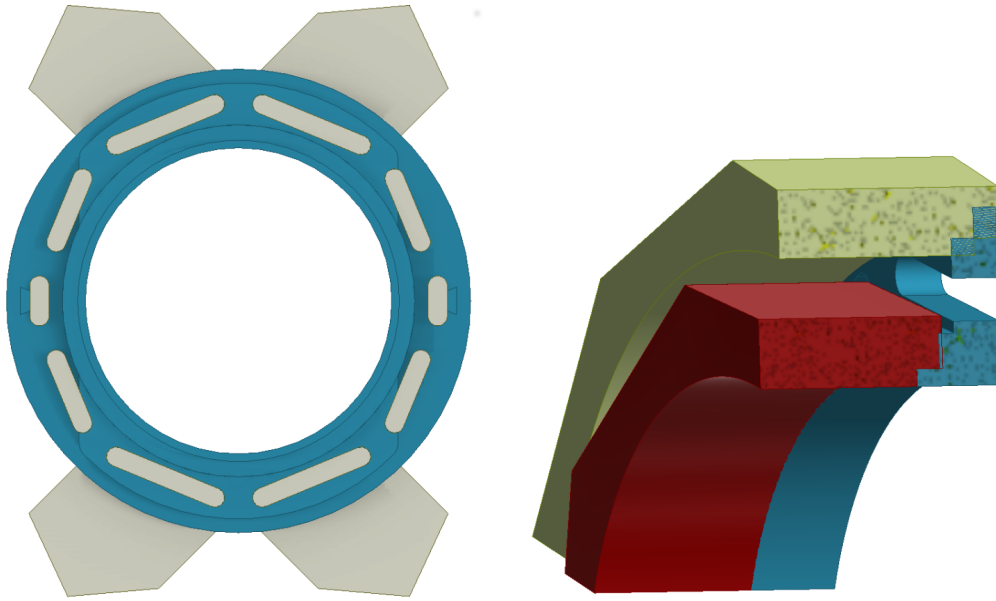
(a) Front view with drawn supply tubes (grey) (b) Cut section to visualize the space for the flow

Figure 5.11: CAD drawing of the inner double layer endring

of three tubes (see Cooling concept in section 4.3.1).

The inlets and outlets are integrated in the endring (see 5.11a) and helium needs to flow through a space between the endpieces (see figure 5.11b). The parameters for the simulation are:

- velocity in gap region $v = 10\,\text{m/s}$

- zero overpressure

- Mesh adaptation enabled

First studies with this set-up indicate that it is reasonable to run the simulation with mesh adaptation in order to reach mesh independent results.

The simulation results show an uneven flow distribution for this gap flow as well. Using the same techniques as before, each volume with velocities above $5\,\text{m/s}$ is coloured in light blue (see figure 5.12a). One can see that the flow velocities are low for the regions furthest away from the inlet tubes (compare 5.11a). In order to explain the later temperature profile, the flow directions are visualized with vectors in figure 5.12b. This reveals a large vortex in the helium flow, which appears on both sides of the detector. Due to the size of the vortex, which reaches through the entire length of the layer, one can already presume negative effects for the cooling system.

Once again changing the flow pattern involves changes to the endring and possibly the tubing. The effects of this helium flow on the temperature profile and two possible methods to further lower the temperature will be presented in section 5.2.2. For one of these methods it is intended to prevent the vortex.
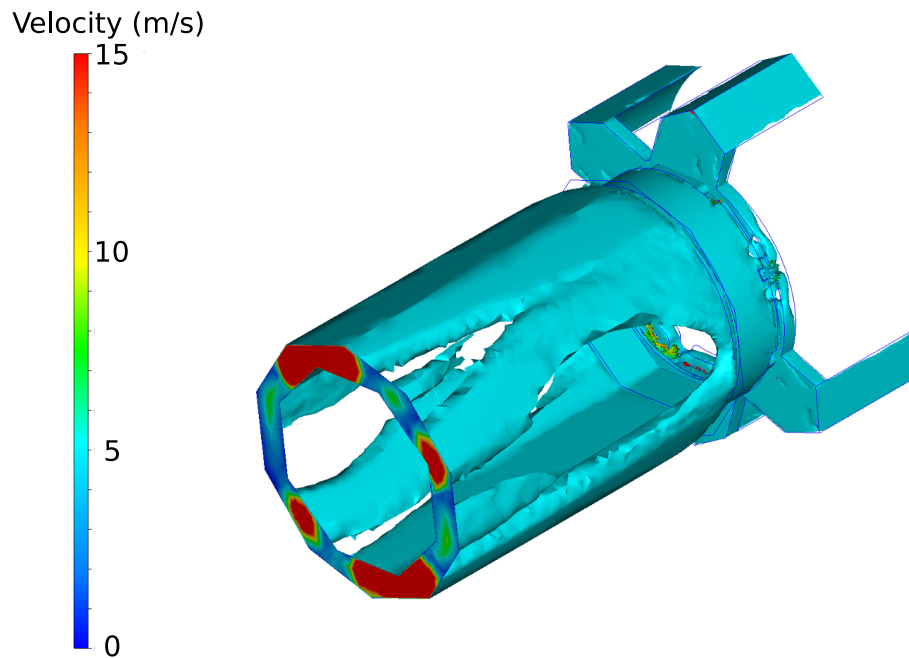
(a) Cross-section through the inner detector. Volumes coloured in blue indicate velocities above 5 m/s and thus blank regions have velocities below this value
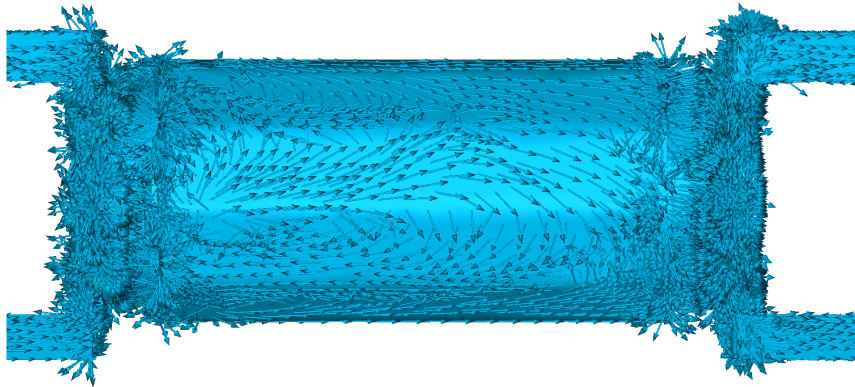
(b) Flow pattern visualized with the vectorial directions of the velocity. The chosen colour is not connected to the velocity.

Figure 5.12: CFD simulation results for the flow through the inner detector with an average velocity of 10 m/s.
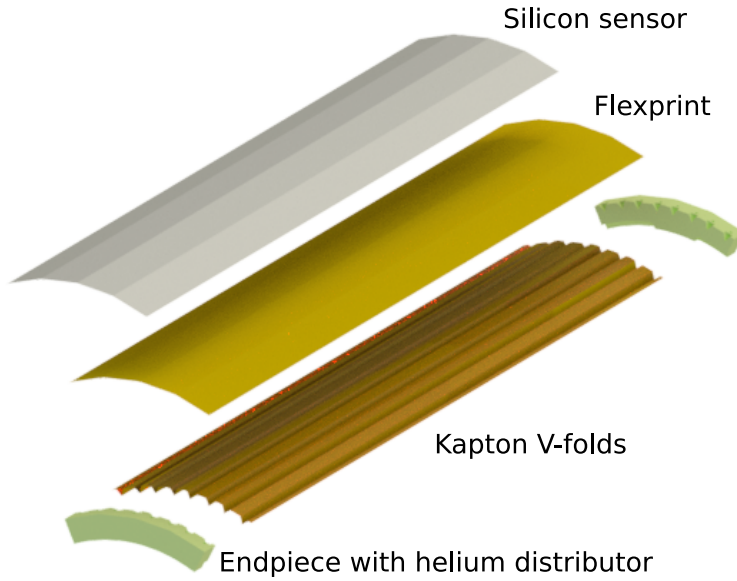
Figure 5.13: CAD explosion sketch of a Layer 4 module

5.2 Thermal Analysis of the Cooling System

The most important question in this thesis is, whether the presented cooling systems will be capable of keeping the temperatures of the tracking detector in a reasonable range. The expected heat load for the final MuPix is about $250\,\text{mW/cm}^2$, but a more conservative estimate of $400\,\text{mW/cm}^2$ will be tested as well. This will not only establish a margin for possible higher power consumption, e. g. caused by higher operating frequencies, it will also show if the temperature of the detector is linearly proportional to the power consumption. Performing simulations including heat transfer increases the complexity of the simulations significantly because it is now necessary to add all the individual parts, e. g. the endpieces, polyimide foil and silicon chips. The properties of most materials are already implemented in the Autodesk CFD®database, but polyimide needs to be added manually. The properties of the most commonly known polyimide foil Kapton®[1] are listed in table 5.1 .

Property	Value
Thermal Coefficient of Linear Expansion	$2.0 \cdot 10^{-5}/\text{K}$
Coefficient of Thermal Conductivity	$0.12\,\text{W/(m\,K)}$
Specific Heat	$1.09\,\text{J/(g\,K)}$
Density	$1.43\,\text{g/cm}^3$
Young Module	$2.6\,\text{GPa}$

Table 5.1: Properties of $25\,\mu\text{m}$ thick Kapton®polyimid film at $296\,\text{K}$ [35]

5.2.1 Thermal Analysis of a Single Module

It is useful to start off with a single module, before heading directly to the entire detector, because changes and simplifications of the design can be tested at lower computation time.

---

[1]Kapton®is a registered trademark of E.I. du Pont de Nemours and Company

Since the modules of Layer 3 and Layer 4 are similar, only one type will be presented in this section. Figure 5.13 shows an explosion drawing of the used CAD model of the Layer 4 module. It consists of two endpieces, V-folds made of 25 µm thick polyimide foil, a 50 µm thick flexprint dummy and a 50 µm thick layer of silicon. The following simplification to the real module are made:

- Parts like screw holes are neglected.

- The flexprint is simulated as 50 µm thick polyimide foil and aluminium traces are neglected

- The endpieces are simulated as ABS[2], which is already included in the software, instead of PEI plastics

- The silicon layer is made of one solid layer with dimensions of 19 mm × 360 mm for each side. Overlaps between chips are neglected

First it is tested, whether the optimized endpieces (see section 5.1.1) improve the temperature profile. The following parameters are used for the simulations:

- flow velocity through V-fold $v = 20$ m/s

- helium enters at $T = 0\,°C$

- zero overpressure for outlet

- Heat load per surface area $P/A = 250$ mW/cm^2

- Mesh adaptation enabled

- No additional helium surrounding the module

Even though the dimensions of the simplified silicon are smaller than the ones of the prior introduced MuPix, the power dissipation per surface area will not be adapted in order to have similar absolute values. This is motivated by two factors. First, the exact dimensions and final power consumption of the MuPix are yet unknown. Second, later in this thesis it will be shown that the temperature is proportional to the power consumption, so the exact power consumption does not matter at this point. It will also be tested whether using a uninterrupted silicon layer is a reasonable simplification.

The temperature profiles of the Layer 4 modules with optimized and original endpiece are presented in figure 5.14. Due to the applied changes the module heats up more evenly in flow direction.

As a metalloid, silicon has a high thermal conductivity (148 W K/m [25]) and working with a solid, uninterrupted silicon layer means allowing this type of heat transfer for the entire module. This could result in a different temperature profile, which might not match a simulation with MuPix chips. To test whether this is an issue, an alternative silicon layer is drawn with individual sensors with dimensions of 19×19.8 mm^2. These chips are placed with a gap of 0.2 mm to the adjacent sensor. Both models will be simulated with the same

---

[2]Acrylonitrile butadiene styrene is a common 3D printer material
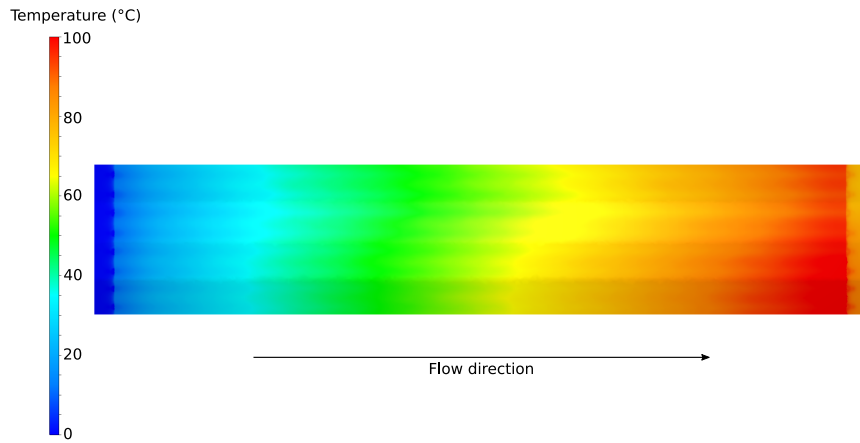
(a) Original endpiece design
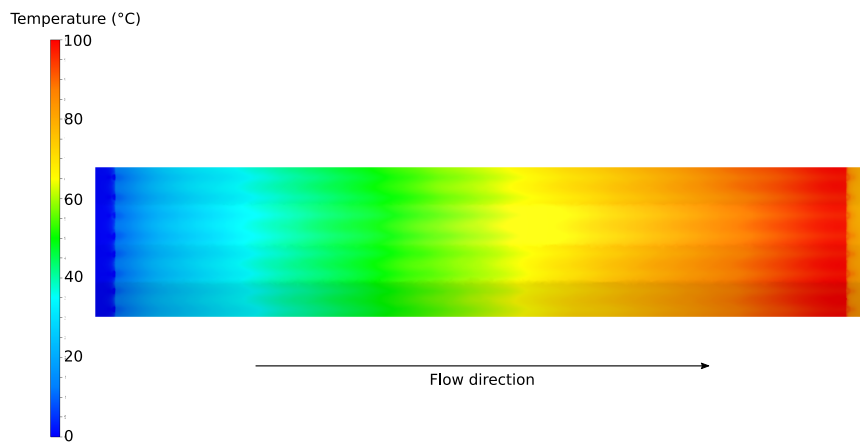
(b) Optimized endpiece design

Figure 5.14: Surface temperature of a heated Layer 4 module cooled with local helium flow of $20\,\text{m/s}$ through V-folds. The initial helium temperature when entering the detector is $0\,°\text{C}$. The module is heated with $250\,\text{mW/cm}^2$ and the model is not surrounded by further helium volumes.
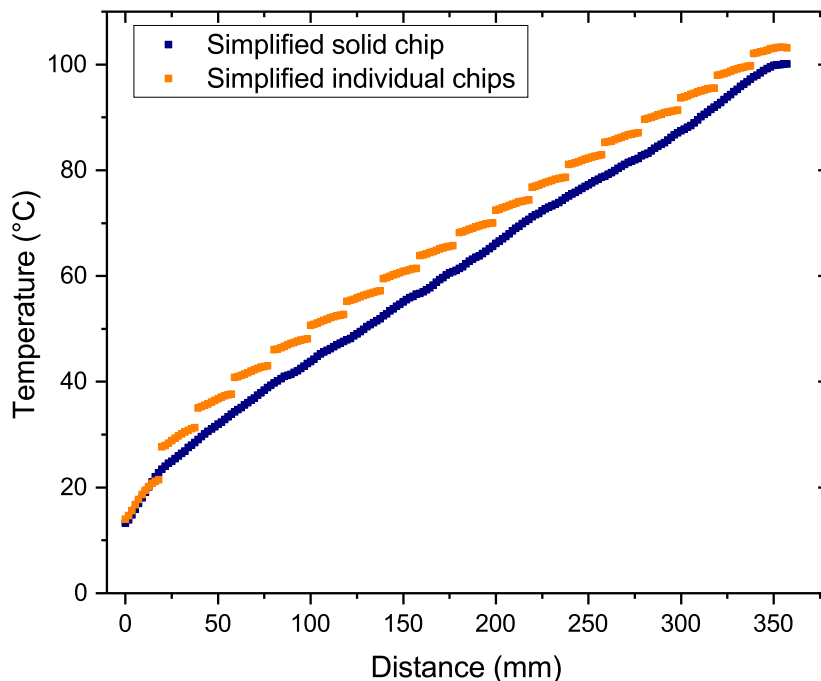
Figure 5.15: Temperature of the silicon sensor as a function of the module's length. The module is heated with $250\,\mathrm{mW/cm^2}$ and cooled by a helium flow of $20\,\mathrm{m/s}$ through the V-folds. The initial helium temperature when entering the detector is $0\,^{\circ}\mathrm{C}$.

parameters as used above, which means the total heat dissipation for the individual sensor module is expected to be slightly lower.

Figure 5.15 shows the temperature over the module's length for both sensor types. It can be seen nicely how the temperature chips increases from one individual chip to the next. Even though the total power consumption of the single chips are slightly lower, their temperatures are higher. This is most likely due to the interrupted thermal conduction. The maximal temperature difference between both silicon designs is about $6\,^{\circ}\mathrm{C}$, which can be kept in mind as a systematic error for the simulations. However, the overall difference between the individual chip and the single solid layer is small.

Using individual chips for this set-up already increased the number of elements by a factor of seven. But these chips are a simplification themselves and do not consider the overlap between adjacent chips (see section 3.3.1). Adding this feature would increase the element number for the detector simulations in a way that lets the runtime exceed any appropriate limits.

The temperature profile over the module shows a large gradient close to the inlet and the theoretical introduction of forced convection for laminar flow predicts the temperature to follow a square root function. This is not in accordance to the simulation results. Changing the flow type in the theoretical analysis does not change that ($\Delta T \propto \sqrt[5]{x}$) [25]. The ex-
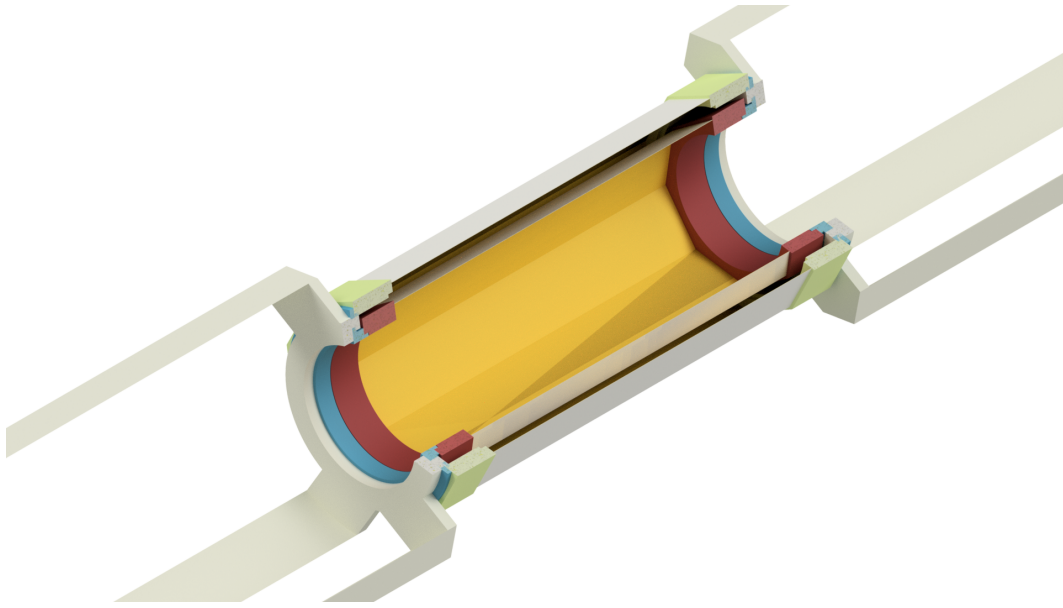
Figure 5.16: CAD drawing of the inner detector with helium ducts

planation is that it is not possible to determine the thickness of the temperature boundary layer or in other words, there is no specific temperature T_∞ that can be associated with the fluid flow. Surface temperature T_S and fluid temperate both change over the length of the silicon heater, but without detailed knowledge of the temperature boundary layer calculating $\Delta T = S - T_\infty$ is not possible.

5.2.2 Thermal Analysis of the Inner Detector

The spatial separation of the inner and outer double layer due to the scintillating fibre detector makes it possible to deal with both parts individually, and thus lowers the simulation time. Furthermore, the complexity of the inner detector is low enough to run simulations with mesh adaptation in a reasonable time. The used CAD model is presented in figure 5.16 and the same simplifications as above are applied. In particular drill holes and the separation between the layer halves are removed. Although it is not drawn in figure 5.16 the inner detector is fully surrounded by helium. The target inside Layer 1 can be neglected, since there will be no forced helium flow in this volume.

The parameters for the simulation are:

- helium flow through the gap $v = 10\,\mathrm{m/s}$

- helium enters at $T = 0\,^\circ\mathrm{C}$

- zero overpressure for outlets

- Heat load per surface area $P/A = 250\,\mathrm{mW/cm^2}$ and $P/A = 400\,\mathrm{mW/cm^2}$
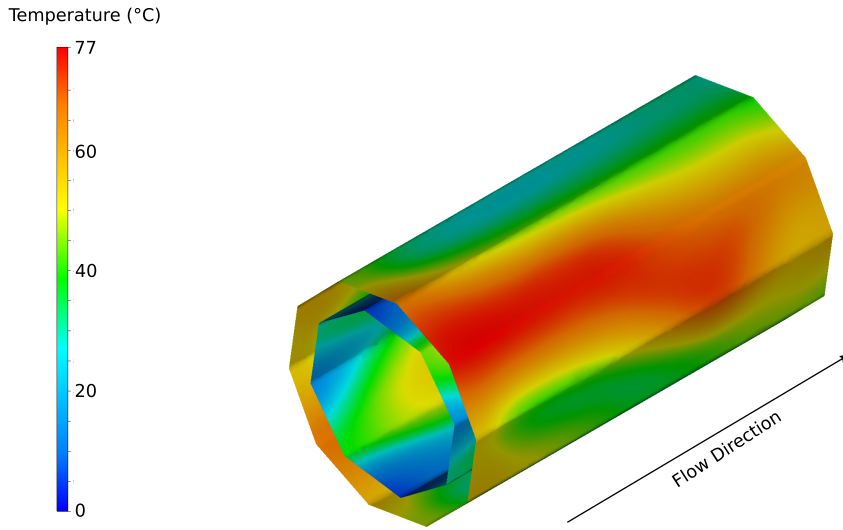
- Mesh adaptation enabled

Figure 5.17: Temperature profile for inner detector heated with $P/A = 400\,\mathrm{mW/cm^2}$. The flow direction is indicated and helium enters the detector at $0\,^{\circ}\mathrm{C}$.

Simulation Run	$250\,\mathrm{mW/cm^2}$		$400\,\mathrm{mW/cm^2}$	
	T_{avg}	T_{max}	T_{avg}	T_{max}
1	10	35	16	56
2	12	35	18	52
3	16	45	27	72
Final	17	50	27	77

Table 5.2: Temperatures in $^{\circ}\mathrm{C}$, obtained from the four stages of mesh adaptation

Mesh adaptation is used to refine the mesh three times. Including an initial simulation run, there are four simulation results that can be compared. If the final result is mesh independent, the temperature should only change on a small scale compared to the previous run. The average temperatures and the maximum temperatures for the four simulations are listed in table 5.2. These values are valid for the entire simulated model, meaning the temperature of helium or polyimide are considered as well. The maximum temperatures can be found on the silicon layer since these are the heat sources. For most cases the temperatures increase by about $60\,\%$ which equals the factor between the two applied heat loads per surface area. This means the temperature and power consumption are directly proportional to another. But the difference in the maximum temperatures between the second last and last run is still about $10\,\%$, which means the results are not fully mesh independent yet. In order to obtain these results, the simulations had to run on a cloud service offered by Autodesk, but there is a three day limit for simulation run times. The presented simulation already required about one and a half days so running additional mesh adaptation cycles, which would require more time than the previous due to the refined meshes, could exceed the time limit. Therefore, the last variation of the average temperature is taken into account as an error for the simulated results of the inner detector. This results in a $5\,\%$ error. Figure 5.17 shows the temperature profile of the inner detector with a heat load per area of

$P/A = 400\,\mathrm{mW/cm^2}$. The visible temperature profile is not as expected. Instead of having the highest temperature close to the outlet, the temperature reaches its maximum on the opposite side where cooled helium enters the detector. This can be explained by the vortex in the helium flow which guides the already heated helium from the end of the detector back to the front (see figure 5.12b). This way, the detector heats up stronger and unevenly.

A consequence of the uneven temperature profile is mechanical stress to the the detector caused by irregular thermal expansion. Due to a temperature difference ΔT a body with length L_0 changes its length by approximately

$$\Delta L = \alpha L_0 \Delta T, \tag{5.2}$$

where α is the linear expansion coefficient. The value for Kapton®is $\alpha = 2.0 \cdot 10^{-5}/\mathrm{K}$. Since the silicon chips in the real detector are separated and expand individually, the total deformation of the module is dominated by the expansion of the polyimide layers. The fact that silicon has a ten times lower expansion coefficient than polyimide causes additional problems, which will be subject of chapter 6.1.2 .

It is assumed that the detector is assembled at a temperature of $20\,°\mathrm{C}$ and each polyimide layer is initially $12\,\mathrm{cm}$ long. In the actual detector each layer is $2\,\mathrm{cm}$ longer, but we can neglect the area where poliymid film and endpiece are glued together, since it will expand differently. The mean temperatures of each segment and their linear expansion for the two different heat loads are plotted in figure 5.18 . The segments heat up similarly for the two different heat loads. However, the the average temperatures of the segments can differ by almost $25\,°\mathrm{C}$ when applying a power of $400\,\mathrm{mW/cm^2}$. This means the module expands irregular with maximal differences of almost $70\,\mathrm{\mu m}$. The consequence is mechanical stress to the glued connections; hence this could damage the detector. Furthermore, the segments can start to sag, which changes the position of the silicon chips, and thus affects the resolution of the tracking detector. The latter could be compensated by calibration runs of the detector as long as the temperatures in the detector are constant over time. In order to protect the detector from damages, it is advisable to improve the flow profile, and therefore change the temperature distribution.

Improving the Cooling of the Inner Detector

There are two possibilities to improve the cooling of the inner detector. First, one could add additional helium flows, e.g. a flow in the gap between Layer 2 and the scintillating fibres. This would, however, require additional ducts. The second option is to eliminate the vortex in the gap flow by changing the endring design.

Changing the endring has the advantage that the current design for the helium ducts is not affected. However, finding a working solution to redirect the flow can be difficult and time consuming. But there is one option that only requires minor changes to the design. Figure 5.11a shows the feed throughs in the endring and how they are oriented relative to the ducts. The smallest of these holes are on the sides where the velocity is low and the vortex forms. Rotating the ring by 90° places the small holes between the ducts and the
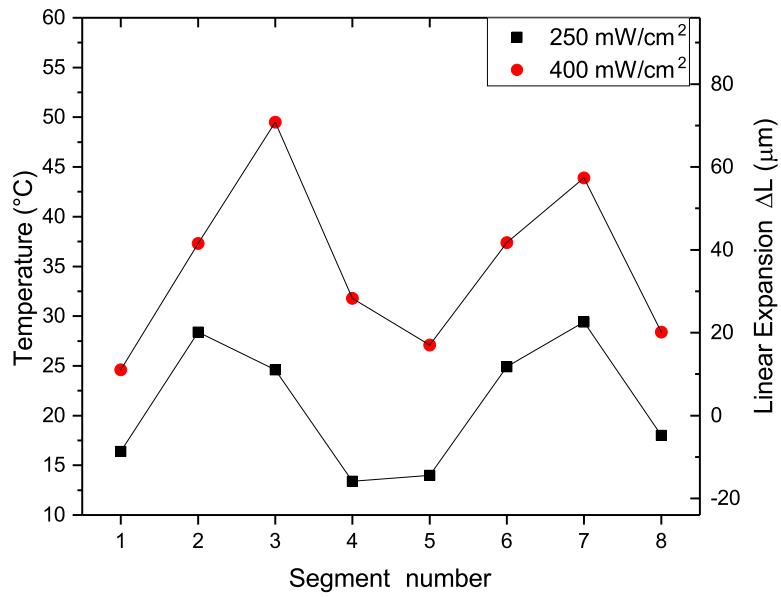
(a) Layer 1
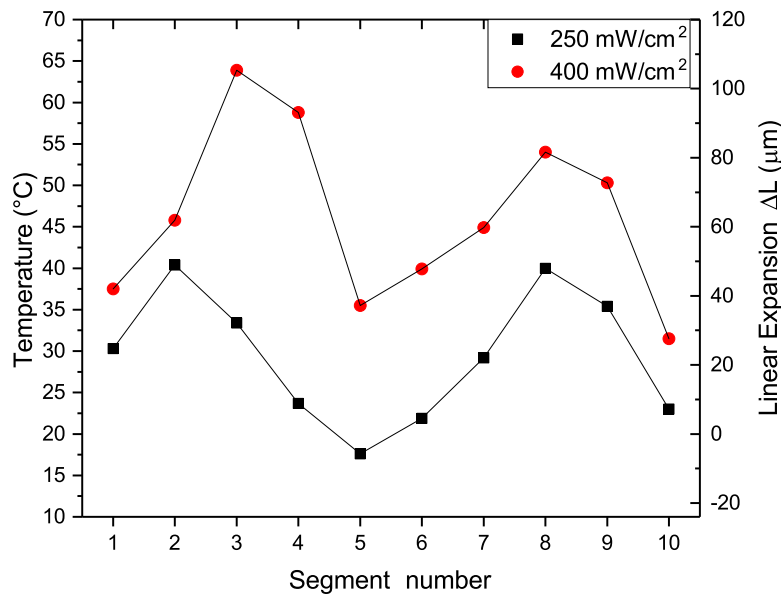
(b) Layer 2

Figure 5.18: Average temperatures of the heated inner detector segments and their linear expansion relative to 20 °C. The detector is cooled with a flow of 10 m/s, which enters the detector with 0 °C. Errors are not plotted, but the uncertainties of the simulations will be motivated.
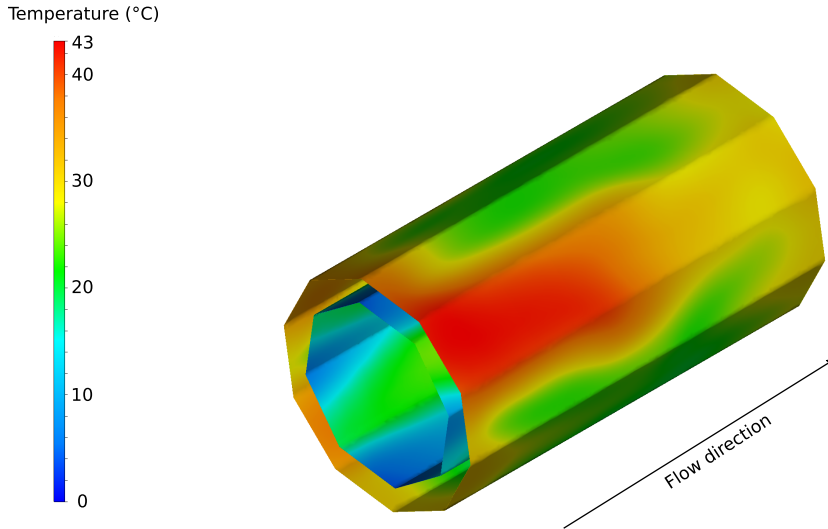
Figure 5.19: Temperature profile for inner detector with optimized endring design and heated with $P/A = 250\,\mathrm{mW/cm^2}$. The flow direction is indicated and helium enters the detector at $0\,°\mathrm{C}$.

larger in the area of low velocities. The effects of this minor change are visible in figure 5.19. This simulation was performed for $P/A = 250\,\mathrm{mW/cm^2}$ and with three mesh adaptation cycles. The maximal temperature is lowered by about $8\,°\mathrm{C}$ down to $T_{250,\mathrm{optimzed}} = 42\,°\mathrm{C}$. However, the average temperature and the temperature profile did not change significantly (compare to figure 5.17), and thus the differences in thermal expansion are not solved yet. But improving the endring seems to be the most promising method to create an evenly distributed temperature.

The second option is to create an additional helium flow between Layer 2 and the scintillating fibre (see 4.5a). Because there are no planned ducts yet, the flow is applied uniformly to the volume surrounding Layer 2. The helium velocity is set to $v = 3\,\mathrm{m/s}$ and like before the helium temperature when entering the detector region is set to $0\,°\mathrm{C}$. This simulation was performed with three mesh adaptation cycles as well. By applying this additional flow, the maximum temperature decreases to $33\,°\mathrm{C}$, but does not affect the temperature profile significantly. However, the significant improvement to the original design of about $17\,°\mathrm{C}$ shows that it should be considered to add another helium flow.

5.2.3 Thermal Analysis of the Outer detector

The analysis of the outer detector is performed analogously to the inner detector. Running simulations of this part has the advantage that the temperatures can be interpreted as results for the recurl stations as well. A CAD model of the outer detector is shown in figure 5.20. The helium volume of the global region is not drawn. As introduced in chapter 4.3.1 there are five different flows that need to be defined in the simulation. The parameter for the simulation are:
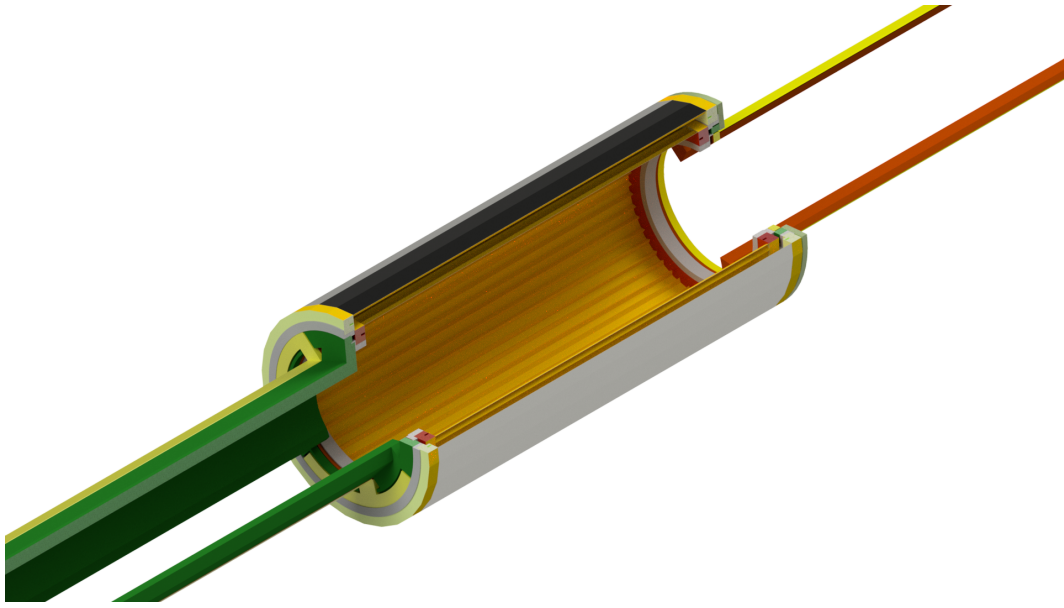
- helium flow through the V-folds of L3 and L4 $v = 20\,\mathrm{m/s}$

Figure 5.20: CAD model of outer detector

- helium flow through the gap L3/Scifi $v = 5\,\mathrm{m/s}$

- helium flow through the gap L3/L4 $v = 10\,\mathrm{m/s}$

- helium flow in the global region $v = 0.5\,\mathrm{m/s}$

- helium enters at $T = 0\,^\circ\mathrm{C}$

- zero overpressure for outlets

- Heat load per surface area $P/A = 250\,\mathrm{mW/cm^2}$ and $P/A = 400\,\mathrm{mW/cm^2}$

- Mesh adaptation disabled

For this simulation the global flow is chosen in the direction from downstream to upstream, so it will flow in the opposite direction of the other flows cooling Layer 4. However, there is no official decision yet. Furthermore, the global volume can not be simulated up the full radius of 50 cm, because it would significantly increase the runtime. For this reason, the outer diameter of this volume is set to 22 cm, which equals the dimensions of the tube that is used for the future thermal-mechanical mock-up. It is also not possible to use mesh adaptation, because the initial simulation already runs about two days on the cloud service. Performing additional mesh adaptation cycles would exceed the three day limit for simulation run times on the cloud.

The maximal temperatures for both simulations are $T_{250} = 25\,^\circ\mathrm{C}$ and $T_{400} = 40\,^\circ\mathrm{C}$. These values are in agreement with the expected direct proportional relation of temperature and applied heat load per surface area. The temperature profile of the outer detector for $P/A = 400\,\mathrm{mW/cm^2}$ is shown in figure 5.21. One can see that the outer double layer heats up stronger in four regions, which are related to the low velocity regions found in section 5.1.2. The mean temperatures as well as the linear expansion of the polyimide segments are plotted
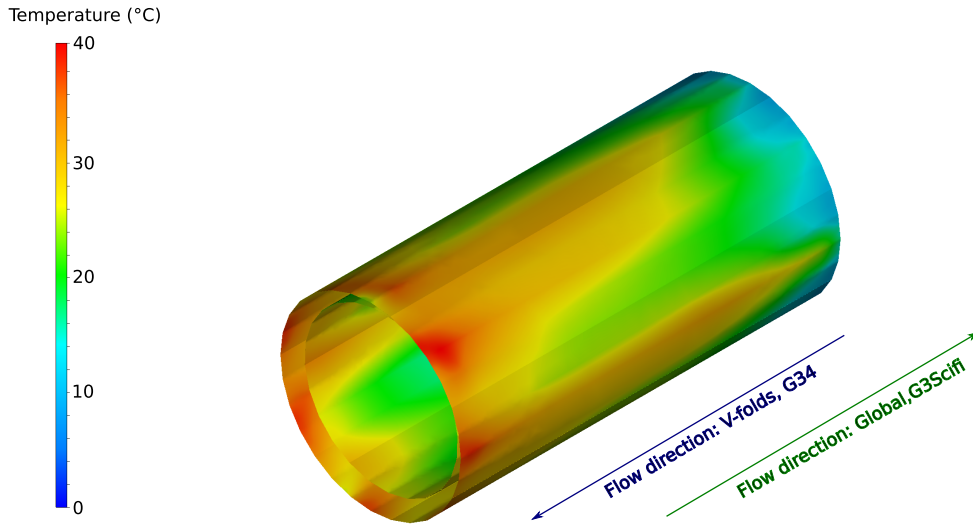
Figure 5.21: Temperature profile for outer detector heated with $P/A = 400\,\mathrm{mW/cm^2}$. The flow directions are indicated and the initial helium temperature when entering the detector is $0\,^\circ\mathrm{C}$.

in figure 5.22. The initial polyimide layers at $20\,^\circ\mathrm{C}$ are $340\,\mathrm{mm}$ and $360\,\mathrm{mm}$ long. Similar to the inner detector, there are strong variations for the thermal expansion and within one module the difference can be up to $40\,\mathrm{\mu m}$. This causes stress to the material and could damage the detector. One possible option is to improve the flow through the gap between Layer 3 and Layer 4 and minimize the differences in thermal deformation. Another solution for this problem could be to apply forces on the endpieces in order to stretch the polyimide segments to equal length. Assuming a length difference $\Delta L = 40\,\mathrm{\mu m}$ and an initial length of $L_0 = 360\,\mathrm{mm}$ the necessary force per segment $A = 0.025\,\mathrm{mm} \times 19\,\mathrm{mm}$ can be calculated via the Young module E(see table 5.1) [36].

$$F = EA\frac{\Delta L}{L_0} \tag{5.3}$$

The resulting force is about $0.14\,\mathrm{N}$ per Layer 4 segment. Consequently, a force of about $8\,\mathrm{N}$ applied on the endring of Layer 3 and Layer 4 should be sufficient to stretch away length differences of about $40\,\mathrm{\mu m}$ and this seems to be a manageable engineering task.

Variations of the Helium Flow Velocities

The two gapflows related to the outer detector have the highest volumetric flow when neglecting the global volume. If it is possible to lower the volumetric flow without significantly rising the temperature of the outer detector it might be possible to use less strong pumps and cooling units. It is tested how using only half the velocity for the gapflows affects the temperature. This is done separately for the flow through the gap of Layer 3 and Layer 4 and through the gap through Layer 3 and the Scifi. The latter is designed to cool only Layer 3 and not Layer 4, so it is necessary to compare the maximum temperatures of both layers
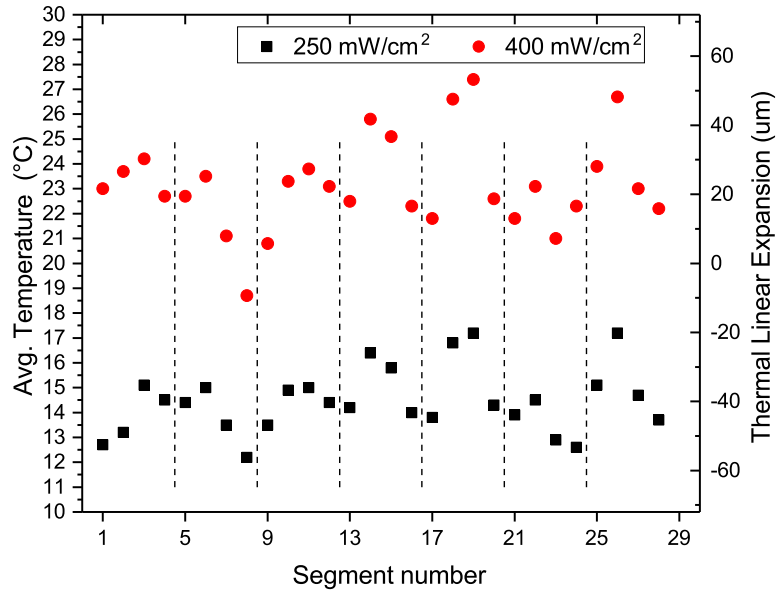
(a) Layer 3
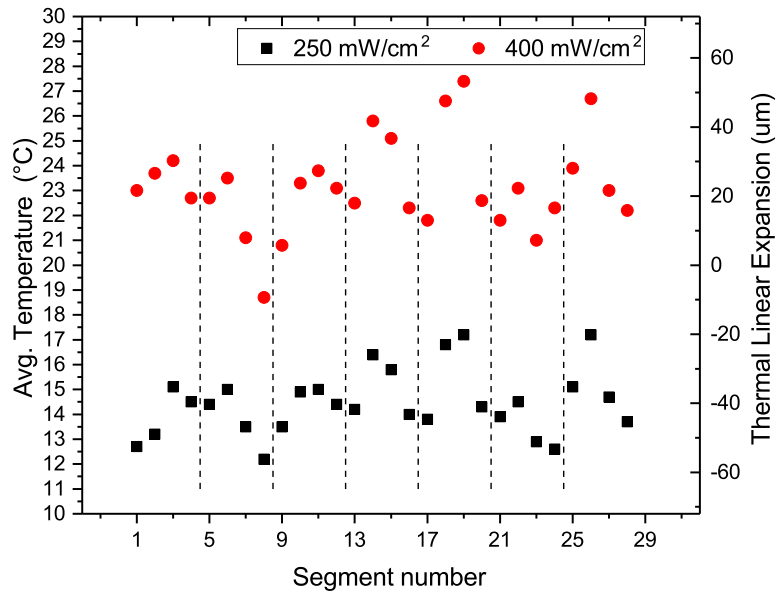
(b) Layer 4

Figure 5.22: Average temperatures of the outer detector segments and their linear expansion relative to 20 °C. Dashed lines mark the different modules. Errors are not plotted, but the uncertainties of the simulations will be motivated.

Flow Velocity	$T_{\max,\text{Layer 3}}$	$T_{\max,\text{Layer 4}}$	T_{avg}
G34: $10\,\text{m/s}$, G3Scifi: $5\,\text{m/s}$	21	25	8
G34: $5\,\text{m/s}$, G3Scifi: $5\,\text{m/s}$	30	35	12
G34: $10\,\text{m/s}$, G3Scifi: $2.5\,\text{m/s}$	23	25	9

Table 5.3: Temperatures in °C of the outer detector when using different flow velocities for the gap flows. The reference is G34 $10\,\text{m/s}$ and G3Scifi $5\,\text{m/s}$. The velocity in the V-folds is unchanged ($20\,\text{m/s}$). The detector is heated with $250\,\text{mW/cm}^2$.

as well as the average temperature of the full outer detector, when heating the silicon with $250\,\text{mW/cm}^2$. The reference is the previously introduced simulation with a flow of $10\,\text{m/s}$ through the gap of Layer 3 and Layer 4 and $5\,\text{m/s}$ through the gap between Layer 3 and the Scifi. The flow through the V-folds is unchanged and still $20\,\text{m/s}$, since their volumetric flow is comparably small. The results of the three different simulation are presented in table 5.3 . According to the dependency of the temperature to the flow, lowering the velocity by a factor 2 should lead to an increase of temperature by a factor of $\sqrt{2}$ ($\Delta T \propto \frac{1}{\sqrt{v}}$, see equation 4.10). This applies for changing the flow through the gap between Layer 3 and Layer 4. For the flow through the gap between Layer 3 and the Scifi this relation is not fulfilled, but since this flow only cools one and not both layers, it was expected to see a different result. These simulations also show that the gap flow through Layer 3 and Layer 4 has a stronger effect on the temperatures of the detector as the other gap flow. Therefore, future attempts to improve the cooling system of the outer detector should mainly focus on this flow channel.

5.2.4 Temperatures and Pressures in the Full Detector

To verify that nothing unexpected happens when combining the inner and the outer detector, simulations for the full central station were performed. For this purpose both CAD models shown above can be used, but the separation in form of the scintillating fibre detector needs to be added. This is done by a six sided prism with $1\,\text{mm}$ thickness made of polystyrene, which is supposed to be the main material [37]. All parameters for the two detector parts are chosen equivalent to their initial simulation, meaning optimized flow channels and changed flow velocities are not considered for this test. The only exceptions are the modified endpieces of the Layer 3 and Layer 4 modules. Regarding the run time, this simulation is performed without mesh adaptation.

The maximal temperatures for the inner and outer part are listed in table 5.4 . Once again both scenarios with $250\,\text{mW/cm}^2$ and $400\,\text{mW/cm}^2$ are considered and as a comparison the maximal temperatures of the individual simulations are listed as well. Comparing the results of the simulations without mesh adaptation shows that the results are mostly consistent. Therefore, it is a reasonable to assume that both inner and outer detector can be studied individually. The small divergence for the outer detector is most likely caused by the changed mesh due to the additional contact surfaces between the detectors. This could be ruled out when running a simulation with mesh adaptation, but this is currently not possible due to the three day limit for simulation run times on the cloud service. The increased temperatures of the inner detector, when running with mesh adaptation indicates that increased temperatures for the outer detector need to be presumed as well. However, these changes

49
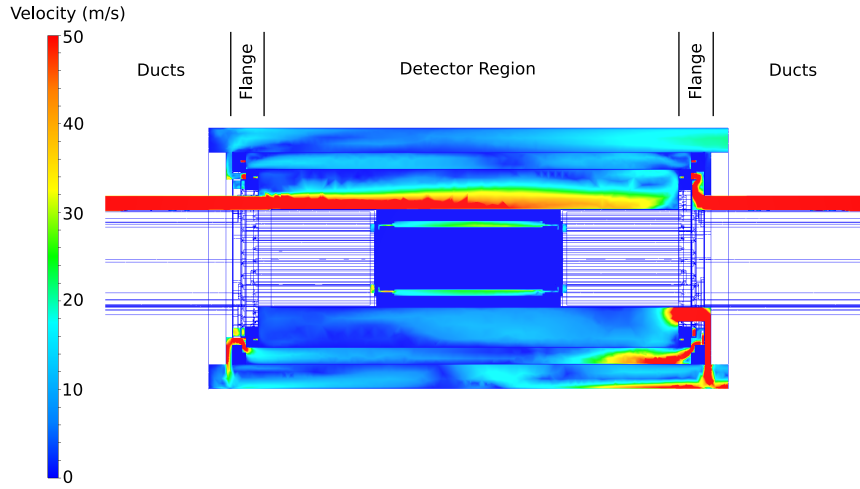
(a) Layer 3
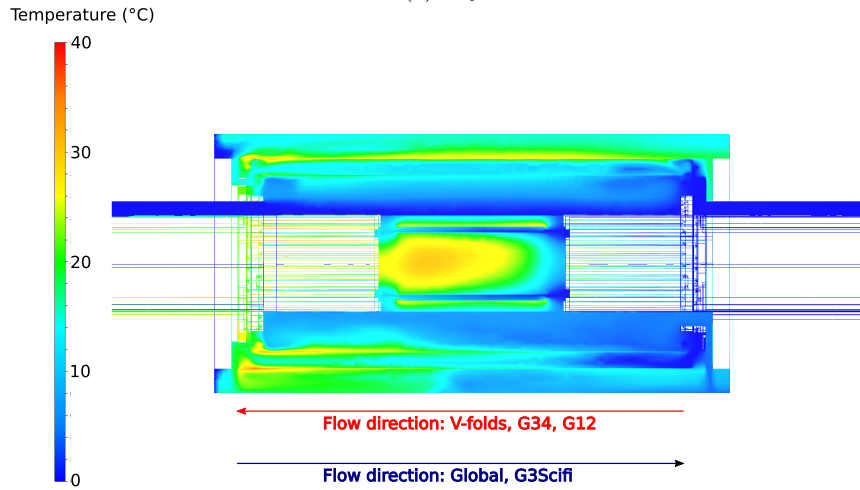
(b) Layer 4

Figure 5.23: Transversal cut through the central station's velocity profile (a) and temperature profile (b). Indicated are individual regions of the outer detector for ducts, flanges and the detector region. A flange consists of endpieces and endrings. The ducts in this picture are shortened. The detector is heated with $400\,\mathrm{mW/cm^2}$

		$250\,\mathrm{mW/cm^2}$	$400\,\mathrm{mW/cm^2}$
Individual Simulation	Inner Detector	35	50
		50	*77*
	Outer Detector	25	40
Combined Simulation	Inner Detector	34	50
	Outer Detector	25	38

Table 5.4: Maximal temperatures in °C for the inner and outer detector when simulated individually and combined. The italic numbers for the individual inner detector are the temperatures after running mesh adaptation. The other values represent simple simulation runs.

Circuit	Duct IN	Flange	Detector	Flange	Duct OUT
Gap L1/L2	25	7	<1	9	24
Gap L3/Scifi	6	<1	3	28	-
V-Folds L3	25-50	80-90	25	10-20	25-35
Gap L3/L4	8	25	<1	11	-
V-folds L4	30-50	60-70	10-20	50-70	20

Table 5.5: Pressure drops over different sections of the detector in mbar. The different sections are indicated in figure 5.23a. Each flange consists of a combination of endpieces and endrings.

do not necessarily have to be as large as for the inner detector, but even if they were, an increase in temperature of 50 % for the outer detector would still be below the 70 °C limit. At this point, it is seems reasonable to wait for first experimental results to test whether it is required to run more precise simulations.

A transversal profile of the velocities and temperatures is shown in figure 5.23. One can see how the temperatures are distributed in the detector and the different layers can be identified via the increased temperature surrounding them. On the bottom-right side, one can see how the helium flows in to gap area between Layer 3 and Layer 4 and how the helium is exhausted radially outwards. Since the global volume is restricted to a smaller diameter, one can see how the helium reflects off this boundary. Since the warmed helium is then blown over the surface of Layer 4, the temperatures of Layer 4 could be lower in the final set-up. The high velocities of 50 m/s are usually reached in narrowed regions like the ducts and inlet systems. One exception is the flow coming from the left-hand side which is part of the gapflow between Layer 3 and the scintillating fibre detector. The preliminary design for the inlet allows the gas to flow into the gap region without being distributed evenly. Since this can affect the temperature distribution the gapflow needs to be further studied, once an official design for the inlet system exists.

The temperatures of the detector will be relevant for the final experiment in two ways. They need to be within the operating range of the MuPix sensor and the gradients of their distribution should be small to minimize mechanical stress due to expansions of the system. But apart from the temperature, pressure differences in the detector can possibly damage the system as well. Table 5.5 lists the pressure drops for different sections of the detector like the ducts or the distribution system. These sections are indicated in figure 5.23a. The pressure is mostly obtained from the individual simulations of the outer and inner detector, because the pressure seems to be the most mesh dependent variable in the simulations. So using the results of mesh adapted simulations whenever existing is reasonable. In some cases it is necessary to give the minimum-maximum range, because due to the unsymmetrical design of the ducts and inlet systems, the pressure can vary. The gap flows of the outer detector vent into the global volume and therefore no value is given for *duct OUT*. The reason why the pressure drop for the V-folds is not symmetrical to the detector center is due to a slightly different design of the inlet and outlet system.

Too high pressure differences between layers are critical because of their ultra thin design. For example a higher pressure in the V-folds relative to the surrounding gap flow could cause the folds to blow up like balloons. This creates stress to the glued connection and repeatedly

starting the cooling system could cause damages. As an example a pressure difference of 1 mbar between both sides of a Layer 4 segment ($1.9 \times 36\,\mathrm{cm}^2$) corresponds to a force of $F = 0.68\,\mathrm{N}$ or a weight of about 68 g. In contrast, the segment alone only weights about 1.3 g. The maximum deformation can be determined with the Euler–Bernoulli beam theory. We assume a 360 mm and 19 mm wide beam made of 25 μm thick polyimide layer which is fixated on both ends. The maximum displacement in the center is

$$h_{\max} = \frac{12qL^4}{384Ebh(b^2 + h^2)} \tag{5.4}$$

with the uniformly distributed load q, the lenght L, the thickness h, the width b and the elastic module E (Young Module, see table 5.1) [38]. With $q = 1.9\,\mathrm{N/m}$ being the uniformly distributed load over then length, the maximal central displacement for one segment is $h_{\max} \approx 2\,\mathrm{mm}$, which should not cause any trouble to the mechanics but to the track reconstruction. It should be noted that this estimation does not consider the additional strengthening by the V-folds.

For the simulation it was assumed that helium is pumped in on one side and that the outlets have zero overpressure. However, instead of having zero overpressure at the end of the tubes it would be better to have zero overpressure in the center of the detector. This can be accomplished by installing pumps on both ends of the detector, one pumping helium in and one pumping helium out of the system.

The results of this chapter indicate that the cooling system still needs to be optimized and further studied. In particular, the inner detector can heat up to temperatures above 70 °C and its temperature profile is irregular. This causes high variations in thermal expansion and creates mechanical stress. The problems for the outer detector are similar and additionally due to the lack of computational power the results have a high uncertainty. Regarding, the errors it is important to keep the simplified silicon layers in mind, which will increase the temperature. Furthermore, the simulations are not mesh independent yet, but more detailed simulations require more computational power. Improving the different gap flows through the detector will solve most of the presented problems regarding the deformation and, therefore, this will be an important task for the future.

Chapter 6

Heater Elements

Simulations offer a great tool to investigate how the helium flows through the detector and how it might be possible to lower the temperatures in the detector. But they are just approximations and some neglected details might affect the cooling system. Other problems like the actual deformation of the detector or possible vibrations are complicated to test in simulations. There might be a theoretical approach, but performing an experiment is more reliable.

The goal is to build a full thermal-mechanical mock-up, which can be used to study the cooling system and validate the results of the simulations. Instead of actually using valuable MuPix chips the prototype will consist of two types of modules. The first kind is made of silicon chips with the same dimensions as the MuPix, but without any pixel electronics. Since producing a full detector out of pure silicon chips is still costly, most modules will consist of tape heaters, a special laser edged aluminium-polyimide laminate.

In the first part of this chapter the Silicon heater is characterized and in the second part first experiments with the tape heaters are presented.

6.1 Silicon Heater

In future cooling experiments the silicon heaters are supposed to mimic the mechanical and thermal characteristics of the actual MuPix sensors as close as possible. Therefore, the silicon is thinned to $50\,\mu m$ and cut into pieces with dimensions of $23 \times 19.8\,mm^2$. Traces of $1\,\mu m$ thick aluminium are sputtered on the surface to create two meanders. One meander shape is designed as a heating element with low resistivity and the other one can be used as a temperature sensitive element with a resistance of about $1000\,\Omega$ at $0\,°C$. The silicon heater is bonded to conductive traces on a flexprint and the resistance of the temperature sensitive element can be measured in a four-wire configuration.

Before building full modules with silicon heaters, one needs to study the characteristics of the chips themselves. In particular the temperature sensitive element needs to be calibrated and the mechanical deformations due to temperature variations need to be investigated. A picture of a silicon heater can be seen in figure 6.1 .
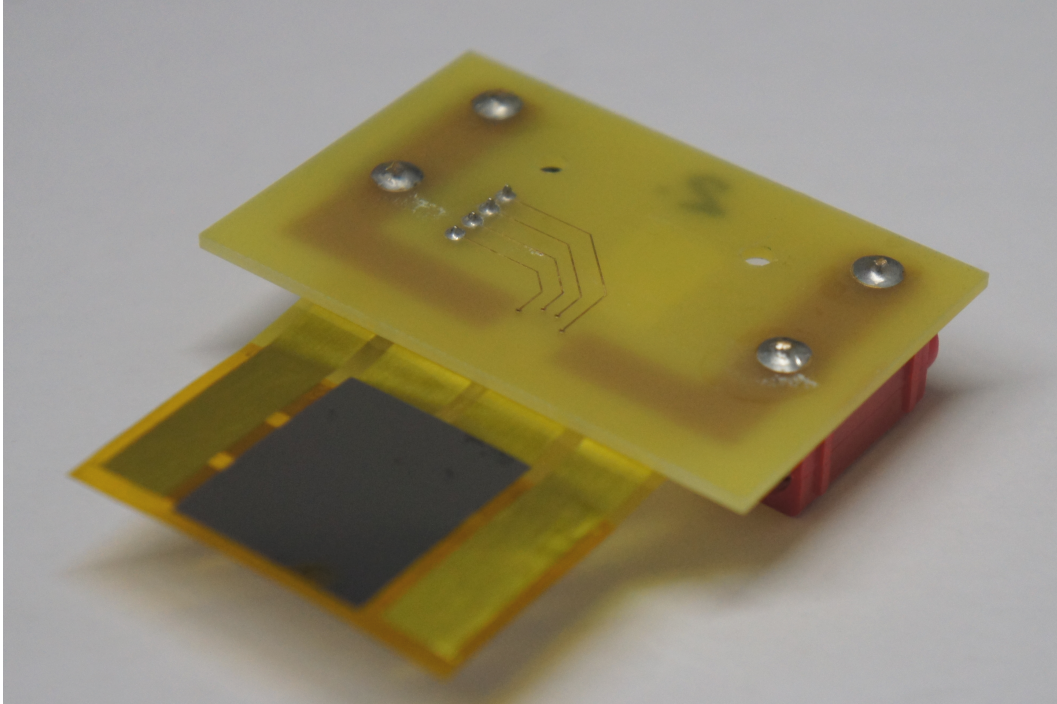
Figure 6.1: Silicon heater: Visible is the 50 µm thick silicon layer and the flexprint. It is possible to see four thin traces on the solid circuit board, which are used to connect in four-wire configuration.

6.1.1 Calibration of Temperature Sensitive Element

To calibrate the temperature sensitive element, which is nothing else but a temperature dependent resistor, one needs to measure the resistance of this element for different temperatures. This is done best by placing the Silicon Heater in a fluid bath, which is under constant circulation to create an evenly distributed temperature in the fluid. The thermal operation range of the MuPix sensor will be between $0\,°C$ and $70\,°C$. For this reason the calibration should at least cover this temperature regime. A buffer of $10\,°C$ is added to both extrema. Measuring below $0\,°C$ is possible due to a mixture of water and ethylene glycol in the fluid bath.

The temperature of the fluid and the resistance of the temperature sensitive element are measured with a MSCB SCS2000 slow control box [39]. At the current state, this device is equipped with slot cards capable of reading the temperature of a previously calibrated AD592 transistor [40] and the voltages from external sources. Measuring the resistance is performed in four-wire configuration (see figure 6.2), which eliminates additional resistances of the wires. For this technique one pair of wires is used to measure the voltage drop over the resistor R_S and the other pair is used to measure the current. Since the SCS2000 can currently only measure voltages, the current through the temperate sensitive element is obtained by measuring the voltage drop over a known resistor with low temperature dependency. The resistance can simply be calculated by Ohm's law $R = U/I$. Comparable resistance thermometer (RTDetector) based on Platinum usually work with a current of
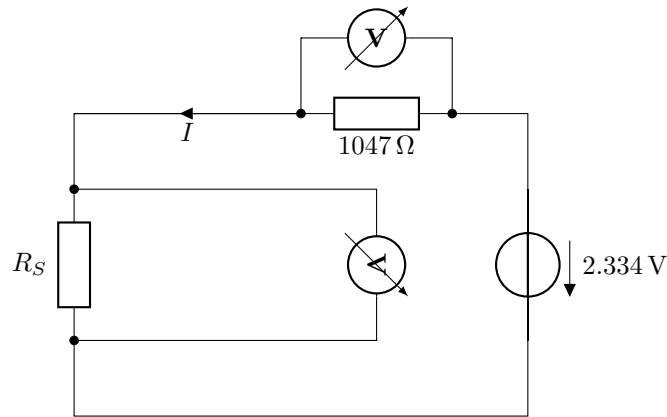
Figure 6.2: Schematic of the circuit used to measure the resistance of the sensor R_S. The silicon sensor R_S has a resistance of about $1300\,\Omega$ at $20\,°\text{C}$.

about $1\,\text{mA}$, which is also chosen for this experiment [41].

Prior to the actual calibration, it is tested whether measuring the resistance with an applied current of $1\,\text{mA}$ heats up the system itself. This problem is known as self heating. The silicon heater is placed freely in the room and to monitor the room temperature a AD592 transistor thermometer is placed in a distance of about $20\,\text{cm}$ to the sensor. This distance offers a reasonable compromise between not being effected by the possible heat source and being close enough to assume the same air temperature for the surrounding. This environment was chosen, because following tests of the deformation are performed in the lab without any special containers. The caparison of the resistance and temperature after one hour measurement is presented in figure 6.3. Taking into account that the AD592 transistor has an accuracy of $0.5\,°\text{C}$ at $25\,°\text{C}$ and that the resistance measurement has an error of about $2\,\Omega$, this plot shows that no significant self heating is measurable with this set-up. Furthermore, the future experiments do not require a precision below $1\,°\text{C}$, so self heating can be neglected. Especially, compared to the dissipated heat of about $1\,\text{W}$ by the heater element, the $1\,\text{mW}$ of the RTD are negligibly small.

For the calibration measurement the silicon heater is placed in a polyethylene (PE) bag and then dipped it into the fluid. The bag is not sealed at the top, so that the air in the bag is pressed out by the hydrostatic pressure and the silicon sensor has almost direct contact to the fluid.

The measurement begins at a temperature of $-10\,°\text{C}$ and the fluid is then slowly heated up. The temperature of the fluid and the resistance of the RTD are measured every second. At about $70\,°\text{C}$ the measurement is interrupted because of unrealistically values for the resistance. Investigating the problem's origin, revealed strong corrosions at two bonds, which eventually destroyed the connections. Pictures showing the corrosion and its effects will be discussed after finishing the calibration.

In figure 6.4 the resistance of the RTD is plotted in steps of $5\,°\text{C}$. The few unrealistic values are already neglected. Until $50\,°\text{C}$ the resistance follows a linear trend and above this temperature the resistance increases slower. These data points are also neglected because it is not certain whether these values are affected by the corrosion or actual aluminium
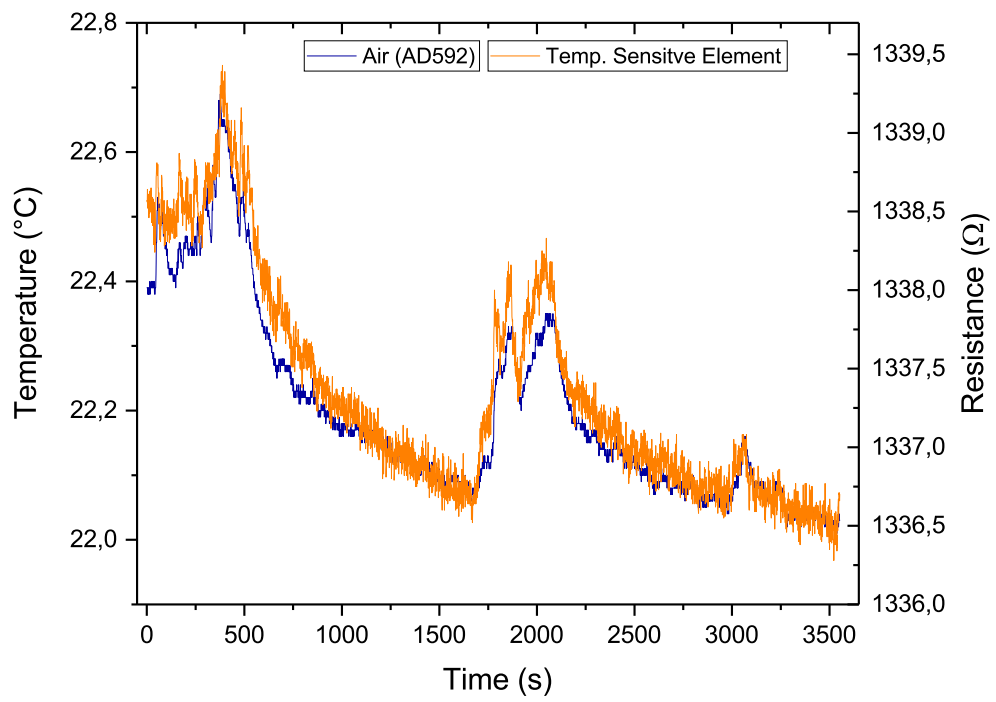
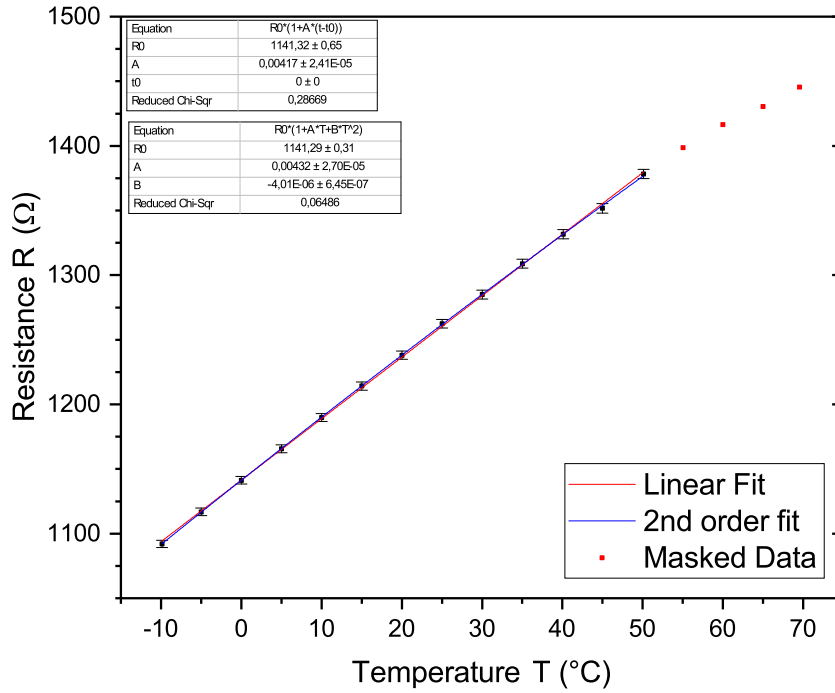Figure 6.3: Measurement of the self heating of the temperature sensitive element when applying $1\,\mathrm{mA}$ for $1\,\mathrm{h}$

Equation	R0*(1+A*(t-t0))
R0	1141,32 ± 0,65
A	0,00417 ± 2,41E-05
t0	0 ± 0
Reduced Chi-Sqr	0,28669

Equation	R0*(1+A*T+B*T^2)
R0	1141,29 ± 0,31
A	0,00432 ± 2,70E-05
B	-4,01E-06 ± 6,45E-07
Reduced Chi-Sqr	0,06486

Figure 6.4: Calibration curve obtained for the temperature sensitive element. Temperatures above $50\,°C$ are masked, because they might be affected the corrosion problem.

characteristics. A linear and a second order polynomial fit are applied for the data

$$R(T) = R_0(1 + A_\mathrm{l}T) \tag{6.1}$$

$$R(T) = R_0(1 + A_\mathrm{p}T + B_\mathrm{p}T^2). \tag{6.2}$$

Comparing both results shows that the difference of both fits is negligibly small for the considered temperature range. Therefore, future temperature measurements will be performed using the converted linear equation,

$$T(R) = \frac{(\frac{R}{R_0} - 1)}{\alpha} + T_0, \tag{6.3}$$

where α is the linear temperature coefficient of the resistivity and T_0 and R_0 can be chosen for different situations and RTDs. The error of this measurement is dominated by the accuracy of the resistor, which was added to measure the current. This causes the low χ^2_red indicating that the data is over fitted. The linear temperature coefficient α_0 for a reference temperature of $0\,°C$ is

$$\alpha_0 = (4.17 \pm 0.02) \cdot 10^{-3}/°C. \tag{6.4}$$

57

Sometimes it is more useful to have the linear temperature coefficient relative to $20\,^\circ\mathrm{C}$, which is slightly different:

$$\alpha_{20} = (3.85 \pm 0.02) \cdot 10^{-3}/^\circ\mathrm{C}. \tag{6.5}$$

It is possible to find reference values for the linear temperature coefficient being $3.9 \cdot 10^{-3}/^\circ\mathrm{C}$ [42] at $20\,^\circ\mathrm{C}$.

Corrosion of the Bonds

The corrosion affected two silicon heaters. In the first case the PE bag was leaking and fluid covered the sensor. Luckily, only one bond was destroyed so it is still possible to measure the resistance using a three-wire configuration. However, studying the corrosion for this sensor is not very informative due to the amount of fluid that entered the bag.

In the second case a new bag was used, which was tested multiple times for several hours in the fluid. Even though the bag was water proof, some condensation built up inside. After four hours of measurement time the two bonds connected to the positive voltage output of the SCS2000 were completely destroyed (see figure 6.5).

One could easily ignore this problem, stating that the MuPix chips will not have contact to water, but there are two things that should be considered. Compared to the planned one year run time of the Mu3e experiment, the chemical reaction time of the corrosion in the second case was short. One needs to evaluate the risk of leaks in the water cooling system or humidity in the helium atmosphere, which may create enough condensed water to start the corrosion process like in the discussed experiment. Since the bonds should be covered in a protective layer of glue, it might be an option to use a different glue and eliminate the problem for the future. The second reason why it is worth examining the corrosion further, is its blueish, greenish colour. This indicates the presence of a heavy metal ion like copper or nickel, which were officially not used in any production step [43].

Three-Wire Configuration

Forced by the corrosion it is necessary to test how well the resistance measurement performs using only three wires. This configuration is often used for industrial purposes, since it saves one cable. However, due to the missing cable the resistance of one cable is not eliminated and needs to be taken into account. A schematic of the three-wire configuration can be seen in figure 6.6 .

The following modification to the calculation of the resistance R_S can compensate for the additional lead resistor.

$$R_S = \frac{1}{I} \cdot (U_2 - (U_1 - U_2)) \tag{6.6}$$

In general subtracting two almost identical values gives an uncertainty, which could be compensated by adding an operational amplifier into the circuit. But before applying changes to the circuit, it is tested whether this step is necessary or not. Besides testing the accuracy of the three-wire configuration, this test is a good opportunity to check whether the
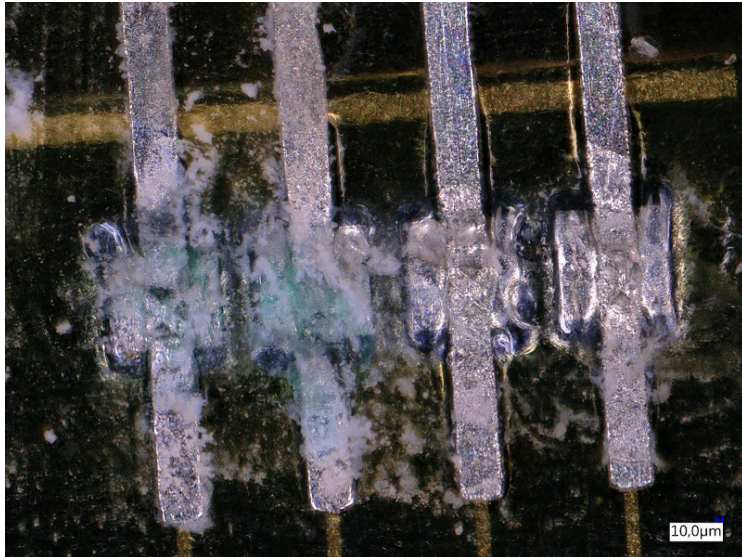
Figure 6.5: Visible corrosion at two bonds of the four-wire configuration. The two not corroded bonds on the right were connected to ground.
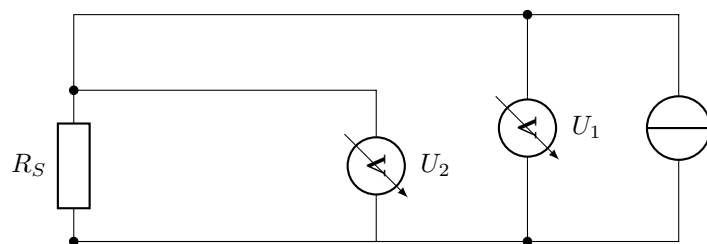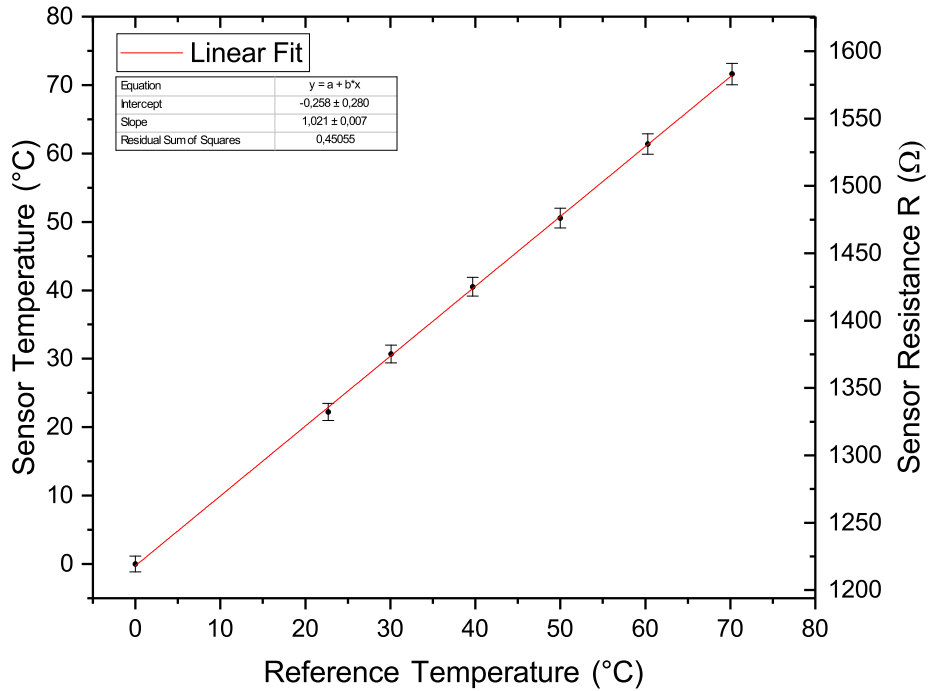

Figure 6.6: Schematic of three-wire configuration

Figure 6.7: Measurement of the accuracy when using a three-wire configuration

temperature calibration works for different chips too[1]. The temperature sensitive element is used to measure six temperatures starting with 20 °C going up to 70 °C. Figure 6.7 shows the resistance and the corresponding temperature of the temperature sensitive element as a function of the actual temperature. The error of the RTD is dominated by the error of the resistor that had to be added for the current measurement. This error is about is about 0.3 %, and thus the temperature errors are about 1.4 °C. Since all the other calculated temperatures are based on the priorly determined resistance for 0 °C, it is reasonable to add this value to the plot as well. If this value is not accurate, non of the other values should be. A linear fit is performed and shows that the results are about 2 % higher than the actual temperatures. This can be accounted as a systematic error, which is most likely due to the three-wire configuration.

This test proves that the accuracy of the measurement using only three wires instead of four is sufficient and the calibration for the aluminium resistance thermometer works.

6.1.2   Silicon Heater Deformation

As priorly discussed in chapter 5.2, mechanical stress due to thermal expansion is a problem that needs to be considered. Not only do the entire pixel layer modules change their length causing them to sag or tighten, the different materials also expand at different scales. This

---

[1]The calibration chip was destroyed (see section 6.1.1)

(a) Flat Sensor at initial temperature   (b) Deformation due to increased temperature
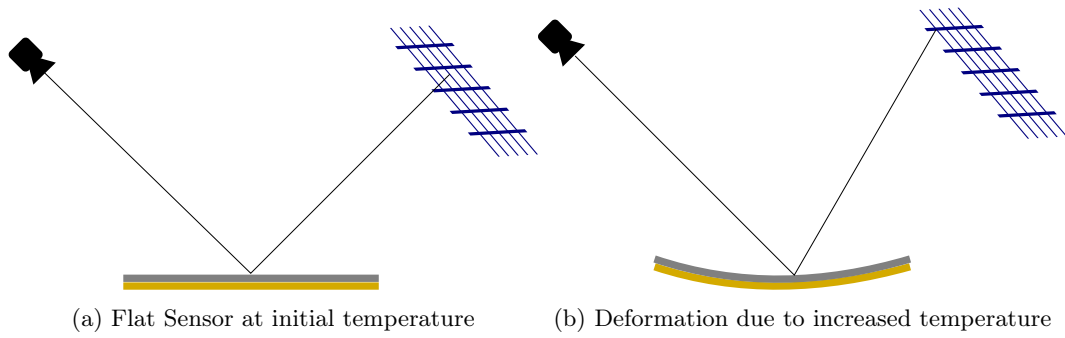
Figure 6.8: Schematic of the surface deformation experiment. The observed point on the graph paper changes for a flat surface (a) and a deformed, curved surface (b).

becomes a problem whenever two materials with different thermal expansion coefficients, like polyimide and silicon, are mechanically attached to each other. The linear expansion coefficient for these two material are:

$$\alpha_{\text{Kapton}} = 2.0 \cdot 10^{-5}/\text{K}$$
$$\alpha_{\text{Silicon}} = 2.6 \cdot 10^{-6}/\text{K}$$

In an environment with increasing temperature, polyimide expands stronger than silicon and due to the forced connection both materials will bent (see figure 6.8b). An approximation for $\Delta T = 50\,\text{K}$ can be calculated using some geometry and assuming that the contact plane of both materials expands at the same rate. The calculation can be found in appendix 7.2. Using an initial length 19.8 mm at 20 °C results in a displacement h of the central point by about 580 µm. This equals a change of 11.6 µm/°C.

To test how realistic this first approximation is, the deformation of a silicon heater is measured for different ΔT.

Since there is no three dimensional scanner with sufficient resolution on hand, an alternative experimental set-up is designed. The idea is to use the reflective silicon surface as a mirror (see figure 6.8). A camera is then used to take pictures of a graph paper, which is mirrored on the surface. To simplify the analysis, camera and graph paper are arranged with a 45° angle to the silicon surface. The temperature of the silicon heater can be increased by applying power to the included heater element. As an example for the deformation the pictures of the surface at about 30 °C and 50 °C are presented in figure 6.9 .

When assuming a point like camera lens it is possible to calculate some values for the surface deformation. The calculation is presented in appendix 7.2. The silicon sensor was assembled at room temperature, but due to necessary strong illumination the set-up's initial temperature is about 27 °C. Therefore, the deformation is given in reference to this temperature. The absolute deformation of the chip might be slightly higher but the deformation per Kelvin should be the same.

In figure 6.10 the height displacement h for the central point of the chip is plotted against the temperature of the silicon heater. For temperatures higher than 55 °C the entire set-up starts to deform and therefore these values are neglected. For the temperatures below, it is possible to see a linear dependency. A straight line is fitted to the data and the height

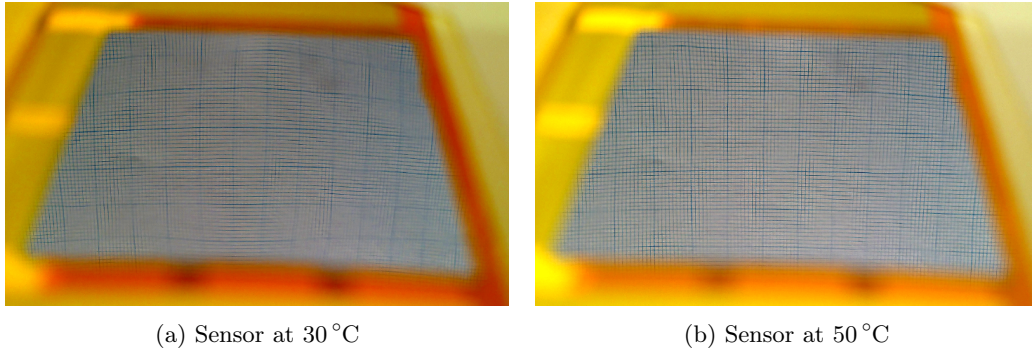(a) Sensor at 30 °C

(b) Sensor at 50 °C

Figure 6.9: Pictures of the reflected graph paper in the silicon surface for two different temperatures. The picture were modified to increase the visibility.

displacement per Kelvin is $(15.9 \pm 0.9)\,\mu\text{m/K}$, which is in a 30 % range to the first approximation.

Additionally it is possible to simulate the deformation of the silicon heater. The results of such simulations were provided by Thomas Mittelstaedt [44]. The height displacement per Kelvin in the simulations is about $11.3\,\mu\text{m/K}$. Figure 6.11 shows the result of a deformation simulation for 50 °C. The sensor is assumed to be flat at 20 °C. Unfortunately, the actual deformation is too small to show a direct comparison between the experiment and the simulation.

The simulation was performend for a sandwich of $50\,\mu\text{m}$ flexprint[2] and $50\,\mu\text{m}$ silicon, which equals the layering of the studied real silicon heater. One possible explanation for the 30 % difference between simulation and experiment is that the simulation software Catia Version 5-6 can not properly interpret the glue (Araldit 2011 2k glue). The glue points (circles in figure 6.11) had to be mimicked with welding points with redefined characteristics. These points were destroyed in the simulation, but apart from the corrosion the real silicon heater is still in perfect shape.

In the end, both method show similar characteristics for the chip and the deformation needs to be studied further, because it obviously affects the track reconstruction. However, as long as the deformation is static, it should be possible to include the deformation to the track reconstruction software. In order to have a static problem, the temperature variations over time need to as low as possible.

6.2 Tape Heater

Tape heaters are a laminate of $25\,\mu\text{m}$ thick polyimide and $25\,\mu\text{m}$ aluminium. Like on flexprints, traces are lasered into the aluminium creating to meanders. One functioning as resistance thermometer and the other one as heater element. An exemplary tape heater half is shown in figure 6.12a. Their width is about 23 mm, resulting in an overlap to the adjacent tape.

In this section some characteristics of Layer 4 modules build with these tape heater will be

---

[2]The flexprints expansion coefficient was defined as $\alpha_{\text{flex}} = 2.15 \cdot 10^{-5}/\text{K}$
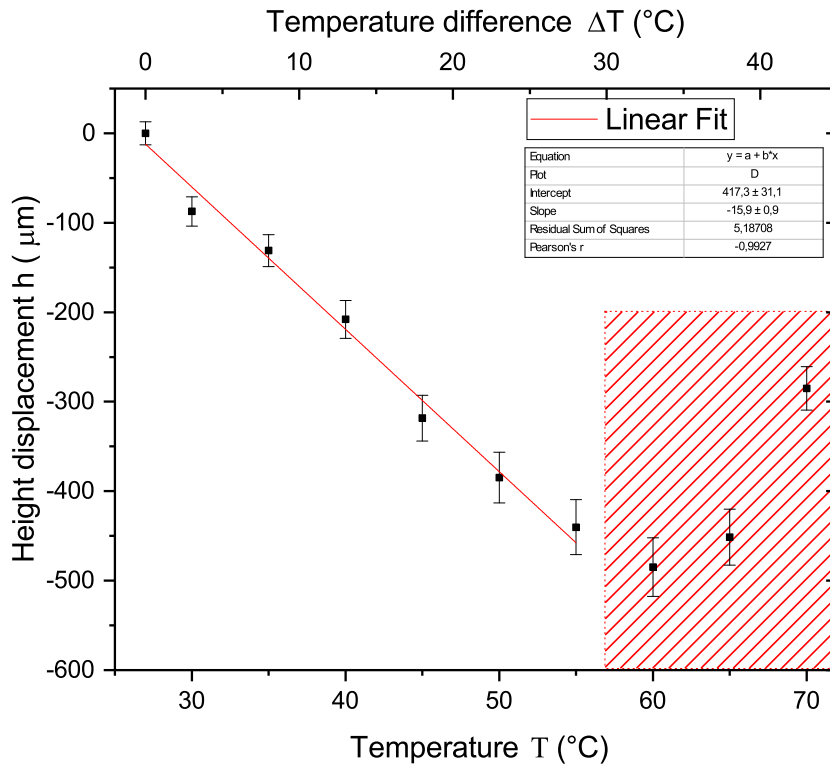
The chart shows:
- Top axis: Temperature difference ΔT (°C) with values 0, 10, 20, 30, 40
- Left axis: Height displacement h (μm) with values 0, -100, -200, -300, -400, -500, -600
- Bottom axis: Temperature T (°C) with values 30, 40, 50, 60, 70
- Linear Fit legend

Equation	y = a + b*x
Plot	D
Intercept	417,3 ± 31,1
Slope	-15,9 ± 0,9
Residual Sum of Squares	5,18708
Pearson's r	-0,9927

Figure 6.10: Height displacement of the central point on the Silicon Heater. The red coloured area is neglected due to visible deformations for the entire set-up.

Height displacent

mm
0,339
0,305
0,271
0,237
0,204
0,17
0,136
0,102
0,0678
0,0339
0

At border
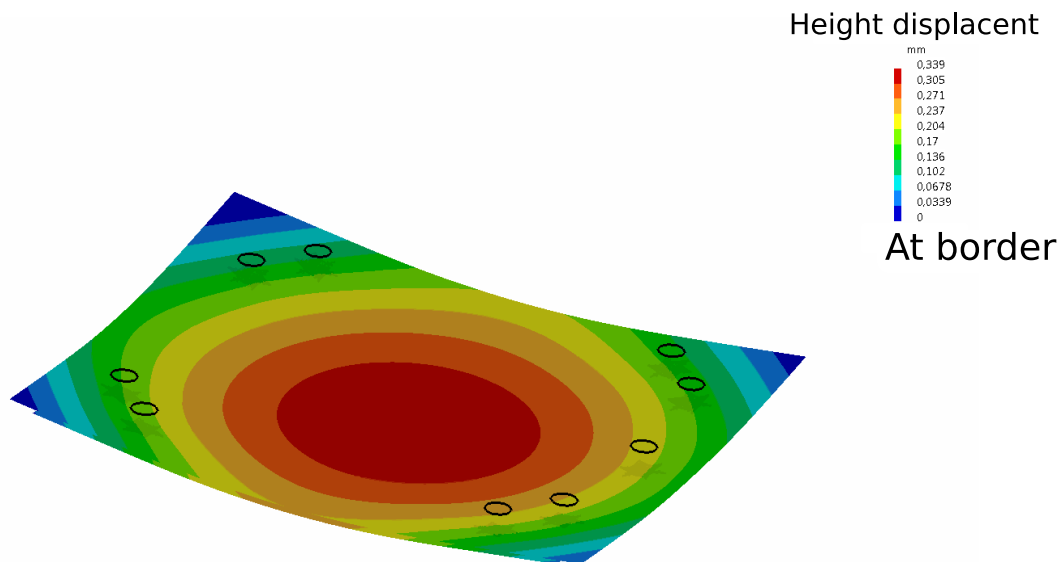
Figure 6.11: Simulation of the silicon heater deformation for 50 °C relative to the flat surface at 20 °C

(a) Tape heater half
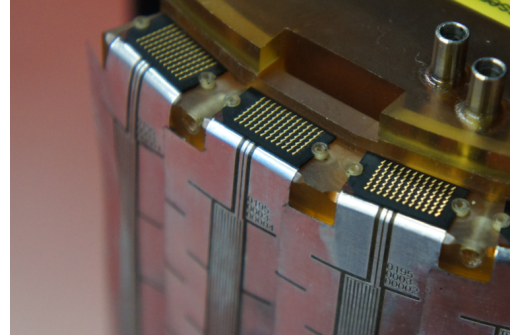
(b) Tape heater and connecting interposer

Figure 6.12: Pictures of (a) a tape heater half and (b) then partially assembled module with four tape heaters and interposer on top. The central, fine meander is used for the temperature measurements and the surrounding meander is used to heat the tape.

presented. The tested module does not include V-folds, so the mechanical stability is different and cooling is only possible by a global flow. In order to create this flow, the module is placed in an acrylic tube with 22 cm diameter and computer fans on both ends.

The temperate sensitive element on the tape heater is designed to have about 14 Ω at 22 °C. To measure temperature dependent changes of the resistance it is necessary to use a high accuracy multimeter [45]. It is intended to measure the resistance in four-wire configuration without creating a permanent connection to the tape heater. This way it is possible to additionally test the interposer, which are used to create a connection between the aluminium traces and the read out system. Aluminium has the unfortunate characteristic to be covered in a thin layer of aluminium oxide, which is an electric insulator. For this reason each interposer consists of copper needles (see figure 6.12b) that poke through the corrosion layer into the conducting aluminium if the necessary pressure is applied. Figure 6.12b shows the positioning of the interposer on top of the tape heater, a second polyimide aluminium laminate is placed on top, which is connected to the read out.

Once again self heating of the RTDs needs to be considered. Since all the following measurements are performed in the acrylic tube, also the self heating is tested in this environment. The multimeter constantly applies 1 mA and measures the voltage changes to determine the resistance. The temperatures inside and outside the tube are monitored with AD592 transistors and the data is acquired every second over a time period of one hour. The results of this measurement is presented in figure 6.13. The accuracy of the multimeter in this resistance range is below 1 mΩ, so this error is negligibly small compared the resistance fluctuations due to small temperature variations. The accuracy of the AD592 transistors is about 0.5 °C and since future measurements with about 1 °C accuracy are more than sufficient, the self heating is not considerable and does need to be quantified more precisely. It is also possible to see, that the temperature changes inside the tube are less strong than on the outside,
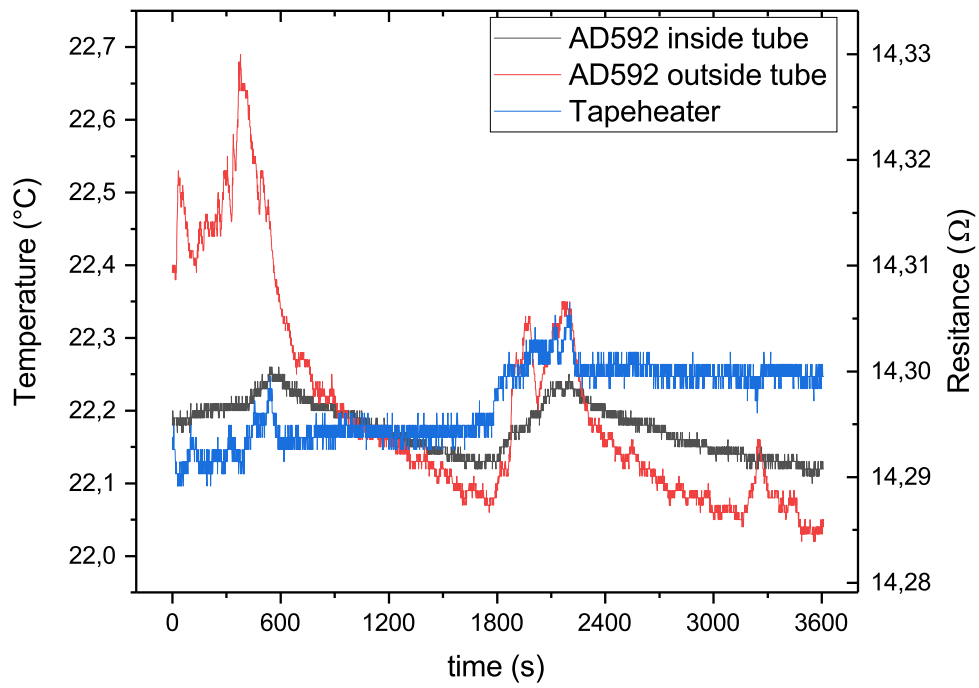
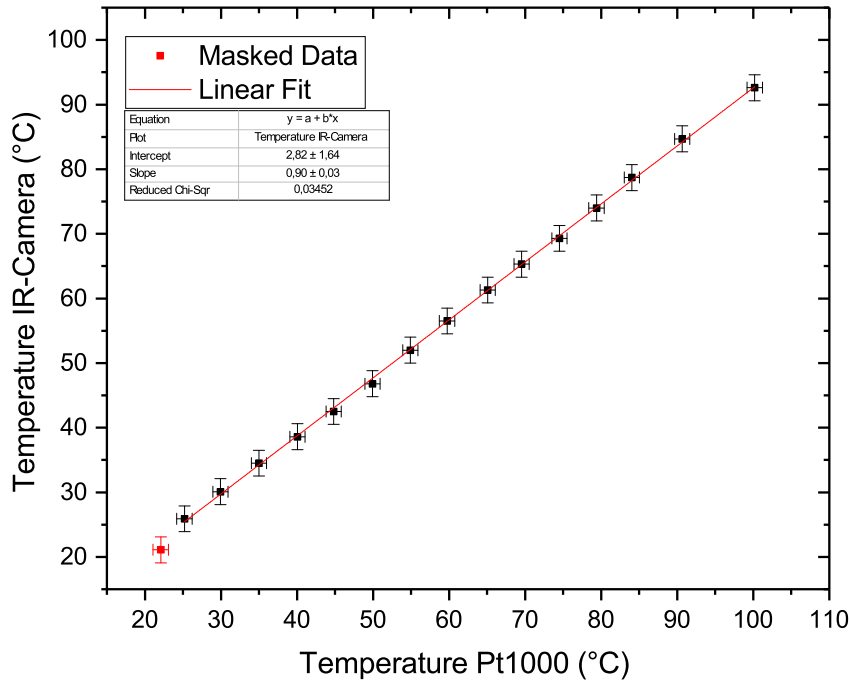Figure 6.13: Self heating measurement of tape heater in the acrylic tube for one hour

Figure 6.14: Calibration of the IR-camera in combination with the radiator paint. The first data point is neglected, since it was not possible to distinguish between the resistor and the ground.

which can be explained by the spatial separation due to the acrylic tube.

Emissivity Measurement of the Radiator Paint

The next important step is to verify if the tape heater heats up evenly. Obtaining a temperature profile of the entire tape is done best by using an infra-red (IR) camera. The advantage is, that one obtains a full profile in contrast to the located values one gets when gluing additional thermometers on top of the aluminium. The main problem, however, is the high reflectivity of aluminium for these wavelengths, making the results of the camera unreliable. Measuring the polyimide sides of the tapes instead is not an option neither, because they will not be visible in the set-up. One working solution is to apply a thin layer of radiator paint, which has a high emissivity. In order to get reliable data the emissivity ϵ of the paint needs to be determined.

This step is necessary, because the IR-camera does not actually measure temperatures but the radiative flux coming from the observed objects. To calculate the temperature one uses the Stefan–Boltzmann law

$$P/A = \epsilon\sigma T^4 \tag{6.7}$$
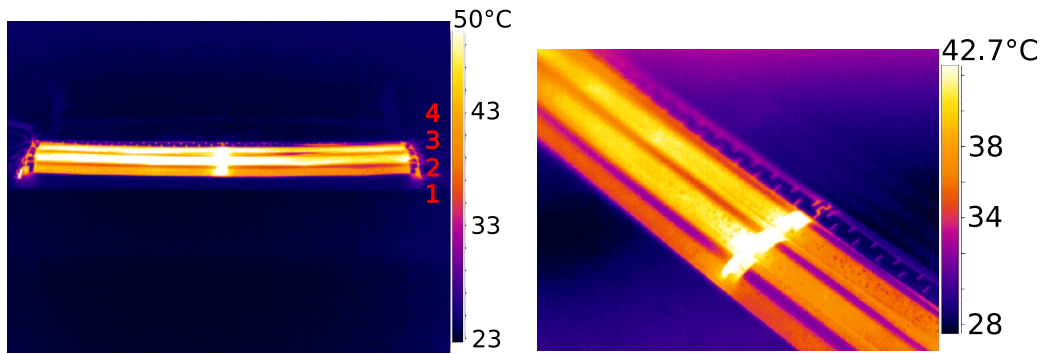
(a) Full tape heater module heated with 20 W (b) Close-up of the central area heated with 10 W

Figure 6.15: IR-camera picture of the module. The tape heaters are numbered from the front to the back.

with the Stefan-Boltzmann constant σ. Varying emissivities of different materials usually cause high inaccuracies of IR cameras. To measure the emissivity, a Pt1000 (Class B) resistance thermometer is glued[3] on top of a $1\,\Omega$ $5\,W$ ceramic power resistor, which is then sprayed with radiator paint. This set-up is heated up to different temperatures and the surface temperature is measured with the Pt1000 and the IR camera. The error for the camera is given as $2\,°C$ [4]. The calibration of Pt1000 resistors is well known; hence it is possible to calculate the temperature. The value for the resistance fluctuates about $10\,\Omega$ and the error of the RTD measurement is estimated to be $0.5\,°C$. The obtained temperatures are plotted in figure 6.14 and a linear fit function is applied. The first data point is neglected since the resistor can not be distinguished properly from the underground. The slope of this fit function can be interpreted as the emissivity ϵ of the radiator paint, which yields 0.90 ± 0.02. Possible errors due to the thickness of the paint layer are difficult to predict, but should already be accounted for in the high error of the IR-camera.

Three of the four tape heaters of the Layer 4 module are painted and one is kept original as a reference for the temperature and the mechanical stability, which might be changed due the additional layer of paint.

6.2.1 Studies with the Current Tape Heater Design

In total there are eight heater elements, because each tape heater has individual electric circuit for both halves. For each end, these elements are connected in a row and $10\,W$ are applied, complying with a total power supply of $20\,W$. Pictures taken with the IR camera are presented in figure 6.15. Since acrylic glass does not transmit IR wavelengths, the pictures had to be taken through a opened lid in the tube. It is possible to see higher temperatures for the region at half the length. This indicates a higher resistance for this region, which needs to be corrected for future measurements. One can also see that the area of the temperature sensitive elements does not radiate as strong as the heater element, so

---

[3]A special heat conductive glue was used.
[4]Trotec LV/V Serie

67

Tape	RTD left	RTD right	IR-camera left	IR-camera right
1	39.2 ± 0.5	42.0 ± 0.5	41 ± 2	41 ± 2
2	47.3 ± 0.5	44.6 ± 0.5	46 ± 2	44 ± 2

Table 6.1: Comparison between the temperatures in °C at $P = 20\,\mathrm{W}$ determined with the RTD and the IR camera

it seems reasonable to neglect its area when calculating the heat load per surface area. In figure 6.15b one can see the difference between the painted tapes and the aluminium surface. The resistances of the RTD can be transformed to temperatures using the priorly determined thermal resistance coefficient for aluminium. The camera software can be used to measure the temperature for the visible area of the RTD, which has a lower temperature than the rest of the tape heater. These values and the corresponding RTD results are listed are listed in table 6.1. The temperatures measured with the IR-camera are already corrected for the given emissivity of the radiator colour. The obtained values for both methods are consistent. Unfortunately, this is an issue, because the temperatures are measured for the coolest area on the tape heater and the heater elements surrounding the RTD can be up to $10\,$°C hotter. This means measuring the temperature using the RTDs seems to give a lower limit for the temperature, which is not a very useful information for cooling experiment. A possible explanation could be the low thermal conductivity of polyimide, which is the only material in contact with both meanders. Due to this observation it will be necessary to further characterize the temperature distribution on the tape heater to either find a correction or estimation for the error. This task will not be context of this thesis, but it should be considered that absolute temperature values of the RTDs need to be handled with caution. For the next step, a constant air flow of about $2\,\mathrm{m/s}$ is created in the tube, which cools down the still heated module. A comparison between a picture of the temperature profile and a corresponding simulation with a total power supply of $20\,\mathrm{W}$ applied to the aluminium, is shown in figure 6.16. Due to the unevenly heated surface of the tape heaters, the temperature profile looks different and in particular the central region is too hot. Comparing the temperatures of the RTDs to the IR camera values shows matching values once again, but one RTD shows a temperature which is about $6\,$°C higher than for the IR-camera. A higher temperature for the RTDs is unexpected and a first indicator for another problem, which will be discussed later.

Comparing the absolute temperatures of simulations and the measurements with RTDs is almost meaningless for two reason. The first one involving the results of the RTDs was already discussed above. The second problem is that the set-up now contains three painted tape heaters. Aluminium usually has a emissivity of about $4\,\%$, but by adding the radiator paint we increased the heat dissipation via radiation by a factor 22. For a temperature of $40\,$°C one tape heater now dissipates about $3\,\mathrm{W}$ instead of about $140\,\mathrm{mW}$. Including radiative heat transfer into the simulations is theoretically possible, but there are missing parameters like the heat conductivity or the thickness of the paint layer. Running the simulation with convective heat transport only and estimating how much heat was carried away by radiation is possible, but not very meaningful if the absolute temperatures of the RTDs
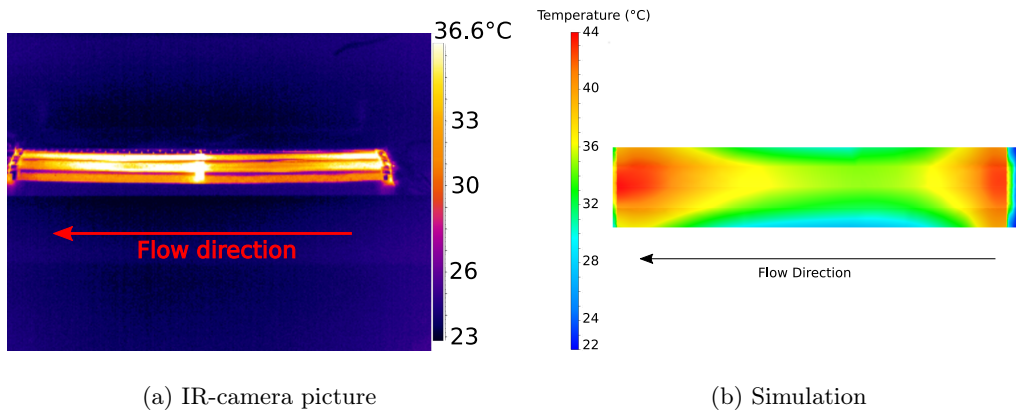
(a) IR-camera picture   (b) Simulation

Figure 6.16: Comparison between the IR-camera picture and the simulation for heated aluminium tape heater. An airflow of $2\,\text{m/s}$ and $22\,\degree\text{C}$ cools the heated module with a total heat dissipation of $20\,\text{W}$.

are not accurate.

At this point neither measuring the absolute temperatures nor characterizing the temperature distribution are representative for future experiments, so the only test left is to verify whether the elements heat up proportional to the power supply. Therefore, the power is increased in steps of $20\,\text{W}$ up to $120\,\text{W}$, while cooling with a constant flow of air with a velocity of $2\,\text{m/s}$. The heat load per surface area is calculated for an area of $19 \times 360\,\text{mm}^2$ per tape heater. The area of the temperature sensitive element is neglected for this calculation. Due to the early state of the set-up, the temperatures of the eight tape heater halves need to be measured manually and individually. The error of the RTDs is estimated to be about $0.5\,\degree\text{C}$, which consists mostly of fluctuations during the measurements. It should be noted, that the measurement reveal a currently unpredictable error, which will be explained below. Figure 6.17 shows the temperature difference ΔT plotted as a function of the power supply. The reference temperature is $22\,\degree\text{C}$, which corresponds to the initial temperature of the air flow when entering the tube. The data is split into two sub-plots, in order to improve the visibility. The numbering of the tape heaters is indicated in figure 6.15a . One can see that most of the data can be described fairly by linear fits, but the high χ^2_{red} indicates that the errors are poorly estimated. It is also possible to see that the temperatures increase slightly in flow direction.

However, the more interesting data points are the ones not fitting into the expectations. For example, according to the data one tape heater had a temperature of about $30\,\degree\text{C}$ before heating the system even started and one data point for $120\,\text{W}$ has about $140\,\degree\text{C}$, which exceed the figure scale. Furthermore, non of the RTDs returned to its initial resistance once the heating test was finished. Some kept resistances above $20\,\Omega$, even though they are designed to have about $14\,\Omega$ at room temperature. The module was taken apart, but there were no visible damages to the set-up and after putting it back together the problem of unexpectedly high resistances was temporarily solved. This indicates that the problem is connected to the interposer and the aluminium oxide layer. First can affect the resistance if the pressure on the interposer changes, due to deformation of the carbon fibre plate applying

the pressure or an expansion of the metal screws fixating this plate. Second could effect the resistance if the oxide layer thickness increases for higher temperatures. A simple option to test one of these possibilities, is to use two carbon fibre plates instead of one. The additional strengthening should minimize a deformation of the plate and changes to the pressure should be smaller. However, this method could not solve the problem, so it will be a necessary step for the future to systematically search the cause of these resistance variations. After all it is interesting that the resistance still increases more or less linearly with the temperature and then returns to higher values when cooling down, but understanding this dependency requires solving the problem.
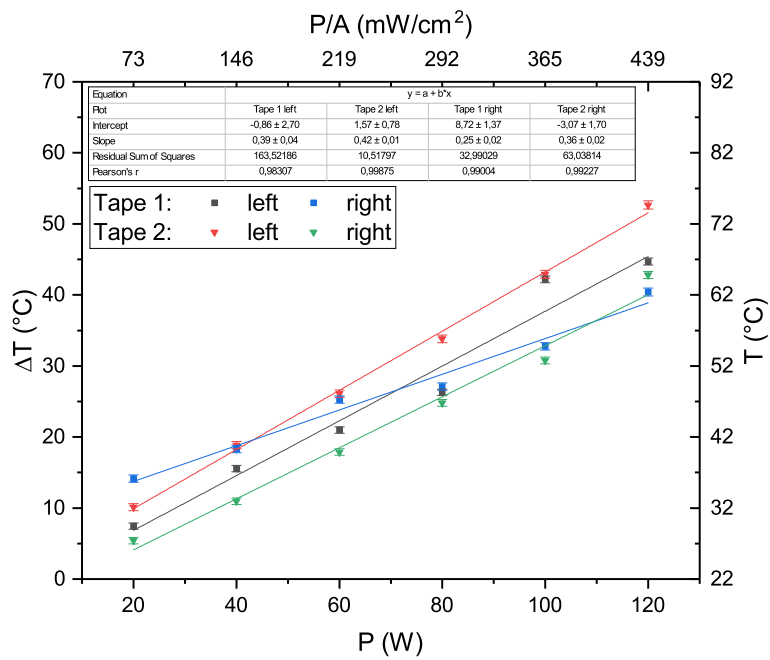
(a) Tape heaters in the front
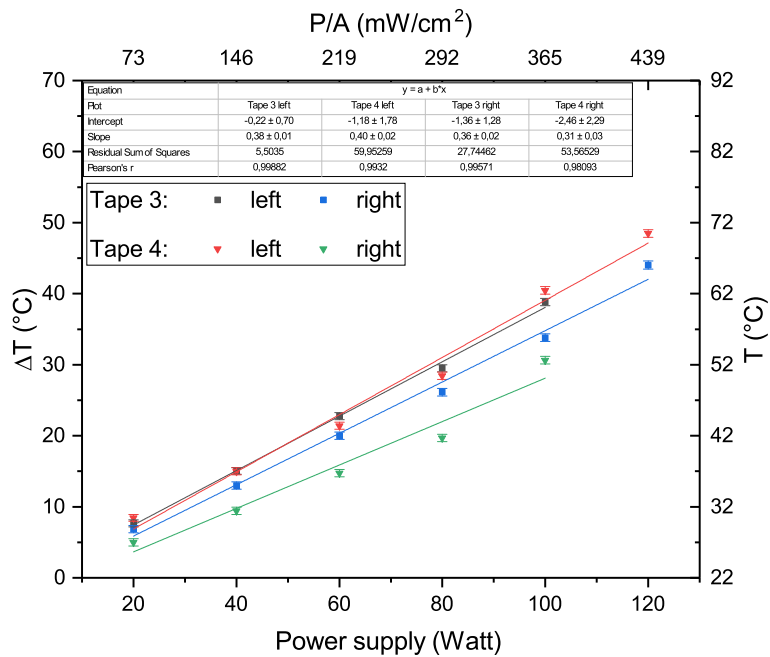
(b) Tape heaters in the back

Figure 6.17: Temperatures of the RTDs as a function of the power consumption. The shown error consists of the calibration error and the error of the resistance measurement. The unpredictable error due to the interposer is neglected.

Chapter 7

Summary & Outlook

7.1 Summary

The Mu3e experiment requires a cooling system that increases the effects of multiple Coulomb scattering as little as possible while still being capable to remove a heat load of about $5\,\mathrm{kW}$ for the entire detector. Using gaseous helium as coolant offers the best compromise between cooling potential and radiation length. Since this system will be the first of its kind, it is essential to test its efficiency and feasibility. Following a first successful proof a concept, it is time to study a design that could be implemented into a running detector. This includes having a concept how to fit the helium ducts and inlets in between the electronic wiring and detector components. The cooling system is based on six individual flow circuits guaranteeing sufficient helium flow between the four layers of the tracking detector. The tracking detector consists of HV-MAPS with a probable heat load per surface area of about $250\,\mathrm{mW/cm^2}$. As an insurance the cooling system should be capable to keep the temperature below $70\,^\circ\mathrm{C}$ even when the heat is increased to pessimistic $400\,\mathrm{mW/cm^2}$. Tests will be performed in two stages; theoretical analysis performed with computational fluid dynamics simulations and an experimental phase with a full thermal-mechanical mock-up of the Mu3e detector.

The first step was to study the different helium distribution systems providing the helium flow into the detector region. This is important because the flow profile directly influences the temperature distribution in the detector. If the flow is not evenly distributed this can cause a strong temperature gradient, which induces mechanical stress due to thermal expansion. The informations gained by CFD simulations could be used to propose changes to the design, which will lead to a more even flow pattern. In particular, the module endpieces with included helium distribution system could be optimized.

Simulations with convective heat transfer show that the maximum temperatures of the detector could reach $T_{\mathrm{max},250} = 49\,^\circ\mathrm{C}$ for $250\,\mathrm{mW/cm^2}$ and $T_{\mathrm{max},400} = 77\,^\circ\mathrm{C}$ for $400\,\mathrm{mW/cm^2}$. This shows that the temperatures in the detector are proportional to the heat load, so once the final silicon chips is characterized it is possible to calculate the maximal temperature for the given heat load. The maximal temperatures will be reached for the inner pixel tracker double layer, which is only cooled with a single helium flow. Since the final temperatures

need to be below 70 °C, the inner detector in its current state can not be cooled sufficiently to remove a pessimistic heat load of $P/A = 400 \, \mathrm{mW/cm^2}$. However, it could be shown that adding another flow of coolant or optimizing the distribution for the single flow can lower the temperatures. Choosing at least one of these option will be necessary to keep the temperatures of the detector below 70 °C, which is the upper limit of the operating range of the tracking detector. The cooling system for the outer double layer seems already sufficient, since the highest temperatures for this part are $T_{\mathrm{max},250} = 25$ °C for $250 \, \mathrm{mW/cm^2}$ and $T_{\mathrm{max},400} = 40$ °C for $400 \, \mathrm{mW/cm^2}$. But in the most pessimistic case these values could increase by 50 %. The reason for this high inaccuracy is that the simulated model requires a high element number for the simulations and further improving the mesh of these simulations requires additional computational power. Results of the outer double layer can also be used for the four recurl stations, which have a similar cooling design.

The question whether it will be necessary to organize additional computational power, will be answered in experimental studies with the thermal-mechanical mock-up. This mock-up will consist of silicon heaters with comparable characteristics to the future HV-MAPS and a polyimide-aluminium laminate which is mainly used to lower the costs for the mock-up. Both parts have been tested in the context of this thesis. To obtain the temperature in the future experiment, both devices are equipped with aluminium resistance thermometers. A calibration curve was measured and the linear thermal resistance coefficient relative to 20 °C is $\alpha_{20} = (3.85 \pm 0.03) \cdot 10^{-3}/\mathrm{K}$. In order to use less wires it is possible to use a three-wire configuration instead of a four-wire configuration. The systematic error between both methods was measured to be about 2 %. The mechanical structure of the Mu3e experiment contains materials with different thermal expansion rates. The effects of uneven expansion was tested for a silicon heater prototype and the central point of the rectangular sensor changes its height by $(15.9 \pm 0.9) \, \mathrm{\mu m/K}$. As long as this deformation is static it will be possible to compensate for this deformation by performing calibration runs and adding the information into the reconstruction software.

The majority of the heating elements in the thermal-mechanical mock-up will consist of tape heaters. These aluminium-polyimide laminates have been tested for their heat distribution and accuracy of the integrated thermometer. The temperature distribution on the aluminium surface could be studied with an IR-camera after applying a layer of high emissivity paint. This revealed an uneven distribution , which needs to be corrected for the final test runs. The resistance thermometers on the tape heater could be tested, but due to an issues with the electronic connections in form of interposer the absolute values are not reliable yet.

In the context of this thesis multiple aspects of the future cooling system of the Mu3e experiment have been tested. Simulations show that the current design with a few adaptations will be capable of keeping the temperature in a reasonable range. More importantly it is possible implemented this system into a detector and, therefore, this is a major step forward.

7.2 Outlook

Many aspects of this thesis were performed with regard to the thermal-mechanical mock-up of the Mu3e detector, which will be used to further study the cooling system. This full scale model will consist of the two discussed heater module types, which will be assembled around two beam pipe dummies. The mechanical construction holding these beam pipe dummys and thus the entire test detector was already designed and manufactured in the early stages of this thesis. But until first heatable modules arrive, there are still a lot of problems that need to be solved. For example it is necessary to upgrade the resistance measurement set-up in order to measure at least 140 individual temperature sensitive elements. This number is valid if the mock-up only consists of tape heaters. In contrast, one Layer 4 module with silicon heaters will already consist of 72 resistance thermometer. Part of this read out system will be the use of interposer. Unfortunately, this thesis revealed unsolved issues with this type of connector and before building the thermal-mechanical mock-up this needs to be further examined. Once the mock-up is operational the cooling system will be tested with all the presented flow circuits including the flow through the V-folds. These experiments will eventually be performed in a helium environment to test the actual cooling capability of the system.

Additionally, it needs to be tested how silicon heater modules with multiple chips deform for varying temperatures and if vibrations induced by the flow can be tolerated. Another important problem for the future will be the installation of a pump system that can keep the pressure gradients inside the detector low. Since the accuracy needs to be in the order of millibar, this is an involved problem.

Furthermore, it is possible to keep working with CFD simulations. Especially, some of the helium flows through the detector could be further improved and since optimizing the flow will improve the cooling system, this is an advisable step.

For the Mu3e experiment, the cooling system might only be a necessary sub system, but it offers a great variety of experimental work and requires to solve many individual problems. Therefore, testing the cooling system will be an exciting task for the future.

Appendix

A.1 Geometrical Estimation of the Deformation of a Polyimide-Silicon Layer

The length L of a material which expands due to a temperature difference is given by:

$$L = L_0 + \alpha L_0 (T - T_0), \tag{A.1}$$

where α is the linear expansion coefficient and L_0 is the length of the material at the initial temperature T_0.

For this calculation we assume that polyimide foil and silicon expand equally in the contact plane. Therefore the deformed sandwich can be handled as an annulus section (see figure A.1). The height displacement h can be calculated as the height of an circular segment, which is given by:

$$h = R(1 - \cos\frac{\alpha}{2}), \tag{A.2}$$

where R is the radius and α the central angle. These two values can be obtained by the equation system:

$$L_{\text{Silicon}} = \alpha \cdot R$$
$$L_{\text{polyimide}} = \alpha \cdot (R + d) \tag{A.3}$$

The two lengths L are the values after the deformation and d refers to the thickness of the polyimide-silicon sandwich. The equation for the height displacement finally yields

$$h(T) = \frac{d}{\frac{L_K(T)}{L_S(T)} - 1}(1 - \cos\frac{L_K(T) - L_S(T)}{2d}) \tag{A.4}$$

Due to the Cosinus term this solution is not very handy. Since were are mostly interested in the height displacement per Kelvin, the derivative of this equation is determined. Below $100\,°C$ the slope is more or less constant and the value is $11.6\,\mu m/K$.
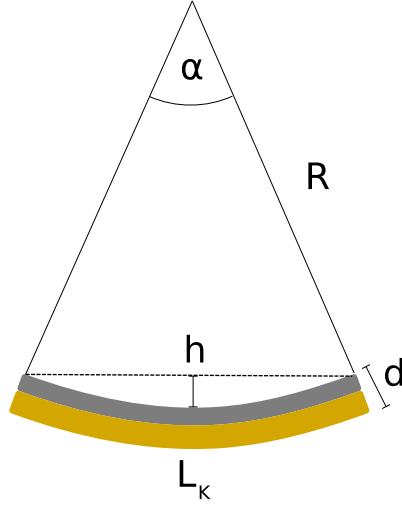
Figure A.1: Geometrical determination of height displacement for a first approximation.

A.2 Evaluation of the Displacement Visible in the Taken Pictures

To simplify the calculations it is assumed that the camera has a point like lens. This assumption seems reasonable for most phone cameras.

At first the equations are determined for a one dimensional flat mirror (see figure A.2a). In the experimental set-up both camera and graph paper were arranged at 45° with respect to the mirror surface. The coordinate systems on the pixel screen and on the mirror are chosen as indicated in figure A.2a. Pixel position on the picture can be transformed into positions on the mirror surface using some geometry, in particular the Sinus theorem:

$$\frac{g}{\sin(\alpha)} = \frac{c}{\sin(\frac{\pi}{2} - \gamma)} \qquad \frac{d}{\sin(\alpha)} = \frac{f}{\sin(\frac{\pi}{2} - \alpha)} \qquad (A.5)$$

With $c = \sqrt{(\sin(\gamma)c_0)^2 + (\cos(\gamma)c_0 + g)^2}$, $|g| < c_0$ and $0 \leq \gamma \leq \pi/2$ the coordinate transformations are

$$d = -f \cdot \frac{g\sin(\gamma)}{g\cos(\gamma) + c_0}$$
$$g = -\frac{dc_0}{d\cos(\gamma) + f\sin(\gamma)} \qquad (A.6)$$

Even though the focal length f and the pixel sizes for the used camera are known, the transformation from pixel to mirror coordinate does not work properly. The main reason is that the lens system is unfortunately a bit more complicated than a point like lens. For this reason the focal length, which is the only camera dependent factor, needs to be eliminated. This is possible by using the following relation

$$\frac{p}{p_0} = \frac{d}{d_0}, \qquad (A.7)$$

76
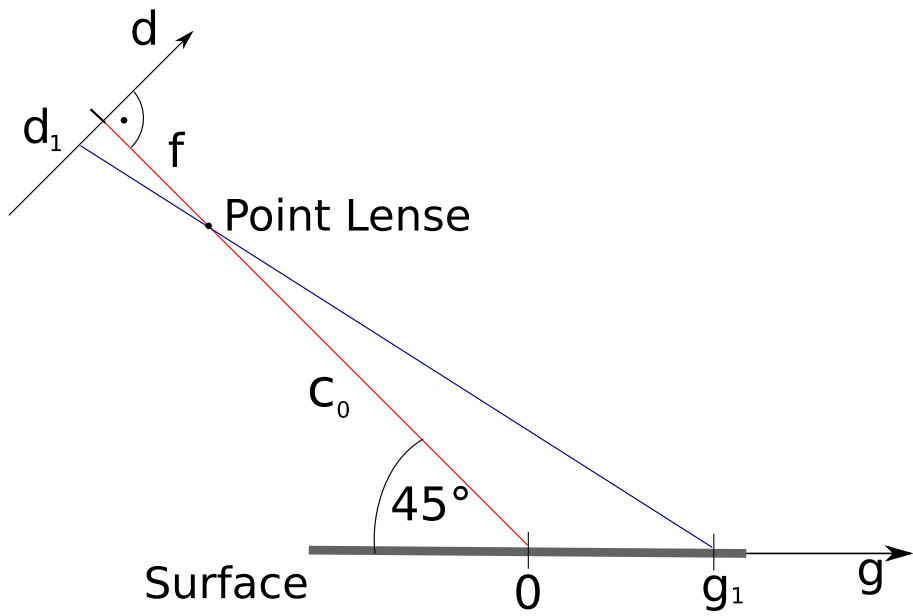
(a) Coordinate transformation
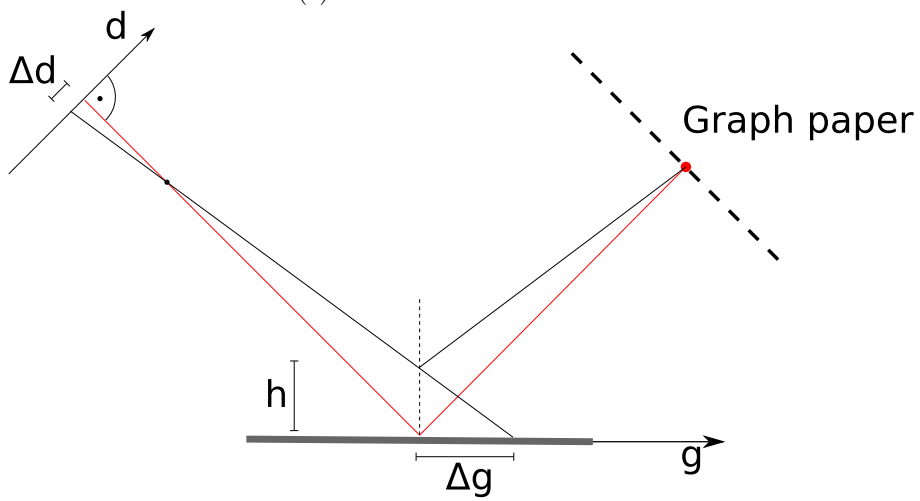
(b) Height displacement h

Figure A.2: Schematic of (a) the transformation between pixel position and position on the reflecting surface and (b) the determination of the height displacement when seeing the same point of the graph paper at different pixel
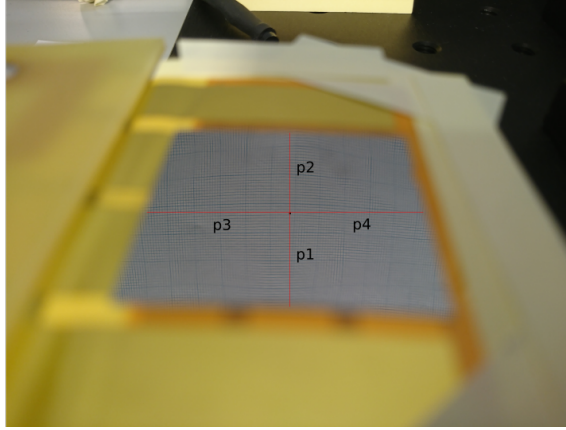
Figure A.3: Indicated central point and pixel distances on the silicon heater

where p denotes the pixel position on the pictures. The two missing quantities need to be defined by known lengths on the chip and on the picture. When assuming the camera is perfectly set up and the central point of the sensor corresponds to the central point on the picture, these values could be chosen as the length of the chip in pixel and $d_0 = d(-9.9) + |d(9.9)|$. However, arranging camera and chip so precisely with the rather simple set-up used, is very complicated. Therefore the position on the chip corresponding to the central pixel needs to be determined.

For this reason the pixel distances from the central pixel to the end of the chip are obtained (see figure A.3). Their ratio is $p_1/p_2 = 0.63 \pm 0.05$ and with the following equation it is possible to calculate the origin on the sensor:

$$\frac{p_1}{p_2} = \frac{d(19.8 - x)}{d(x)} \tag{A.8}$$

Solving this equation for x yields that the central pixel correspond to the point which is (8.7 ± 0.2) mm off the close edge. The same method can be used to determine whether the pixel center equals the sensor center in horizontal direction. The ratio between both pixel distances is

$$\frac{p_3}{p_4} = \frac{(1330 \pm 30)\,\mathrm{px}}{(1420 \pm 30)\,\mathrm{px}} = 0.94 \pm 0.03. \tag{A.9}$$

This equals a displacement of (0.36 ± 0.18) mm, so it is reasonable to assume the central pixel is pointed at the center of the chip in horizontal direction.

These transformations provided it is now possible to determine the height displacement of single points on the chip. One restriction is that the following calculations only work for points on the vertical line through the picture center. The obvious reason is that we only defined our transformation functions in this one dimension. In theory, it is possible to extend the transformation functions for the horizontal dimension, but the calculations for the deformation in this dimension are more complicated and this should only be a first estimation. In order to obtain a detailed two dimensional surface scan it would be advisable to change the set-up, e.g. use an interferometer or at least a different camera.

If we pick a random point on the graph paper, it can be seen at varying pixel positions once

the silicon chip deforms. Neither the camera nor the graph paper changed their position or orientation, so each pixel of camera still observes the same coordinate on the chip as prior to the deformation. Seeing a different point of the graph paper in the mirror is only possible if the chip moves upwards or downwards (see figure A.2b). It is now possible to calculate the height deformation via the distance Δg between the two coordinates corresponding to the pixel positions before and after the deformation. When measuring close to the central point, the angle is about 45°, and thus Δg is approximately the height deformation.

List of Figures

List of Tables

Bibliography

[1] U. Bellgardt et al. 'Search for the decay $\mu \rightarrow eee$'. In: *Nuclear Physics B* 299.1 (1988), pp. 1–6. ISSN: 0550-3213. DOI: `https://doi.org/10.1016/0550-3213(88)90462-2`. URL: `http://www.sciencedirect.com/science/article/pii/0550321388904622`.

[2] Wikimedia Commons. *Standard Model — Wikipedia, The Free Encyclopedia*. `http://en.wikipedia.org/w/index.php?title=Standard\%20Model&oldid=826979209`. [Online; accessed 24-February-2018]. 2018.

[3] The CMS Collaboration. 'Observation of a new boson at a mass of 125 GeV with the CMS experiment at the LHC'. In: (2012). DOI: `10.1016/j.physletb.2012.08.021`. eprint: `arXiv:1207.7235`.

[4] The ATLAS Collaboration. 'Observation of a new particle in the search for the Standard Model Higgs boson with the ATLAS detector at the LHC'. In: (2012). DOI: `10.1016/j.physletb.2012.08.020`. eprint: `arXiv:1207.7214`.

[5] Peter W. Higgs. 'Broken Symmetries and the Masses of Gauge Bosons'. In: *Phys. Rev. Lett.* 13 (16 Oct. 1964), pp. 508–509. DOI: `10.1103/PhysRevLett.13.508`. URL: `https://link.aps.org/doi/10.1103/PhysRevLett.13.508`.

[6] A. Blondel et al. *Research Proposal for an Experiment to Search for the Decay $\mu \rightarrow eee$*. 2013. eprint: `arXiv:1301.6113`.

[7] Makoto Kobayashi and Toshihide Maskawa. 'CP Violation in the Renormalizable Theory of Weak Interaction'. In: *Prog. Theor. Phys.* 49 (1973), pp. 652–657. DOI: `10.1143/PTP.49.652`.

[8] Y. Fukuda et al. 'Evidence for Oscillation of Atmospheric Neutrinos'. In: *Phys. Rev. Lett.* 81 (8 Aug. 1998), pp. 1562–1567. DOI: `10.1103/PhysRevLett.81.1562`. URL: `https://link.aps.org/doi/10.1103/PhysRevLett.81.1562`.

[9] Q. R. Ahmad et al. 'Measurement of the Rate of $\nu_e + d \rightarrow p + p + e^-$ Interactions Produced by ^8B Solar Neutrinos at the Sudbury Neutrino Observatory'. In: *Phys. Rev. Lett.* 87 (7 July 2001), p. 071301. DOI: `10.1103/PhysRevLett.87.071301`. URL: `https://link.aps.org/doi/10.1103/PhysRevLett.87.071301`.

[10] K. Eguchi et al. 'First Results from KamLAND: Evidence for Reactor Antineutrino Disappearance'. In: *Phys. Rev. Lett.* 90 (2 Jan. 2003), p. 021802. DOI: `10.1103/PhysRevLett.90.021802`. URL: `https://link.aps.org/doi/10.1103/PhysRevLett.90.021802`.

[11] Z. Maki, M. Nakagawa, and S. Sakata. 'Remarks on the Unified Model of Elementary Particles'. In: *Progress of Theoretical Physics* 28 (Nov. 1962), pp. 870–880. DOI: `10.1143/PTP.28.870`.

[12] S. L. Glashow, J. Iliopoulos, and L. Maiani. 'Weak Interactions with Lepton-Hadron Symmetry'. In: *Phys. Rev. D* 2 (7 Oct. 1970), pp. 1285–1292. DOI: `10.1103/PhysRevD.2.1285`. URL: `https://link.aps.org/doi/10.1103/PhysRevD.2.1285`.

[13] Yoshitaka Kuno and Yasuhiro Okada. 'Muon Decay and Physics Beyond the Standard Model'. In: (1999). DOI: `10.1103/RevModPhys.73.151`. eprint: `arXiv:hep-ph/9909265`.

[14] J. Beringer et al. 'Review of Particle Physics'. In: *Phys. Rev. D* 86 (1 July 2012), p. 010001. DOI: `10.1103/PhysRevD.86.010001`. URL: `https://link.aps.org/doi/10.1103/PhysRevD.86.010001`.

[15] Rashid M. Djilkibaev and Rostislav V. Konoplich. 'Rare Muon Decay $\mu^+ \to e^+ e^- e^+ \nu_e \bar{\nu_\mu}$'. In: (2008). DOI: `10.1103/PhysRevD.79.073004`. eprint: `arXiv:0812.1355`.

[16] V. L. Highland. 'Some practical remarks on multiple scattering'. In: *Nuclear Instruments and Methods* 129 (Nov. 1975), pp. 497–499. DOI: `10.1016/0029-554X(75)90743-0`.

[17] Ivan Peric. 'A novel monolithic pixelated particle detector implemented in high-voltage CMOS technology'. In: *Nucl. Instrum. Meth.* A582 (2007), pp. 876–885. DOI: `10.1016/j.nima.2007.07.115`.

[18] Antoaneta Damyanova. *Scintillating Tiles*. Presentation during Mu3e Review 2018, [Online; accessed 10-March-2018]. URL: `https://indico.psi.ch/getFile.py/access?contribId=3&resId=0&materialId=slides&confId=6365`.

[19] Yonathan Munwes. *Tile Detector*. Presentation during Mu3e Review 2018. URL: `https://indico.psi.ch/getFile.py/access?contribId=2&resId=0&materialId=slides&confId=6365`.

[20] Raphel Philipp. 'Characterisation of High Voltage Monolithic Active Pixel Sensors for the Mu3e Experiment'. MA thesis. University Heidelberg, 2014.

[21] Heiko Augustin. 'Characterization of a novel HV-MAPS Sensor with two Amplification Stages and first examination of thinned MuPix Sensors'. Master thesis. University Heidelberg, 2014.

[22] H. Augustin et al. 'MuPix7 - A fast monolithic HV-CMOS pixel chip for Mu3e'. In: (2016). DOI: `10.1088/1748-0221/11/11/C11029`. eprint: `arXiv:1610.02210`.

[23] R. Bellwied et al. 'The STAR Silicon Vertex Tracker: A large area Silicon Drift Detector'. In: *Nuclear Instruments and Methods in Physics Research Section A: Accelerators, Spectrometers, Detectors and Associated Equipment* 499.2 (2003). The Relativistic Heavy Ion Collider Project: RHIC and its Detectors, pp. 640–651. ISSN: 0168-9002. DOI: `https://doi.org/10.1016/S0168-9002(02)01962-9`. URL: `http://www.sciencedirect.com/science/article/pii/S0168900202019629`.

[24] Marco Zimmermann. 'Cooling with Gaseous Helium for the Mu3e Experiment'. Bachelor thesis. Heidelberg University, 2012.

[25] Frank P. Incropera. *Fundamentals of heat and mass transfer*. eng. 6. ed. Hoboken, NJ [u.a.]: Wiley, 2007, XXV, 997 S. ISBN: 978-0-471-45728-2 and 0-471-45728-0.

[26] Wikimedia Commons. *Boundary layer — Wikipedia, The Free Encyclopedia*. `http://en.wikipedia.org/w/index.php?title=Boundary\%20layer&oldid=808476279`. [Online; accessed 25-February-2018]. 2018.

[27] J.H. Lienhard IV and J.H. Lienhard V. *A Heat Transfer Textbook*. 4th. Version 2.11. Cambridge, MA: Phlogiston Press, 2017, p. 720. URL: `http://ahtt.mit.edu`.

[28] Lukas Huxold. 'Cooling of the Mu3e Pixel Detector'. Bachelor thesis. Heidelberg University, 2014.

[29] Adrian Herkert. 'Gaseous Helium Cooling of a Thin SIlicon Pixel Detector for the Mu3e Experiment'. Master thesis. Heidelberg University, 2015.

[30] Yanwing Ng. 'Finite Element Analysis of the Cooling System for the Mu3e Experiment'. MA thesis. University of Applied Science Jena and Heidelberg University, 2015.

[31] Lars Henkelmann. 'Optical Measurement of Vibration and Deformation of the Mu3e Silicon Pixel Tracker'. Bachelor Thesis. University Heidelberg, 2015.

[32] Rene Austermühl. 'Analyse von Michelson-Interferometriedaten von Vibrationsmessungen eines dünnen gesgekühlten Pixeldetectors'. Bachelor Thesis in german. University Heidelberg, 2015.

[33] W.M. Haynes. *CRC Handbook of Chemistry and Physics, 97th Edition*. CRC Press, 2016. ISBN: 9781498754293. URL: `https://books.google.de/books?id=VVezDAAAQBAJ`.

[34] *Autodesk CFD | CFD | Autodesk*. [Online; accessed 10-March-2018]. URL: `https://www.autodesk.de/products/cfd/overview`.

[35] *Datasheet Kapton*. DuPont. URL: `http://www.dupont.com/content/dam/dupont/products-and-services/membranes-and-films/polyimde-films/documents/DEC-Kapton-summary-of-properties.pdf`.

[36] Wolfgang Demtröder. *Experimentalphysik 1. Mechanik und Wärme*. ger. 6., überarb. u. akt. Aufl. 2013. Springer-Lehrbuch. Berlin, Heidelberg: Springer, 2013, Online–Ressource (XVI, 470 S. 615 Abb., 500 Abb. in Farbe, digital). ISBN: 978-3-642-25466-6. DOI: `10.1007/978-3-642-25466-6`. URL: `http://dx.doi.org/10.1007/978-3-642-25466-6`.

[37] Roman Gredig. 'Scintillating Fiber Detector for the Mu3e Experiment'. PhD thesis. University Zürich, 2016.

[38] J.M. Gere and S.P. Timoshenko. *Mechanics of materials*. General Engineering Series. PWS Pub Co., 1997. ISBN: 9780534934293. URL: `https://books.google.de/books?id=BKJRAAAAMAAJ`.

[39] R. Schmidt and S. Ritt. *MSCB (MIDAS Slow Control Bus)*. 2001. URL: `http://midas.psi.ch/mscb`.

[40]   *AD592 Datasheet.* URL: http://www.analog.com/media/en/technical-documentation/data-sheets/AD592.pdf.

[41]   *Product Information Pt100,Pt500,Pt1000.* Reissmann Sensortechnik GmbH. URL: http://www.apkservice.ru/files/Pt100_Pt500_Pt1000.pdf.

[42]   SERWAY. *PRINCIPLES OF PHYSICS 2E (Saunders golden sunburst series).* Brooks Cole, 1997. ISBN: 0030204577.

[43]   Frank Meier Aeschbacher. Private Communication. 2018.

[44]   Thomas Mittelstaedt. *Bericht Simulation Klebung MU3E.* Tech. rep. Report in german, date: 05.03.2018. Physical Institute Heidelberg, 2018.

[45]   *Keithley 2000 Series: $6\frac{1}{2}$-Digit Multimeter with Scanning.* URL: https://www.tek.com/digital-multimeter/broad-purpose-digital-multimeters-manual-2.

Acknowledgements

I would first like to express my gratitude to Prof. Dr. André Schöning for giving me the opportunity to work in the Mu3e group and for supervising my thesis.

I would also like to thank Prof. Dr. Norbert Herrmann for agreeing to be my second examiner.

Moreover, I would like to thank the whole Mu3e group for providing a nice working atmosphere and the support whenever needed. Especially, I would like to thank my supervisor Dr. Frank Meier Aeschbacher for entrusting me with several interesting tasks throughout the time of my thesis and helping me in any way possible. I would also like to thank Stefan Hetzel and Simon Muley for advising me during the construction of the mounting system for the thermal-mechanical mock-up, which will hopefully enable future experiments of the cooling system. Special thanks also to Adrian Herkert for introducing me to the simulation software.

At last, I would like to thank my parents, family and friends for supporting me from the beginning of my studies.

Erklärung

Ich versichere, dass ich diese Arbeit selbstständig verfasst und keine anderen als die angegebenen Quellen und Hilfsmittel benutzt habe.

Heidelberg, den 14.03.2018,